Report No.   CG-D-29-94

DESIGN, CONSTRUCTION, TEST AND EVALUATION OF A FREQUENCY SCANNING RADIOMETER FOR MEASURING OIL SLICK THICKNESSES

G. L. HOVER
U.S. Coast Guard Reseach And Development Center
1082 Shennecossett Road
Groton, Connecticut 06340-6096

AND

T. J. MURPHY, E. R. BROWN, G. G. HOGAN, O. B. MCMAHON
Lincoln Laboratory
Massachusetts Institute of Technology
244 Wood Street
Lexington, Massachusetts 02173-9108
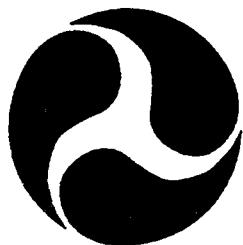
FINAL REPORT

JUNE 1994

DTIC
ELECTE
JAN 12 1995
S
G
D

Prepared for :

19950109 017

U.S. Department of Transportation
United States Coast Guard
Office of Engineering, Logistics, and Development
Washington, DC   20593

NOTICE

This document is disseminated under the sponsorship of the Department of Transportation in the interest of information exchange. The United States Government assumes no liability for its contents or use thereof.

The United States Government does not endorse products or manufacturers. Trade or manufacturers' names appear herein solely because they are considered essential to the object of this report.

The contents of this report reflect the views of the Coast Guard Research & Development Center. This report does not constitute a standard, specification, or regulation.

D. L. Motherway
Technical Director, Acting
United States Coast Guard
Research & Development Center
1082 Shennecossett Road
Groton, CT   06340-6096

ii

1. Report No. CG–D–29–94	2. Government Accession No.	3. Recipient's Catalog No.

4. Title and Subtitle	5. Report Date
Design, Construction, Test and Evaluation of a Frequency Scanning Radiometer for Measuring Oil Slick Thickness	June 1994

7. Author(s)	6. Performing Organization Code
G.L. Hover, T.J. Murphy, E.R. Brown, G.G. Hogan, and O. McMahon	
	8. Performing Organization Report No. R&DC 20/94

9. Performing Organization Name and Address	10. Work Unit No. (TRAIS)
USCG R&D Center 1082 Shennecosset Road Groton, CT 06340-6096	
MIT Lincoln Laboratory Massachusetts Institute of Technology 244 Wood Street Lexington, MA 02173-9108	11. Contract or Grant No. F19628-90-C-0002

12. Sponsoring Agency Name and Address	13. Type of Report and Period Covered
Department of Transportation U.S. Coast Guard Office of Engineering and Development Washington, DC 20593	Final October 1992 - April 1994
	14. Sponsoring Agency Code

15. Supplementary Notes

16. Abstract

Single frequency microwave radiometry has been used to detect and estimate oil slick thicknesses. Because only a single sampling point is used, estimates of oil thickness can become ambiguous. MIT Lincoln Laboratory proposed the concept of using a frequency scanning radiometer to sample multiple points across a frequency band, thus resolving the problem of ambiguities in oil thickness estimation. A laboratory-prototype FSR capable of scanning over Ka-band (26 - 40 GHz) was designed, built, and tested. The FSR was used in laboratory proof-of-principle testing to (1) measure uniform thickness oil layers under various ambient weather conditions (day, night, clear, cloudy, drizzle, and snow) and different oil types, and (2) measure the phenomenology of non-uniform thickness oil layers and emulsions. Comparisons of measured data sets with theoretical predictions demonstrated that the expected response of oil is consistent regardless of oil type or ambient weather condition. Comparisons of uniform oil layer measurements and non-uniform measurements with theoretical predictions indicate that the radiometric brightness temperature (T^B) of the oil above that of water is a function of the percentage of that thickness of oil within the antenna field-of-view. Water/oil emulsions were measured and have a higher T^B than a uniform layer of pure oil at the same thickness. Recommendations for FSR modifications and improvements, as well as future collection work are included.

17. Key Words	18. Distribution Statement
Radiometry, Oil Spill Remote Sensing, Microwave Radiometer, Oil Slick Thickness Measurement	Document is available to the U.S. Public through the National Information Service, Springfield, MA 22161

19. Security Classif. (of this report)	20. SECURITY CLASSIF. (of this page)	21. No. of Pages	22. Price
Unclassified	Unclassified		

FORM DOT F 1700.7 (8/72) Reproduction of form and completed page is authorized.

METRIC CONVERSION FACTORS

Approximate Conversions to Metric Measures

Symbol	When You Know	Multiply By	To Find	Symbol
		LENGTH		
in	inches	*2.5	centimeters	cm
ft	feet	30	centimeters	cm
yd	yards	0.9	meters	m
mi	miles	1.6	kilometers	km
		AREA		
in²	square inches	6.5	square centimeters	cm²
ft²	square feet	0.09	square meters	m²
yd²	square yards	0.8	square meters	m²
mi²	square miles	2.6	square kilometers	km²
	acres	0.4	hectares	ha
		MASS (WEIGHT)		
oz	ounces	28	grams	g
lb	pounds	0.45	kilograms	kg
	short tons (2000 lb)	0.9	tonnes	t
		VOLUME		
tsp	teaspoons	5	milliliters	ml
tbsp	tablespoons	15	milliliters	ml
fl oz	fluid ounces	30	milliliters	ml
c	cups	0.24	liters	l
pt	pints	0.47	liters	l
qt	quarts	0.95	liters	l
gal	gallons	3.8	liters	l
ft³	cubic feet	0.03	cubic meters	m³
yd³	cubic yards	0.76	cubic meters	m³
		TEMPERATURE (EXACT)		
°F	Fahrenheit temperature	5/9 (after subtracting 32)	Celsius temperature	°C

*1 in = 2.54 (exactly).

Approximate Conversions from Metric Measures

Symbol	When You Know	Multiply By	To Find	Symbol
		LENGTH		
mm	millimeters	0.04	inches	in
cm	centimeters	0.4	inches	in
m	meters	3.3	feet	ft
m	meters	1.1	yards	yd
km	kilometers	0.6	miles	mi
		AREA		
cm²	square centimeters	0.16	square inches	in²
m²	square meters	1.2	square yards	yd²
km²	square kilometers	0.4	square miles	mi²
ha	hectares (10,000 m²)	2.5	acres	
		MASS (WEIGHT)		
g	grams	0.035	ounces	oz
kg	kilograms	2.2	pounds	lb
t	tonnes (1000 kg)	1.1	short tons	
		VOLUME		
ml	milliliters	0.03	fluid ounces	fl oz
l	liters	0.125	cups	c
l	liters	2.1	pints	pt
l	liters	1.06	quarts	qt
l	liters	0.26	gallons	gal
m³	cubic meters	35	cubic feet	ft³
m³	cubic meters	1.3	cubic yards	yd³
		TEMPERATURE (EXACT)		
°C	Celsius temperature	9/5 (then add 32)	Fahrenheit temperature	°F

Temperature scale:

-40°F   0   32   40   80   98.6   120   160   200   212°F

-40°C -20   0   20   37   40   60   80   100°C

TABLE OF CONTENTS

TABLE OF CONTENTS (CONT'D)

TABLE OF CONTENTS (CONT'D)

Accesion For		
NTIS CRA&I		☒
DTIC TAB		☐
Unannounced		☐
Justification		
By		
Distribution /		
Availability Codes		
Dist	Avail and / or Special	
A-1		

LIST OF ILLUSTRATIONS

LIST OF ILLUSTRATIONS (CONT'D)

LIST OF ILLUSTRATIONS (CONT'D)

LIST OF TABLES

EXECUTIVE SUMMARY

Background

In the early 1970's, the Naval Research Laboratory investigated the use of passive single frequency microwave radiometry to detect oil slicks and to estimate the oil layer thickness. The results of those experiments showed that microwave radiometry could detect oil and estimate oil thicknesses; however, because of the single sampling point, estimates of oil thickness became ambiguous.

MIT Lincoln Laboratory proposed the concept of using a frequency scanning radiometer (FSR) to sample multiple points across a frequency band, thus resolving the problem of ambiguous oil thickness estimation. With recent advances in millimeter wave technology, off-the-shelf products have become available which make it economically feasible to obtain radiometric measurements across a wide frequency band. Lincoln Laboratory, under sponsorship of the United States Coast Guard, has developed and tested a frequency scanning radiometer (FSR) that operates over the Ka-Band (26 - 40 GHz).

This final report starts with a complete technical description of the theory of radiometry as applied to the oil-slick thickness measurement problem. The advantages of using an FSR to measure over a wide band of frequencies instead of measuring the radiometric brightness temperature (T^B) with a fixed-frequency instrument are then discussed.

FSR Development and Testing

The FSR instrument underwent extensive testing and characterization before oil thickness data measurements were conducted. The receiver characterization tests, equipment design tradeoffs, as well as the instrument calibration techniques are presented. The FSR is capable of measuring small changes in brightness temperature down to approximately 1 degree Kelvin.

Proof-of-principle tests consisted of measuring various types of oil in uniform layers from 0 mm (no oil) to thicknesses of 9 mm in 1.0 mm steps, under various ambient conditions. In addition, thin layers of oil were measured from 0 mm to 1 mm in steps of 0.1 mm. The object of proof-of-principle tests was to show that (1) the FSR could measure uniform thickness oil layers under laboratory conditions with repeatable results, (2) the results were consistent with theoretical predictions, and (3) the instrument could measure oil layer thicknesses under various ambient conditions, i.e. show an all weather capability. The results of these tests show that crude oil, kerosene, and a heavy pump oil all have similar radiometric brightness temperature characteristics, and these characteristics are practically constant (although there is a bias term) with various ambient conditions (day, night, drizzle, snow, clear and cloudy). All of the uniform oil measurements conformed to the theoretical model, and due to the large number of measurements conducted, the data collected from the FSR was shown to be repeatable. After experience is gained operating the FSR, the operator can identify uniform oil thicknesses by the characteristic sinusoidal shape of their T^B versus frequency response.

A limited set of laboratory measurements attempted to model the problems of measuring non-uniform oil layers. These modeled "real-world" problems included measuring patchy areas of oil in the antenna field of view to simulate tar balls, and step thickness functions and gradients to simulate wind rows. The results of these measurements show that the presence of any oil in the antenna field of view causes a measurable increase in T^B across the FSR bandwidth. Estimates of surface area covered by oil and oil thickness in that area compare well with the actual values.

Emulsified oil/water mixtures using three different percentages of water content were measured at four thicknesses. As expected, the emulsified oil had a much higher T^B than the surrounding water or any uniform layer prediction. The 20% water/oil emulsion curve appears to follow the sinusoidal characteristic expected for uniform oil layers while the higher percentage water emulsions have a flat response.

Conclusions and Recommendations

The FSR has demonstrated its all weather capability of detecting oil-slick thickness by measuring various types of oil in a controlled laboratory environment. FSR measurements under various atmospheric conditions, namely day and night, clear, overcast, drizzle, and snow have been obtained. All of the measurements show results for uniform layers that are consistent with theoretical predictions. Measurements of crude oil, motor oil, and kerosene, have demonstrated that the results are independent of oil type. For each of the non-uniform layer scenarios investigated, the characteristic change of T^B versus frequency due to the oil layer was a function of the antenna fill factor; the percentage of the layer filling the antenna field of view. Non-uniform oil thickness measurements were compared against uniform thickness oil measurements that have the same "average" oil thickness in the antenna field of view. For the same average thickness, characteristics of the thicker non-uniform oil layer were evident in the resulting curves.

For the short term, the development of the FSR should be continued by modifying it for use at an outdoors facility in a real-world environment to measure controlled oil-slicks in a wave-generating tank. The development of algorithms to detect oil layer thicknesses and percentage of oil in the beam is necessary for an oil slick mapping capability and this activity should continue.

Over the long term, development of a multichannel FSR receiver using off-the-shelf technology should be pursued. The multichannel FSR receiver would allow for fast 'snapshot' like thickness measurements because the instrument would not scan over the Ka band in discrete steps; instead of a serial type data collection system it would become a parallel receive system. This capability is needed for realistic airborne collection scenarios where an operational commander can use an oil thickness map of a large oil slick area to direct cleanup resources and operations.

The FSR demonstrated the ability to detect the presence of thin oil layers (tenths of millimeters) as a slight rise in the mean T^B. Thin oil layers can be measured by expanding the frequency coverage to a higher band, namely, 75 - 100 GHz. A single frequency measurement near 94 GHz, in addition to the measurements over 26 - 40 GHz, could aid in the detection of thin oil layers, potentially down to a minimum thickness of 0.05 mm. Ultimately, to measure very thin layers, a 75 - 100 GHz FSR could be built using commercially available products.

ACKNOWLEDGEMENTS

CHAPTER 1
INTRODUCTION

1.1 BACKGROUND

One of the major problems associated with oil spills on the ocean is determining the thick-oil regions so that appropriate countermeasures can be applied to those areas. Although an oil slick can cover very large areas, more than 80% of the spilled oil is often contained in less than 20% of the slick area [reference 1]. Therefore, it is crucial that an accurate spatial-oil-thickness map be constructed so that oil spill countermeasures can be efficiently employed.

The USCG has a requirement to develop an all-weather day-night capability to remotely measure oil-slick thickness. The Coast Guard Research and Development Center has been tasked with the evaluation of sensor technologies that could significantly enhance the Coast Guard's oil-spill remote-sensing capabilities. Although many types of sensors can detect the presence of oil on the ocean' surface, only a few can be used to estimate the oil spill thickness. These include visual inspection, ultraviolet laser techniques, infrared/ultraviolet (IR/UV) radiometry and millimeter/microwave radiometry. Each of these methods can determine oil thickness; however, each method has limitations. Visual inspection is useful only in clear, daylight conditions [reference 2]. Laser-induced fluorescence and Raman backscatter techniques are limited to thin layers [references 3, 4, 5]. IR/UV radiometry can sometimes provide relative thickness data to discriminate very thin sheen from thicker oil, but signatures are highly variable and dependent upon a complex interaction among numerous sensor-, target-, and environment-related parameters [reference 6]. Millimeter/microwave radiometry is the only one of these techniques that can determine the thickness of oil layers greater than about 1 mm [reference 7]. Millimeter/microwave radiometry is also the only method among the four with the potential to operate effectively at night and in low visibility.

Microwave radiometry (MWR) was investigated by Hollinger in the early '70's for oil slick thickness determination [reference 1]. This technology has been used in a number of oil thickness investigations of controlled spills in ocean conditions [references 1, 7, 8, 9, 10]. Despite the success of the technology in the laboratory, problems arose during field implementation. These radiometer designs, which operated at specific frequencies, encountered significant uncertainties in thickness estimation due to inherent ambiguities in the limited data set produced by fixed-frequency radiometry. Recent advances in off-the-shelf millimeter-wave instrumentation and components call for a re-evaluation of passive microwave radiometry as a sensor technology potentially capable of all-weather oil-slick-thickness determination.

MIT Lincoln Laboratory has identified a unique approach to oil thickness sensing that takes advantage of recent developments in commercially available millimeter wave components. This approach involves measuring the radiometric temperature of a source while scanning over a wide frequency range (Ka-band, 26 - 40 GHz) to obtain a continuous measurement (data set) of oil slick signature data (i.e., radiometric temperatures). From these signatures the oil spill thickness within the antenna footprint can be determined uniquely, without the ambiguity associated with fixed frequency radiometry, by fitting the measured data set with theoretical predictions of the oil response.

This report documents the design, construction and testing of a laboratory model frequency scanning radiometer (FSR). It includes a discussion of using an FSR in lieu of fixed frequency radiometry. Controlled measurements of various thicknesses of oil layers on water under various atmospheric and physical conditions were conducted outdoors. The measurement procedure and the results will be discussed. Based on these results, an assessment of using this technology for operationally viable all-weather measurement of oil slick thickness will be presented.

1.2 OBJECTIVE

The objective of this project was to design and construct a laboratory-prototype, FSR and to perform initial proof-of-principle demonstrations of the oil-slick thickness-measurement concept. To meet this objective, a statement of work for this project was generated that delineated four specific task areas, namely,

1. Design and construct a frequency scanning radiometer receiver using off-the-shelf components from commercial vendors.

2. Characterize the radiometer receiver performance across the 26 - 40 GHz band (Ka-band).

3. Select an appropriate off-the-shelf antenna system, data recording system and appropriate display hardware to integrate the radiometer receiver into a test system capable of demonstrating the feasibility of the oil thickness measurement concept.

4. Use the system in a laboratory environment to collect sufficient data to assess whether the FSR can be used to determine oil layer thicknesses.

1.3 SCOPE

The scope of this report is to document the activities performed to satisfy the tasks outlined above. Chapter 2 of this report will provide an introduction to the principles of radiometry and will compare fixed frequency radiometry to frequency scanning radiometry. Chapter 3 will describe the construction and characterization of the FSR. Chapter 4 describes the test and analysis procedures used to collect and compare measured data sets of known oil thicknesses with theoretical predictions. An extensive set of laboratory FSR thickness data is presented for several oil types, emulsions, and simulated 'field condition' scenarios including measurement of non-uniform oil layers. Chapter 5 provides an assessment of concept feasibility and recommendations for the next-version FSR instrument and measurements that should be conducted using that instrument.

CHAPTER 2
MILLIMETER WAVE RADIOMETRY

A radiometer is an instrument used to measure the radiometric brightness temperature of areas within the instrument's antenna field of view. The radiometric brightness temperature is a measure of the equivalent blackbody temperature of a scene within a certain frequency band, not a measure of its physical temperature. This chapter introduces the theory upon which radiometric sensing of oil slick thickness is based. In the 1970's and 80's single frequency radiometry was used in early tests to determine oil slick thicknesses, but ambiguous results made these measurements unreliable. The concept of frequency scanning radiometry is introduced and the advantages of using this method are compared against using single frequency radiometry.

2.1 THEORY OF RADIOMETRIC OIL THICKNESS SENSING

Oil thickness sensing by means of passive radiometry relies on measurement of the millimeter or microwave radiation emanating from the oil/water surface at a specific frequency. The strength of this radiation is expressed as an apparent brightness temperature, T^B, and the strength varies as a function of frequency. Referring to Figure 2-1, the received T^B signal is a combination of the radiation emitted from the water that is transmitted through the oil/water interface, and the radiation emitted by the sky and reflected at the oil/water interface. The T^B signal is a measure of the equivalent blackbody temperature of the oil/water combination, not a measure of its physical temperature. Microwave radiometry is attractive for oil thickness sensing because a radiometer is a totally passive receiver system, thus fewer components are required than a system that produces its own illumination (e.g., radar, laser-induced fluorescence). This results in a smaller, simpler, less complicated and less expensive measurement system that uses less power.
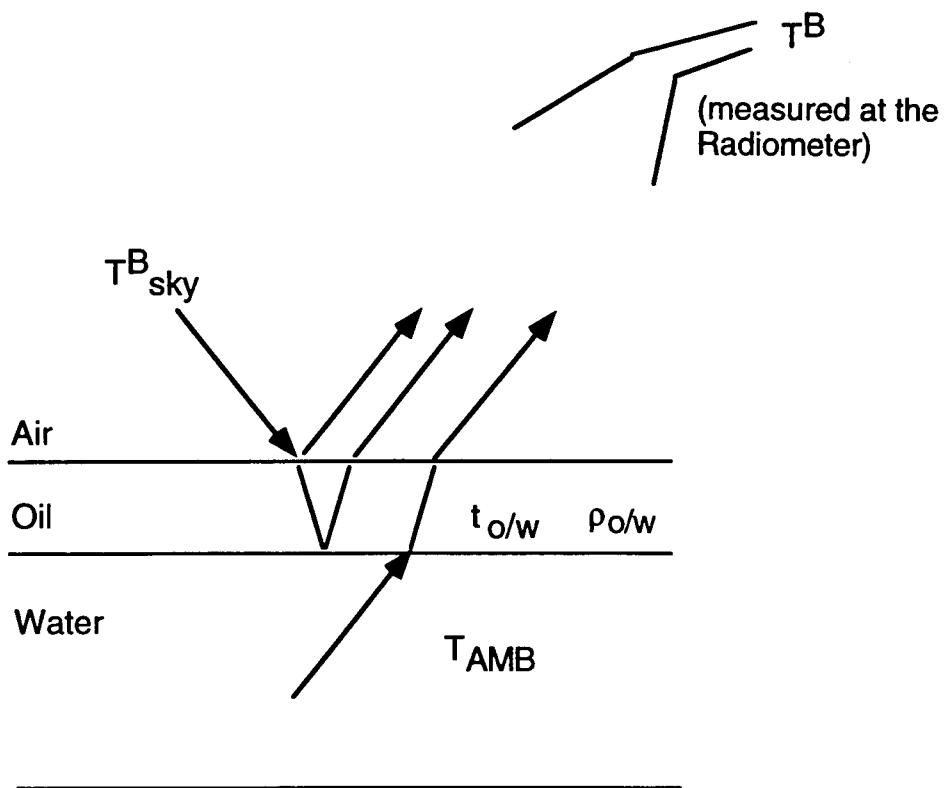
Figure 2-1. Radiometric Source Geometry for Oil Thickness Sensing

Because microwave radiometry does not require a self illuminating source (i.e., it doesn't need a transmitter to provide illumination), it can collect the unique signature of an oil layer over a large range of angles, under all weather conditions. Ambient atmospheric and ocean conditions provide the radiation (background illumination) needed to produce the T^B signature, with the unique properties of the T^B signature dependent on the physical properties of the oil. These properties are the dielectric constant and the layer thickness.

For a spatially uniform oil layer, T^B is a quasi-sinusoidal function of oil thickness, d. This relation, T^B vs. d, is illustrated in Figure 2-2 for theoretical radiometric curves at three widely separated frequencies of 5, 17, and 35 GHz [reference 7]. The oil film acts as an electromagnetic interface layer between the water and free space modulating the apparent brightness temperature of the water. (This is similar to the effect of an intermediate-refractive-index dielectric coating on optical components.) As the thickness of the oil layer is increased at a given frequency, the apparent microwave brightness temperature at first increases and
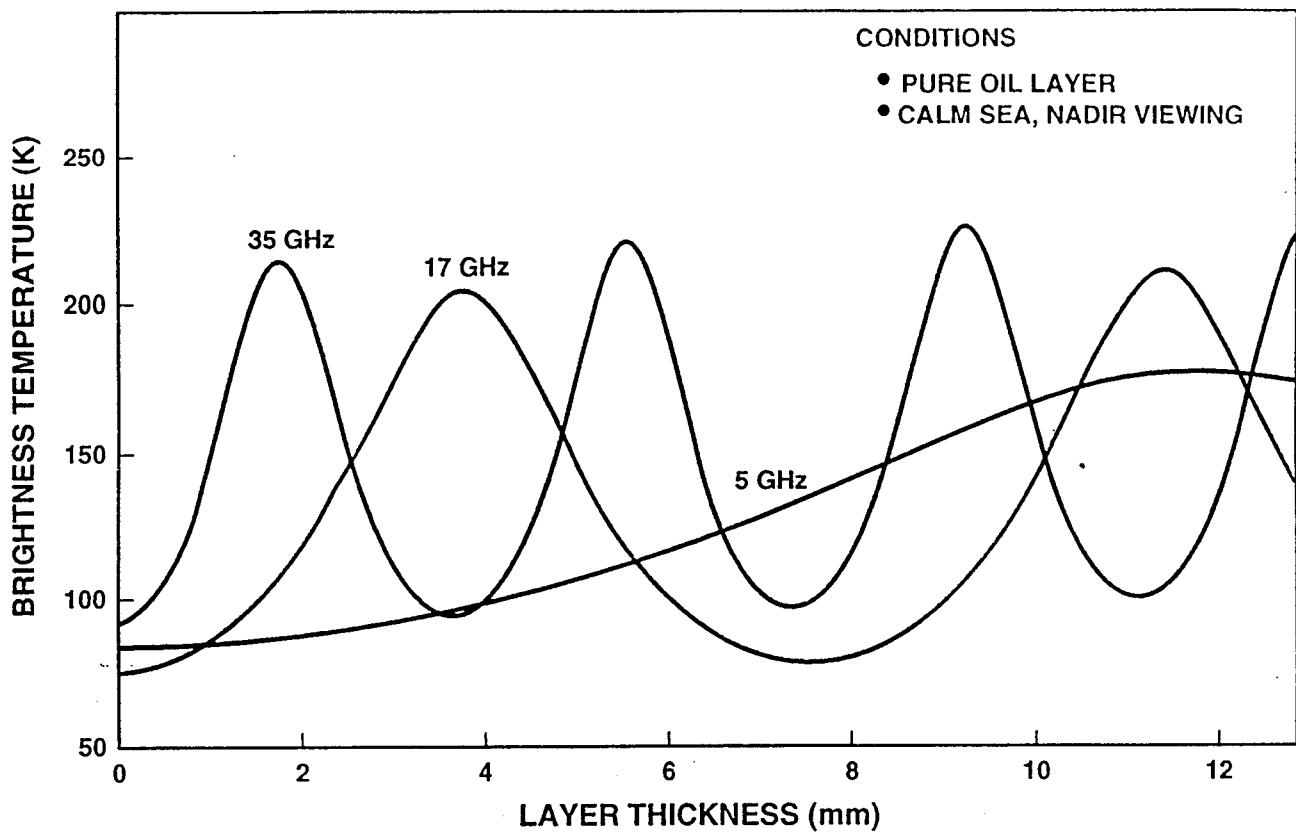
Figure 2-2. Simulated Radiometric Brightness Temperature vs Layer Thickness
for Three Frequencies

then decreases, passing through alternating maxima and minima due to the
interference pattern set up in the oil layer. The adjacent maxima and minima are
separated by integral multiples of a quarter of the electromagnetic wavelength in
the oil.

The apparent brightness temperature of water can be expressed as

$$T^B_W = \varepsilon T_W + \rho T^B_{sky}, \quad\quad\quad (2.1)$$

where ε is the emissivity of the body of water, T_W is its physical temperature, ρ is
its power reflectivity, and T^B_{sky} is the brightness temperature of the sky. In the
microwave and millimeter-wavelength regions, T^B_{sky} is determined in part by
emission from water vapor (particularly clouds), oxygen, and a few other
molecular species through the atmospheric column. Across the Ka band, T^B_{sky}
increases by approximately 1 K with every 2 GHz increase of frequency. The
emissivity and reflectivity in Equation (2.1) are related in a fundamental way

through Kirchoff's relation,

$$\varepsilon = 1 - \rho \qquad (2.2)$$

For both fresh and salt waters, ρ decreases rapidly with frequency in the microwave and millimeter-wave regions from a value of approximately 0.63 at 10 GHz to less than 0.45 at 100 GHz. Hence, assuming that $T_W \gg T^B_{sky}$ (which is usually the case except near frequencies of strong atmospheric absorption such as the oxygen line near 60 GHz), we expect T^B_W to increase monotonically over this frequency range.

In the presence of a uniform oil film on top of the water, we can still use Equations (2.1) and (2.2) provided that the oil and water have the same physical temperature, that T^B_W is replaced by T^B_{ow} for the oil-water combination, and that ε and ρ are understood to apply to this combination. In this case, we can calculate ρ using the optical theory of transmission through thin films (i.e., etalons). The theory is particularly simple when the film is non-absorbing, which is a good approximation for oil in the microwave and millimeter-wave regions. In this case, there is no attenuation of the radiation in the film and the field reflectivity at the oil-air interface is a real quantity $r_{O/A}$. Because water is highly absorbing in the microwave and millimeter-wave regions, the field reflectivity at the oil-water interface must be represented by a complex quantity $r_{OW}e^{i\phi}$, where ρ_{OW} and ϕ (the phase shift upon reflection) are functions of frequency. Calculating these interface reflectivities for radiation incident from the oil side, we obtain the following expression for the net reflection [9],

$$\rho \approx 1 - \frac{(1 - \rho_{OW})(1 - \rho_{OA})}{1 - 2r_{O/W}r_{O/A}\cos(2\delta + \phi) + \rho_{OW}\rho_{OA}}, \qquad (2.3)$$

where δ is the optical phase delay incurred by one pass through the film, $\rho_{OW} \equiv r^2_{OW}$ and $\rho_{OA} \equiv r^2_{O/A}$. The second term in the denominator arises from the physical process of multiple-pass interference of radiation within the film. The interference modulates the reflectivity, and thus the emissivity, as a function of frequency, leading to a commensurate modulation of T^B_{ow}. This physical effect is the basis of our oil-thickness measurement technique.

A general expression for the single-pass phase delay is

$$\delta = (2\pi d n_O / \lambda)\cos\theta_O = (2\pi d f / c)(n_O^2 - n_A^2 \sin^2\theta_A)^{1/2} \tag{2.4}$$

where n_O is the refractive index of the oil, d is the the thickness of the film, λ is the wavelength of the radiation in vacuum, $f = c/\lambda$ where c is the speed of light in a vacuum, θ_O is the angle of propagation in the oil away from the normal direction, n_A is the refractive index of the air (nominally 1.0), and θ_A is the angle of propagation in the air away from the normal. The last step in Equation (2.4) follows from Snell's law of refraction. Each of the reflectivities in Equation (2.3) is implicitly a function of θ_O as well.

A useful approximation to Equation (2.3) results from the fact that the microwave refractive index of oil is low ($n_O \approx 1.4$), making the magnitude of $r_{O/A}$ much less than unity. For example, at normal incidence Fresnel's equation yields $r_{O/A} = (n_O - 1)/(n_O + 1) \approx 0.17$. A second useful approximation is based on the fact that across the Ka band the real part of the refractive index of water is much higher than that of oil. Hence, the phase shift upon reflection at the oil-water interface (radiation incident from the oil side) is close 180°, so that $\phi \approx \pi + \eta$ with $\eta \ll \pi$. This leads to $\cos(2\delta + \phi) = -\cos(2\delta + \eta)$. To take advantage of these approximations, we expand Equation (2.3) to first order in $r_{O/A}$,

$$\rho \approx \rho_{ow} + 2(1 - \rho_{ow})r_{o/w}r_{o/A}\cos(2\delta + \eta) . \tag{2.5}$$

In the limit of zero thickness and small η, this reduces to $\rho \approx \rho_{ow} + 2(1 - \rho_{ow})r_{o/w}r_{o/A}$ which is an expression for the reflectivity of the water-air interface under the given approximations. We label this quantity ρ_{AW}. Note that ρ_{AW} is greater than ρ_{OW} as one should expect intuitively from the greater index constrast between air and water.

Upon substituting Equation (2.5) into Equation (2.1) and applying Equation (2.2), we find

$$T_{OW}^B \approx \rho_{OW}T_{SKY}^B + (1 - \rho_{OW})T_W - (\rho_{AW} - \rho_{OW})(T_W - T_{SKY}^B)\cos(2\delta + \eta) \tag{2.6}$$

Upon substituting the trigonometric identity $\cos\beta = 1 - 2\sin^2(\beta/2)$, we find

$$T_{OW}^B \approx \rho_{AW}T_{SKY}^B + (1-\rho_{AW})T_W + 2(\rho_{AW} - \rho_{OW})(T_W - T_{SKY}^B)\sin^2(\delta + \eta/2)$$

$$= T_W^B + 2(\rho_{AW} - \rho_{OW})(T_W - T_{SKY}^B)\sin^2(\delta + \eta/2)$$

(2.7)

In examining this equation it is seen that the period of the sinusoidal T^B_{OW} response (referred to in the remainder of the report as T^B) is a function of the single-pass phase delay. From Equation (2.4), the single-pass phase delay is a function of the refractive index (n_0) of the oil (which, for unemulsified oil, varies little with oil type), the radiometer sampling frequency (a constant for fixed-frequency radiometers, or a number of measurements over the Ka-band for the FSR), and the layer thickness. In the next section, using Equation (2.7) as a basis, oil slick thickness sensing using fixed-frequency radiometry techniques will be presented. Section 2.3 will discuss the advantages of determining slick thickness using the frequency-scanning radiometric approach.

Equation 2.7 is introduced as an approximate expression for T^B. It is used for discussion purposes because the actual expression for T^B is quite complicated with minor amplitude dependencies on temperature and salinity. The important factor that millimeter-wave radiometry will measure is the $\sin^2$ dependence of oil thickness. All theoretical prediction curves used in this report have been produced using the actual expression for T^B, Equation (2.6), and the actual expression for the dielectric constant of water [reference 13].

2.2 FIXED-FREQUENCY RADIOMETRY

The brightness temperature curves shown in Figure 2-2 vary more rapidly (i.e., steeper slopes) with thickness as sensor measurement frequency increases. Thus, sensor measurement sensitivity is a function of the slope of the T^B vs. d curve; the steeper the slope, the greater the measurement sensitivity. This suggests that greater measurement sensitivity and hence greater accuracy in oil thickness sensing can be achieved with higher frequency sensors. However, because of the sinusoidal response of the brightness temperature curve, there is an ambiguity problem: a given brightness temperature corresponds to many different thicknesses. Thus, one can unambiguously measure thickness only up to a d_{max} that corresponds to the first T^B peak. For example, to unambiguously

measure to a d_{max} of 1 cm would require a frequency of 5 GHz or less, as shown in Figure 2-2, and thicker layers would require lower frequencies.

Thus, fixed-frequency radiometry faces a dilemma: measurement sensitivity is proportional to frequency (the higher the frequency, the greater the sensitivity), but thickness ambiguity is inversely proportional to frequency (the higher the frequency, the smaller the thickness that can be unambiguously measured). When a fixed-frequency radiometer encounters layer thicknesses greater than its d_{max}, (e.g., 1.5 mm for a 35 GHz sensor), under-estimation of the oil thickness results. At this point, one may decide that sensitivity can be traded for unambiguous data by using a low frequency sensor. Unfortunately, a low-frequency approach would have the additional problem of large footprint size, which results in images with poor spatial resolution.

Given an antenna of fixed dimension, the radiometer footprint size is inversely proportional to frequency. Antenna size is generally limited by the airborne platform which must carry the radiometer instrument. This, in turn, limits the spatial resolution that can be achieved at low frequencies. For example, a 10-cm antenna would provide a footprint size of approximately 186 m at a 1000 ft. altitude with a 5 GHz radiometer. This improves to 25 m at 35 GHz, enabling better oil slick feature discrimination. At this frequency, however, the thickness ambiguity discussed earlier becomes problematic.

Another issue that must be addressed for fixed-frequency radiometry is that precise instrument calibration is required. Because brightness temperature varies more slowly with thickness as sensor operating frequency decreases, a single small measurement error results in over (or under) estimation of the oil layer thickness. This concept is illustrated by comparing the 5 GHz and 35 GHz curves in Figure 2-2. The slope of the 5 GHz curves is very shallow, resulting in large thickness errors for small errors in measured T^B.

One historical approach to solving the thickness-ambiguity problem was to add a second or even a third fixed frequency radiometer at different frequencies. Although this approach was somewhat successful, thickness ambiguity problems remained and sensor system bulk and complexity increased proportionally [references 1, 7].

2.3 FREQUENCY-SCANNING RADIOMETRY

Expanding upon the idea of two fixed frequency radiometers, a new oil thickness sensing approach was developed based on a frequency-scanning (tunable) radiometer, FSR. This concept has only become practical in the last few years as wideband microwave components have emerged. With an FSR, a continuous curve of brightness temperature as a function of frequency is obtained for a given location on the oil slick. With sufficient bandwidth, this technique has the potential to overcome the problems associated with ambiguous brightness temperature measurements inherent to fixed-frequency radiometry.

Figure 2-3 shows simulated T^B responses at three frequencies for oil layers of varying thicknesses. Figure 2-3 is similar to Figure 2-2 except the abscissa is now frequency instead of thickness (in this case, T^B response for three thicknesses is plotted as a function of frequency). As in Figure 2-2, Equation (2.1) was used to compute the curves and Equation (2.7) provides a good approximation. The only difference is that for Figure 2-2, f is held constant and for Figure 2-3, d is held constant. The signal variations of Figure 2-3 (and Figure 2-2) result from interference effects in the weakly-absorbing layer. They exhibit a sinusoidal behavior as a function of f very similar to that seen in Figure 2-2 as a function of d. When more than one thickness is present, the overall T^B response is a combination of the responses for each of the thickness components.

The FSR approach offers advantages over fixed frequency radiometry in determining the thickness of an oil slick. As discussed in the following paragraphs, FSR offers potential solutions to fixed-frequency radiometry problems of thickness ambiguity, calibration sensitivity, and measuring oil thickness distributions within the footprint.
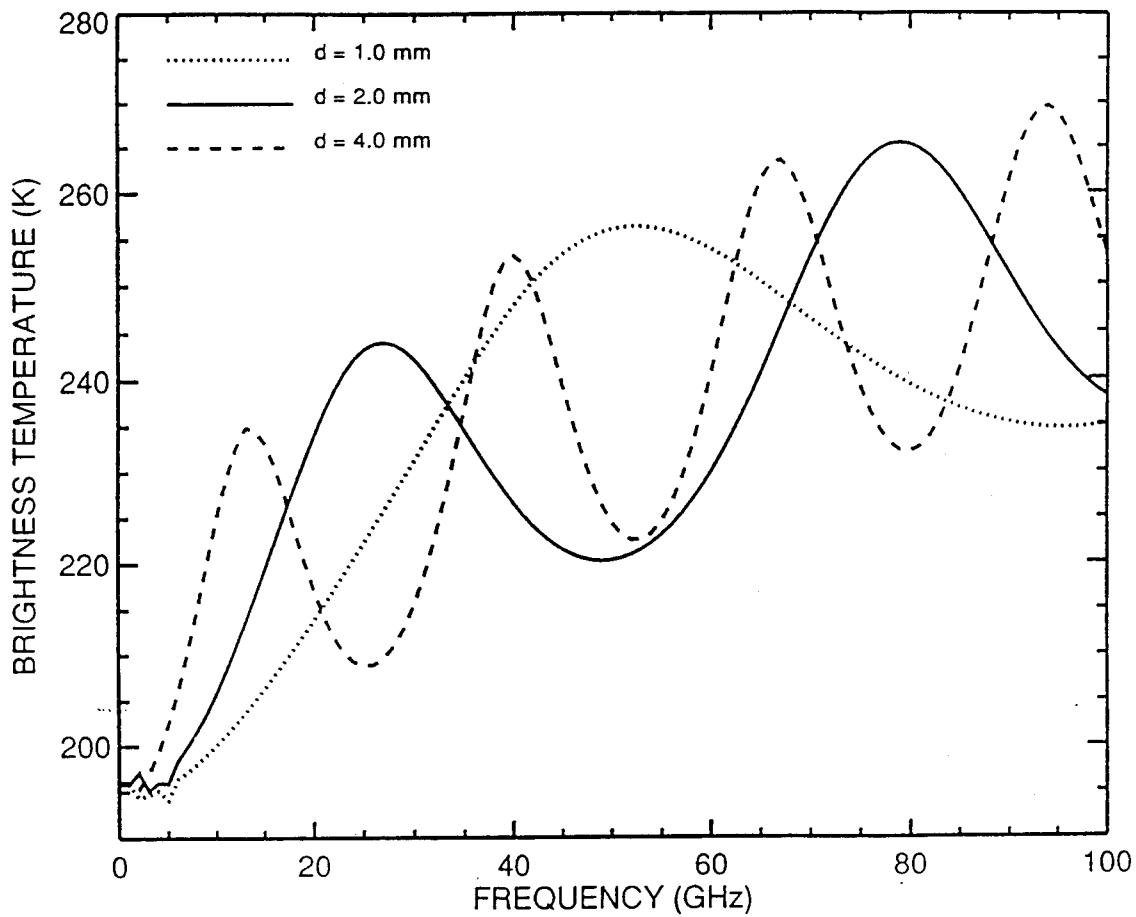
Figure 2-3. Simulated FSR Brightness Temperature vs Frequency for Pure Oil
at Three Thicknesses

Thickness Ambiguity. Recall that thickness ambiguities arise because
thicknesses above some value, d_{max}, appear to have the same brightness
temperature as at least one lower thickness. When only one data point is
collected (single frequency) these multiple thicknesses cannot be discriminated.
On the other hand, the FSR will measure the brightness temperature in discrete
frequency bands separated by an interval, Δf. By Nyquist's sampling theorem,
the thickest oil layer, d_{max}, that can be measured without ambiguity (i.e., without
"aliasing") is the one whose T^B curve displays one half cycle over Δf. From
Equation (2.7), the term creating the sinusoidal variation of T^B is $\sin^2(\delta + \eta/2)$.
To investigate the relation of thickness and sampling frequency, this trigonomic
identity can be reduced, the identity set equal to the condition that satisfies the
Nyquist criterion (at least two samples over the sampling interval for $\sin^2$ requires
$\pi/2$ separation), and with δ expressed in terms from Equation (2.4),

2 - 9

$$(2\pi d_{max}\Delta f / c)(n_0^2 - n_a^2 \sin^2 \theta_a)^{1/2} + \eta/2 = \pi/2 \qquad (2.8)$$

Grouping terms yields

$$(2\pi d_{max}\Delta f / c)(n_0^2 - n_a^2 \sin^2 \theta_a)^{1/2} = (\pi - \eta)/2 \qquad (2.9)$$

Recall that $\eta \ll \pi$, so $(\pi - \eta)/2 \approx \pi/2$. The equation is next solved for d_{max}, as

$$d_{max} = \frac{c}{4\Delta f \left(n_0^2 - n_a^2 \sin^2 \theta_a\right)^{1/2}} \qquad (2.10)$$

Equation (2.10) states that d_{max} is inversely proportional to the frequency sampling interval. For the case of a fixed-frequency radiometer, two T^B values are known; one at $f = 0$, which is simply $T^B \approx T^{BW}$, and the second at the radiometer operating frequency, f. For the single frequency radiometer, the frequency sampling interval Δf is simply its measurement frequency. As an example, with $\sqrt{\varepsilon_{oil}} = 1.4$ and using a single frequency radiometer operating in the center of Ka-band, $\Delta f = 35$ GHz, the ambiguous measurement depth is $d_{max} = 0.15$ cm; that is, a single frequency radiometer operating at 35 GHz can measure oil layer thicknesses up to 0.15 cm with no ambiguity. For the case of an FSR, the frequency sampling interval Δf can be made as small as desired; hence d_{max} can be can be as large as desired. Because frequency sampling interval can be chosen by the system designer, the FSR can sample over the entire Ka band using closely spaced frequency samples to generate a continuous T^B curve.

Sensitivity. The FSR solves the sensitivity problem of fixed frequency radiometry. From the paragraph above, it might seem feasible to use a Ka-band fixed frequency radiometer in order to achieve a d_{max} of 0.15 cm. Using this high frequency band allows for good sensitivity, however, the tradeoff is ambiguous thicknesses at thin oil layers. The FSR approach can solve this dilemma by making measurements at 1 GHz sampling intervals (for high $d_{max} = 5.0$ cm) while operating at a relatively high frequency band (for high sensitivity). Additionally, by making many measurements across the band, the effect of random measurement errors causing mis-estimation of the oil thickness will be lessened.

Thickness Variation within the Antenna Footprint. A fixed-frequency radiometer can only make one T^B measurement per "look", so it can only determine the average layer thickness over the antenna footprint. An FSR makes T^B measurements over a wide frequency range within the same antenna footprint. If, over that frequency range, the different oil thicknesses within the antenna field of view exhibit sufficient variation in T^B, one may be able to use curve fitting analysis to estimate the distribution of oil thicknesses present in the radiometer's antenna footprint.

Footprint Size. As discussed above, using a millimeter wave FSR, the thickness ambiguity based on a given set of brightness temperature measurements is no longer an issue for expected oil-slick thicknesses. The FSR's ability to operate at a high center frequency results in a small footprint size given the same physical dimension antenna. A smaller footprint results in finer spatial resolution, so more sampling points can be measured over an oil slick area. As the number of thickness sampling points increases, a better estimate of the actual oil-thickness spatial distribution results. This in turn, improves the chances of locating narrow features, such as windrows, that contain thick oil.

CHAPTER 3
FREQUENCY SCANNING RADIOMETRIC RECEIVER

3.0 INTRODUCTION

This chapter contains a detailed description of the operation and calibration of the assembled radiometer system, and a list of components that make up the laboratory-version FSR. Specific tests were performed on the FSR to characterize and optimize selected receiver parameters and to check the stability of the receiver. The tests included measurement of antenna performance as a function of frequency, system sensitivity, temporal stability, and conversion loss. Test and analysis methods for these measurements are described as well as the results of each specific test.

3.1 FSR SYSTEM DESCRIPTION

The 26 - 40 GHz FSR is a total-power radiometer with a programmable frequency generator (sweep oscillator) used as the tunable local oscillator. The receiver has a double-sideband response that increases the sensitivity by a factor of two compared to a single-sideband system. A block diagram of the system is shown in Figure 3-1. The FSR operates by combining the following two signals in the single-balanced Ka-band waveguide mixer: (1) the externally sensed radiation, coupled into the mixer by the pyramidal feed antenna, and, (2) the output of the tunable local oscillator, set to frequency f_{LO}. Through the mixing process, power at the difference frequency (also called the intermediate frequency, or IF, by convention) between f_{LO} and the input power spectrum is present at the input to the IF amplifier stage. Because the radiation that is being measured is thermal, it contains a broad distribution of frequencies. Referring to Figure 3-2, with the local oscillator set at a particular f_{LO}, the parts of the broad input distribution that are mixed down to the IF band are contained in the ranges f_{LO} to $f_{LO} + B_{IF}$ (the upper sideband) and $f_{LO} - B_{IF}$ to f_{LO} (the lower sideband), where B_{IF} is the bandwidth of the intermediate frequency (IF) amplifiers and filters.

In the IF section, the signal is boosted using low noise amplifiers, and filtered to obtain the desired bandwidth. The last component in the IF section is a square-law detector. The detector puts out a voltage proportional to the total power contained within B_{IF} at the detector input. The output voltage is then converted from analog to digital by a digital voltmeter, read into the laptop control computer, converted to brightness temperature units, and stored in a data file on a computer disk in ASCII file format. The brightness temperature (or measured voltage) values at each sampled frequency are displayed on the computer screen as they are read into the computer. A plot of brightness temperature versus frequency can then be selected to compare the plot of measured signal strength (brightness temperature) versus frequency against a family of theoretical curves for various oil thicknesses.

The design of the FSR and the hardware used to implement the FSR have not changed appreciably since the unit was first assembled. Two notable differences between the earliest system and the present version are (1) the replacement of the HP Computer with a TI Model TM4000 Laptop Computer, and, (2) the incorporation of the receiver electronics into a temperature controlled unit remote from the tunable local oscillator. Photographs of the evolution of the FSR system are included as Figures 3-3 through 3-6. Figures 3-3 and 3-4 show the earliest configuration of the FSR equipment suite, Figure 3-5 shows the FSR receiver electronics in its present configuration. Figure 3-6 is a close-up of the receiver electronics, with the major components labeled.

The core components of the FSR are the Ka-band balanced mixer and a Hewlett-Packard controllable sweep oscillator with a 26 - 40 GHz output module. The sweep oscillator is controlled by the TI laptop computer through an IEEE-488 (also known as an HPIB) interface. The oscillator is commanded to generate signals at 16 discrete frequencies between 26 - 40 GHz at 0.8 GHz intervals. (Early oil thickness tests and receiver characterization tests used a 0.5 GHz interval at 29 discrete frequencies.) Radiation from the oil slick surface
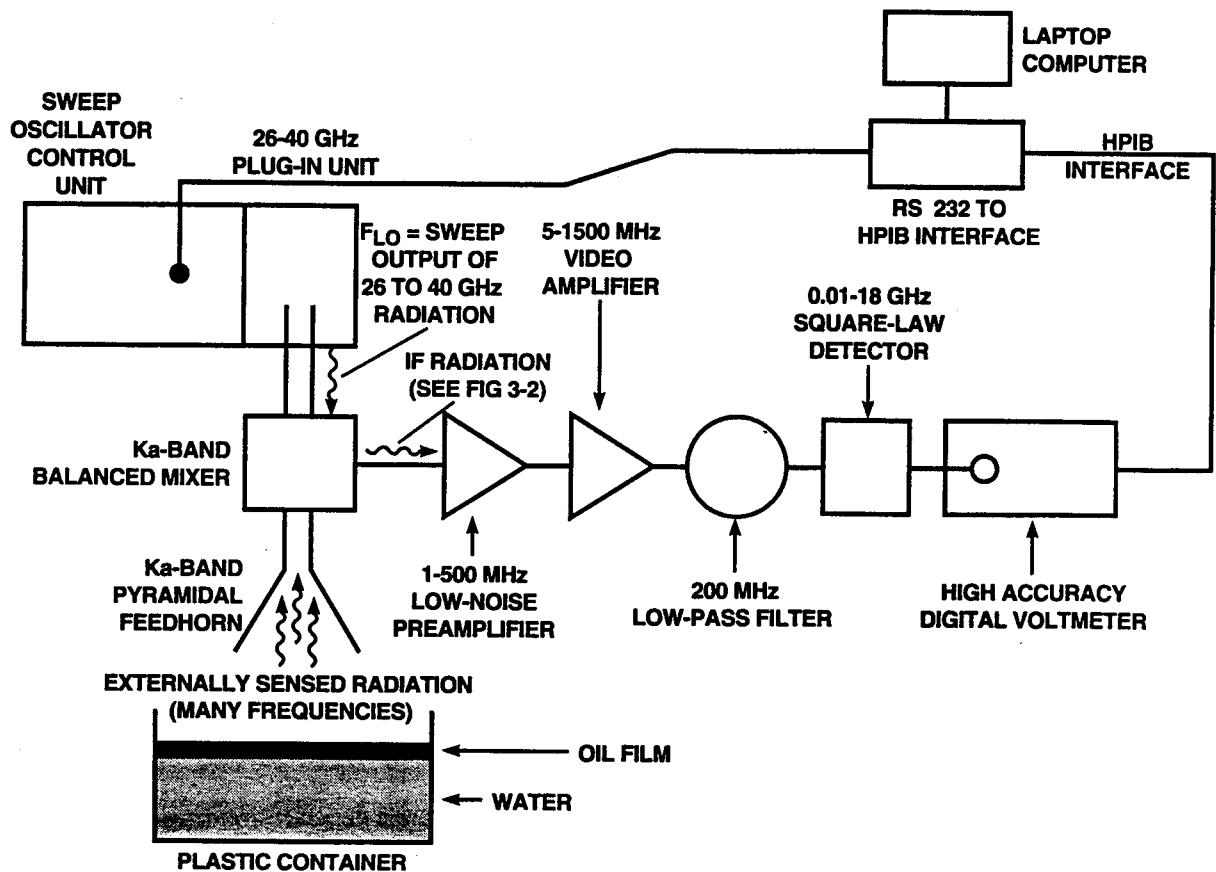
Figure 3-1. FSR Block Diagram
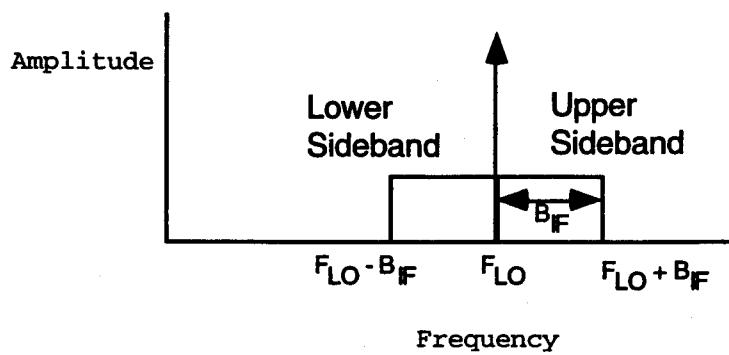
Figure 3-2. Upper and Lower Sideband
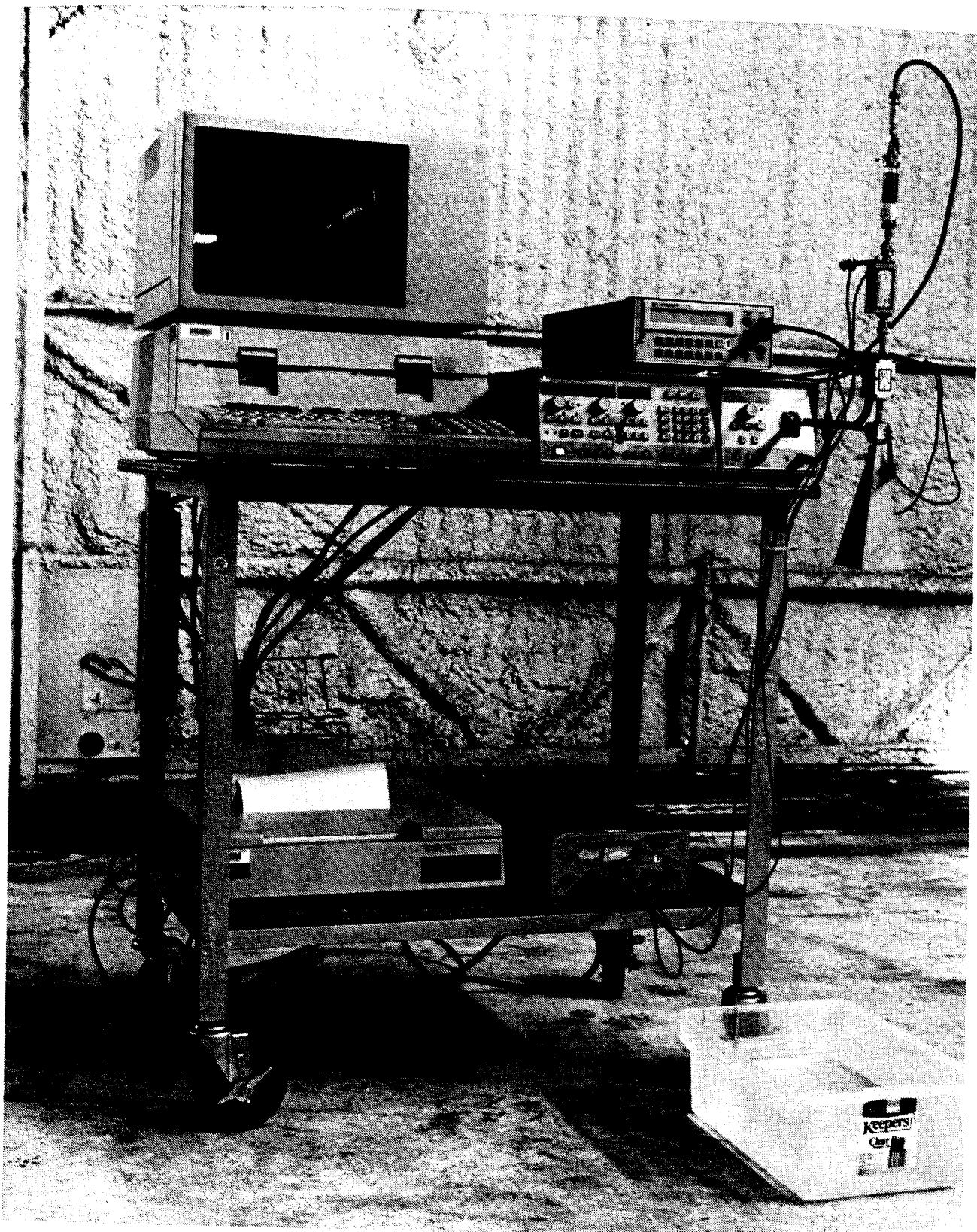
Figure 3-3. First Assembled FSR Unit
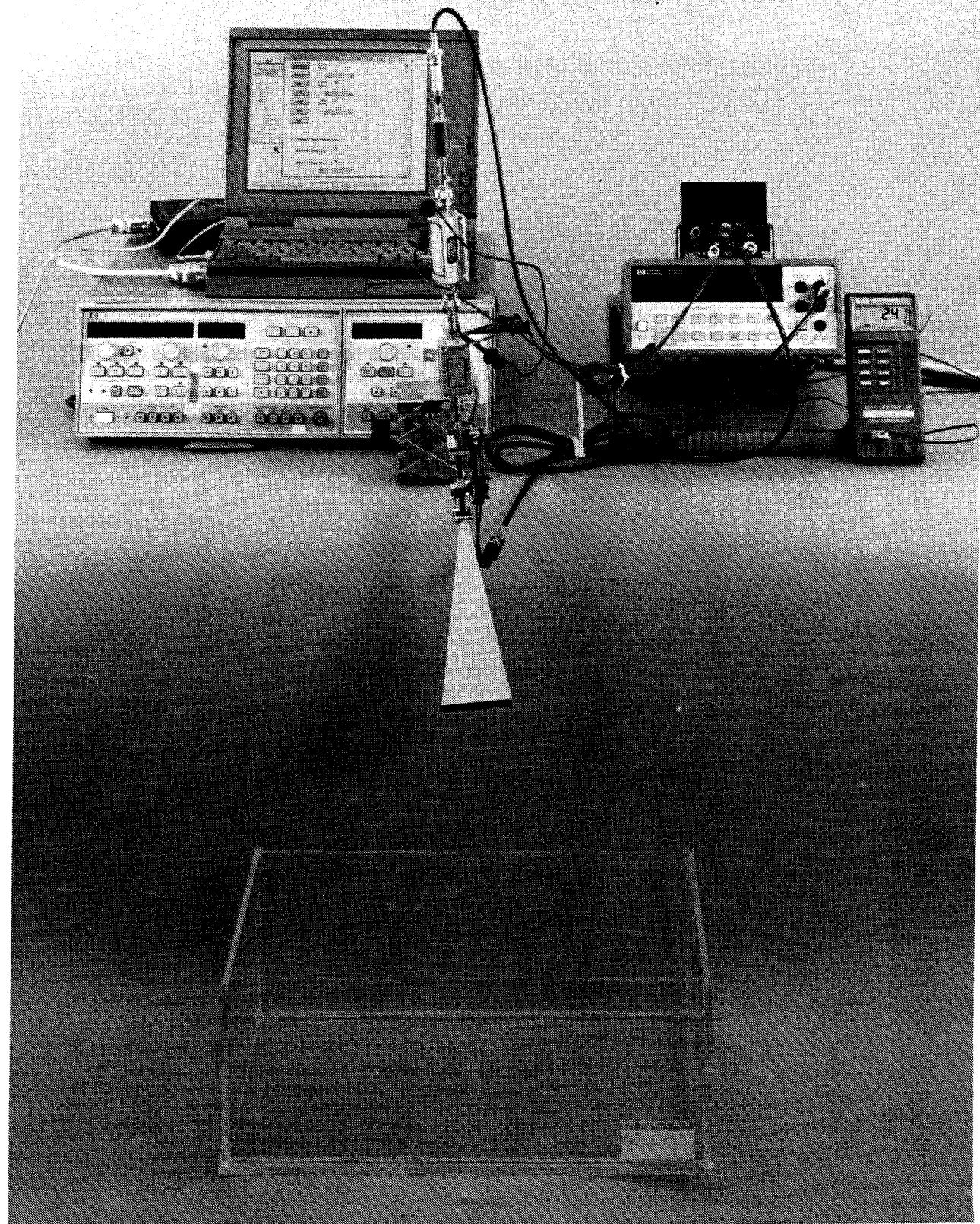
Figure 3-4. Interim FSR System During Receiver Characterization Tests
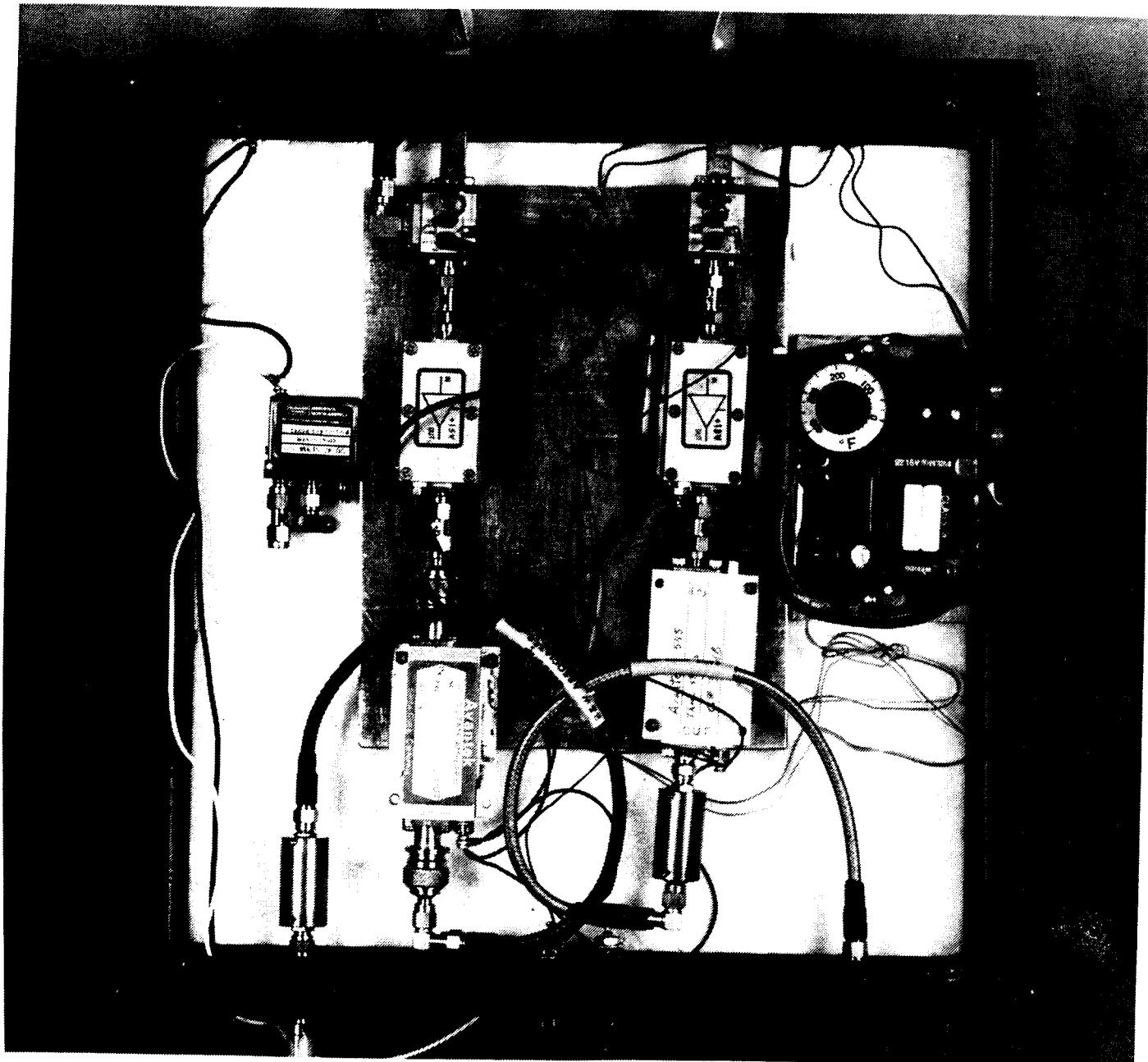
Figure 3-5. Present FSR Receiver Electronics

0.01-18 GHz SQUARE-LAW DETECTOR (H.P. 8473 B)

200 MHz LOW-PASS FILTER (Mini-Circuits NLP-200)

5-1500 MHz VIDEO AMPLIFIER (2 Avantek VTO-1522)

1-500 MHz LOW-NOISE PREAMPLIFIER (MITEQ AV-2A-0150)

Ka-BAND DIRECTIONAL COUPLER

233007-2

Ka-BAND BALANCED MIXER (Spacek MKaKa-9)

Ka-BAND PYRAMIDAL FEEDHORN

12 INCHES
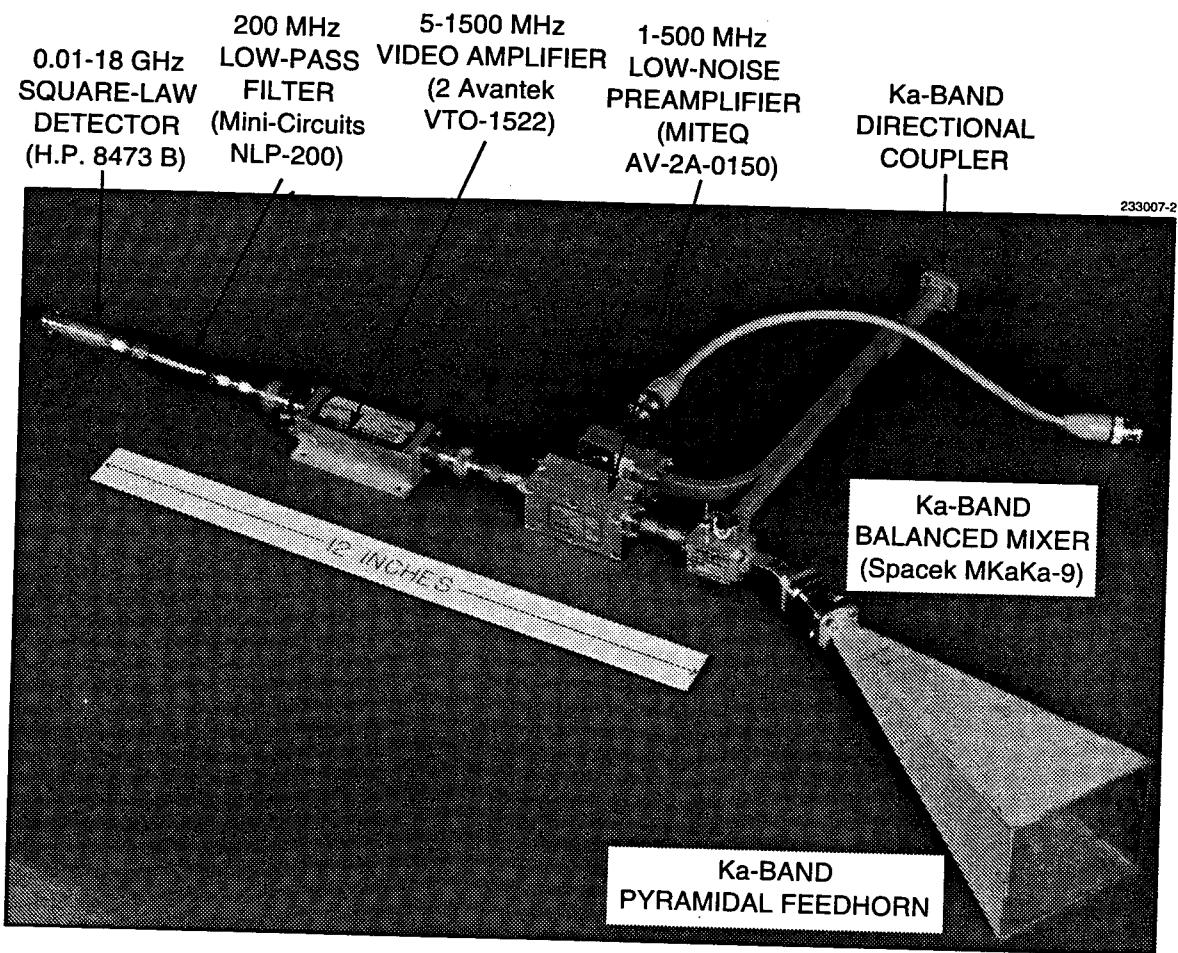
Figure 3-6. Close-Up of the Receiver Electronics

is coupled into the mixer using a Ka-band pyramidal feed horn that has a beamwidth of approximately 10°. The set of discrete frequencies produced by the sweep oscillator is mixed with the incident radiation in the Ka-band single-balanced mixer. The sweep oscillator steps through all 16 frequencies (0.8 GHz intervals) in approximately 11 seconds (for the 0.5 GHz interval the 29 frequencies were stepped through in 18 seconds), using a 0.5 second step time per frequency, and a 0.1 second integration time per frequency. The step time allows for measurement settling at the input to the high accuracy digital voltmeter. The HP sweep oscillator, using a feedback loop, keeps the output power of +10 dBm leveled. An HP R422C waveguide detector measures a sample of the oscillator output through a directional coupler, and provides the feedback voltage to the leveling circuit in the sweep oscillator. The local oscillator drive power is delivered to the mixer (in the remote electronics unit) through semi-rigid coaxial cable using a waveguide to coax adapter at the directional coupler output, and a similar adapter at the waveguide mixer input.

The IF power output of the mixer is boosted in a low noise pre-amplifier with a gain of 30 dB, noise figure of 1.2 dB, and a bandwidth of 499 MHz (1-500 MHz). Next, the signal is again amplified using a two-stage video amplifier with a gain of 35 dB. Since there is some spurious noise at the lower IF frequencies, the video amplifier bandwidth is chosen to be 50 - 500 MHz. Following amplification, the detected signal is filtered to eliminate any high frequency noise by a low-pass filter with a cutoff frequency of 450 MHz and an insertion loss of 0.5 dB. The signal is then rectified using an HP 8473B square-law detector. The detector has a sensitivity of 0.5 mV/μW with saturation occurring when the input power reaches roughly -10 dBm (100 μW), corresponding to a maximum detector output voltage of approximately 50 mV.

The analog output voltage from the square-law detector is digitized using a high-accuracy (22 bit) HP digital voltmeter. The voltmeter can measure signals from 10 μV to 1000 V and is interfaced to the laptop computer through a parallel printer port to IEEE-488 converter. The computer controls the voltmeter functions, and records the measured voltages in a data file on its internal hard disk. After all of the frequency steps have been measured and recorded, a plot

of the apparent brightness temperature (T^B) of the oil/water surface versus frequency can be displayed on the screen. These plots can be compared to theoretical curves to determine the oil thickness.

The TI laptop computer which has been interfaced to the HP sweep oscillator and digital voltmeter, controls the FSR operation. The computer uses a model 486 microprocessor running at 25 MHz, is configured with 4 MBytes of RAM, and has an internal hard disk capacity of 120 MBytes. The operating system is MS-DOS, with the FSR control program written in Visual BASIC. Currently, 3 MBytes of the internal disk space is utilized for the operating system, FSR control software, and data file storage. Since each recorded FSR scan occupies less than 1 kByte of disk space, data storage is adequate for all anticipated experiment work. As the disk fills, older scans can be archived to floppy disks for long-term storage, and the disk space is recovered for new scans. The laptop screen is an LCD gray scale display. Hardware interfaces include a VGA for an external monitor, and an RS-232. An external parallel printer port to IEEE-488 protocol converter is used to communicate with the HP equipment. Except for the interface driver software for the protocol converter, all control and analysis software for the computer was custom written for the present application.

Since the hot load temperature must be precisely known for instrument calibration, a Fluke 52 K/J Digital Thermometer was added to the original FSR equipment suite. The thermocouple consists of a chromel/alumel wire pair, and the temperature is displayed in degrees C. The ambient temperature (in degrees C) is manually entered into the computer program, converted to degrees K, and used as a calibration parameter.

The receiver electronics bipolar transistor amplifiers are mounted on an active heat sink, which is in a Styrofoam lined box. This mounting provides a temperature stable environment which reduces the effects of amplifier gain drift due to ambient temperature variations. An electronic thermostat, which can be set by the FSR operator, keeps the active heat sink at a temperature slightly higher than ambient temperature, and within 0.5° C of the setpoint.

DC power for the amplifiers and mixer is provided by a (portable, rechargeable) battery source (+12 V). The laptop computer can operate from its internal battery or from 120 VAC line voltage. The sweep oscillator, digital voltmeter, and the temperature controller operate from 120 VAC line voltage.

A list of the major components of the FSR is given in Table 3-1. Listed for each component are the manufacturer and model number.

3.2 SYSTEM CALIBRATION AND OPERATION

An FSR calibration is performed at the start of each experiment. Two thermal loads of different temperature (T_H and T_C) are placed in front of the FSR feed horn. The hot thermal load is a blackbody radiator (a piece of microwave-absorbing material or 'Eccosorb') at ambient temperature ($T_H = T_{amb}$). The cold thermal load is a piece of the same type of microwave-absorbing material placed in a bath of liquid nitrogen ($T_C = 77$ K). The FSR output voltage, V_{out}, is then recorded for the two loads at each frequency between 26 and 40 GHz. V_{out} is proportional to the brightness temperature (T^B) of the input radiation, by $V_{out} \propto T_R + T^B$, where T_R is the receiver noise temperature. Since each calibration source is considered a black body radiator, its brightness temperature is its actual temperature. Thus,

$$V_{out} \equiv V_H \propto T_R + T_H \quad \text{and} \quad V_{out} \equiv V_C \propto T_R + T_C$$

The ratio of these measured output voltages (V_H to V_C) is computed to obtain the Y-factor for each frequency step where

$$Y = V_H / V_C = (T_R + T_{amb}) / (T_R + 77). \tag{3.1}$$

By solving for T_R, the receiver noise temperature can be computed for each sampling frequency by

$$T_R = (T_{amb} - 77 \cdot Y) / (Y - 1). \tag{3.2}$$

Table 3-1 FSR Components List

ITEM	DESCRIPTION	MANUFACTURER	MODEL NO.
1	Sweep oscillator control unit	Hewlett-Packard	HP-8350B
2	RF unit 26 - 40 GHz	Hewlett-Packard	HP-83572C
3	Directional coupler	Hewlett-Packard	HP-83572-60071
4	Ka-Band mixer	Spacek	MKaKa-9
5	Waveguide section 30° bend	Baytron	3Ka-80/30°
6	Coaxial cable (2 ea)		
7	Antenna - pyramidal horn		
8	Waveguide - 1" section	MIT/LL	
9	Pre-amplifier 1 - 500 MHz	Miteq	AV-2A-015
10	Video Amplifier	Avantek	AMM-1010T
11	Low pass filter (200 MHz)	Mini-Circuits	NLP-200
12	Square-law detector (0.01 - 18 GHz)	Hewlett-Packard	HP-8473
13	SMA(M)-to-SMA(M) adapter (3 ea)		
14	SMA(F)-to-SMA(F) adapter		
15	TNC(M)-to-SMA(F) adapter (3 ea)		
16	Coax(F)-to-Banana(M) adapter		
17	High accuracy digital voltmeter	Hewlett-Packard	HP-3478A
18	Laptop computer	Texas Instruments	Travelmate 4000 WINSX
19	RS-232 to IEEE-488 adapter	IO Tech	
20	HPIB cables (2 ea)	Hewlett-Packard	
21	Thermocouple assembly	Fluke	10631A
22	Electronic Thermostat	Minco	52 K/J Thermometer
23	Power assembly	Analog Devices	CT149
24	Rechargeable battery assy	MIT/LL	950
25	Measurement tank with calibrated surface area	MIT/LL	

Miscellaneous electrical hardware and wire.

Finally, the brightness temperature associated with the oil thickness measurement can be computed at each frequency by

$$T^B = (V_{out} / V_H) \cdot (T_{amb} + T_R) - T_R \qquad (3.3)$$

where V_{out} is the output voltage measured for the input signal at each selected frequency. The brightness temperature measurements, as well as the V_H and V_C initial measurements, are stored as data files on the computer. The file name is chosen by the user and usually indicates the measurement type, oil depth, and the date of the measurement. During measurements, an activities log is kept that contains the specific information concerning the testing sequence, quantity and types of oil used, and operator comments. The recorded data file contains the date and time of measurement, a description of the measurement, and a listing of the sampled frequencies with the resulting brightness temperature (or, for V_H or V_C, the measured voltages).

3.3 RECEIVER OPERATIONAL CHARACTERISTICS

Two characteristics of the FSR have been optimized for laboratory oil-slick measurement, namely the local oscillator power, P_{LO}, and the intermediate frequency bandwidth, B_{IF}. The value of P_{LO} was chosen as a compromise between mixer performance and mixer lifetime. With too little P_{LO}, the mixer sensitivity would not be adequate. With too much P_{LO}, the mixer would run too close to breakdown and would thus be unstable or short lived. The compromise value of P_{LO} was +10 dBm (10 mW).

The value of B_{IF} was chosen in consideration of spectral resolution and temperature sensitivity. Because the FSR is a double-sideband receiver system, the spectral resolution, Δf, is given by $\Delta f = 2B_{IF}$. The FSR minimum detectable temperature is given by

$$\Delta T_N = T_R / (\tau B_{IF})^{1/2} \qquad (3.4)$$

where T_R is the double-sideband receiver noise temperature, and τ is the integration time. To minimize ΔT_N, B_{IF} should be as large as possible. The limitation on B_{IF} was set by the desire to measure at least 10 separate resolution elements in the brightness temperature period for each oil thickness. Thick oil layers will yield the most rapidly varying radiometric brightness curves versus frequency. Originally it was assumed that 20 mm was the thickest oil film that would be observed in the laboratory experiments. Simulations using theoretical predictions show that the brightness temperature of such a film will undergo one full period over approximately 5 GHz. Thus, a spectral resolution (Δf) of 0.5 GHz will provide 10 resolution elements. This led to the selection of $B_{IF} = 450$ MHz.

3.4 RECEIVER NOISE TEMPERATURE

The sensitivity of the FSR is characterized by the receiver noise temperature T_R, which is given by

$$T_R = T_{MIX} + L \cdot T_{IF}, \qquad (3.5)$$

where T_{MIX} is the mixer noise temperature, L is the double-sideband conversion loss, and T_{IF} is the noise temperature of the IF amplifier. For this application, the original prediction was that $T_{MIX} \approx 500$ K, $L \approx 3$ dB, and $T_{IF} \approx 125$ K. With these parameters, the receiver noise temperature was estimated to be 750 K.

To measure T_R, the Y-factor calibration method described in Section 3.2 was used. Using the optimized values of P_{LO} and B_{IF} described in Section 3.3, the curve of T_R shown in Figure 3-7 for the FSR operating between 26 and 40 GHz was obtained. In these measurements, T_H was ambient temperature and T_C was 77 K. In order to measure T_R without missing any frequencies or having overlap between adjacent resolution elements, the local oscillator was stepped in 0.5 GHz increments. As shown in Figure 3-7, T_R drops rapidly between 26 and 27 GHz, but is nearly constant between 28 and 40 GHz except for one obvious peak near 30.5 GHz. These features will be discussed further in the

Section 3.5. Note that for frequencies above 31 GHz, the measured values for T_R are within 20% of the original prediction of 750 K.
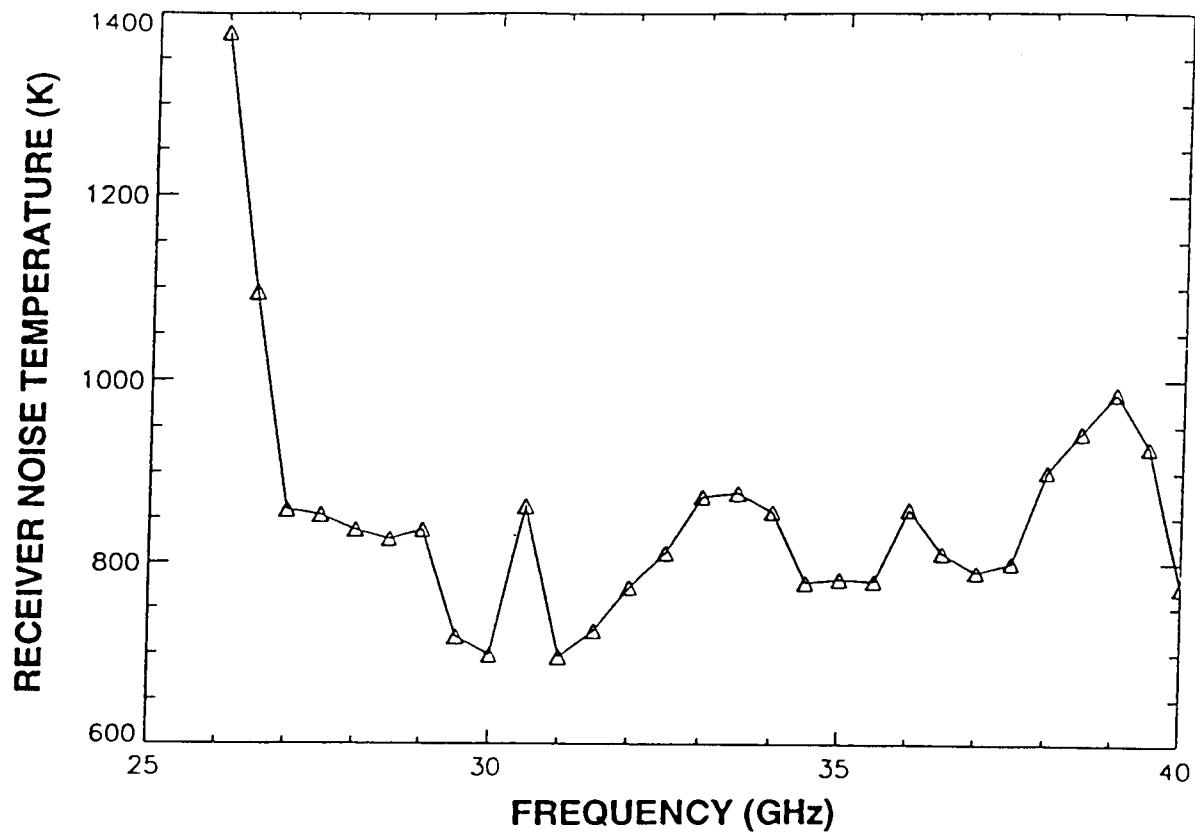

Figure 3-7. Measured Receiver Noise Temperature

3.5 MIXER NOISE TEMPERATURE AND CONVERSION LOSS

To understand the features of Figure 3-7 and shed further light on the performance characteristics of the FSR, the receiver performance was measured using two different preamplifiers, the Miteq low-noise preamplifier normally used in the system, and a higher noise preamplifier made by Avantek. The resulting curves of T_R in Figure 3-8 show that the rapid fall between 26 and 27 GHz and the peak at 30.5 GHz appear in both curves. Because these features are independent of the preamplifier used, and because the preamplifiers have nearly identical input impedance and gain characteristics, these features must be associated with the mixer or some other part of the receiver ahead of the preamplifier.
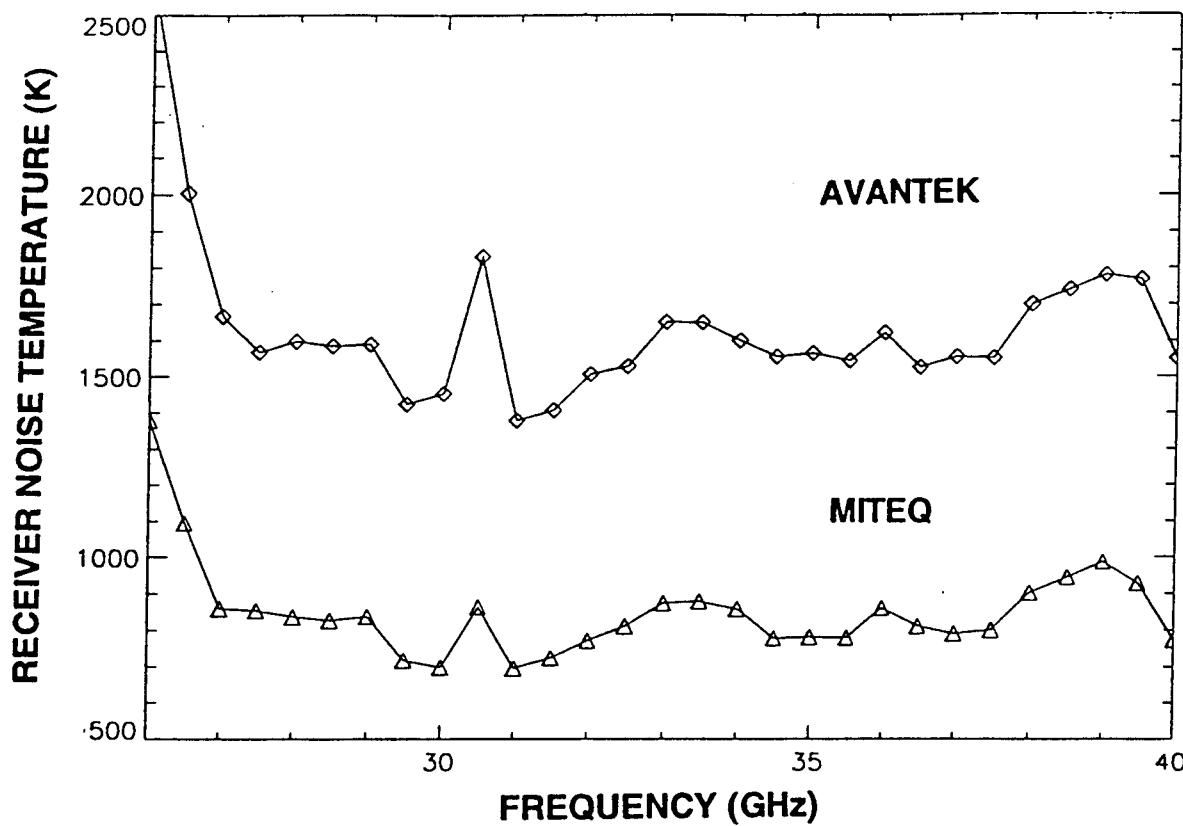

Figure 3-8. Comparison of T_R Using Miteq and Avantek Amplifiers

Measurement with two preamplifiers also allowed the determination of mixer conversion loss, L, and mixer noise temperature, T_{MIX}. These quantities are related by Equation 3.5. T_{IF} of the Miteq and Avantek preamplifiers are approximately 100 and 450 K, respectively. Because these are so different we can apply the values of T_R at each frequency in Figure 3-7 to obtain T_{MIX} and L (i.e., "two equations, two unknowns").

The results for T_{MIX} and L are plotted in Figure 3-9 and Figure 3-10, respectively. The curve for T_{MIX} displays the rapid drop between 26 and 27 GHz followed by a rather flat response from 28 to 40 GHz. The average value of T_{MIX} over the latter range is about 600 K, which is close to what we would expect for a single-balanced mixer using GaAs Schottky diodes. The features in T_{MIX} versus frequency correspond closely to those in T_R versus frequency except that the major peak at 30.5 GHz is much less pronounced in the T_{MIX} curve. This discrepancy can be explained by the behavior of L versus frequency plotted in Figure 3-10. This curve displays a large peak at 30.5 GHz in addition to the drop at the low-frequency end.
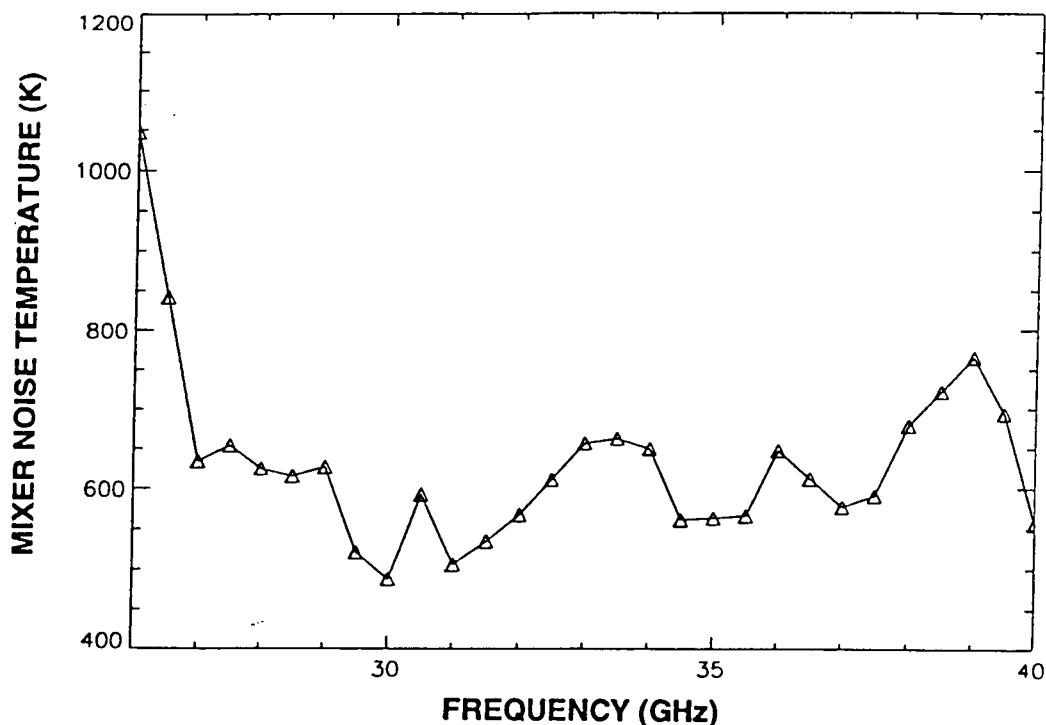


Figure 3-9. Computed T_{MIX}

3-16
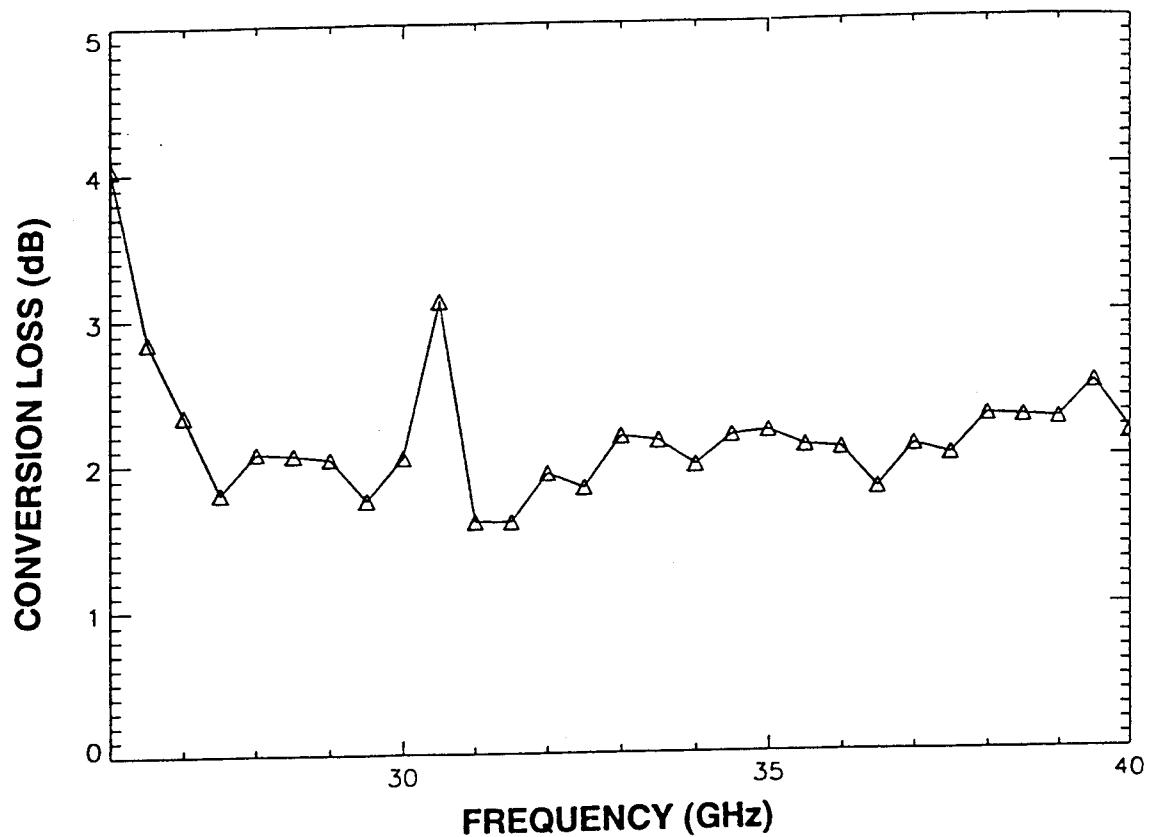
Figure 3-10. Computed Conversion Loss

These observations lead to the following conclusions regarding FSR performance characteristics. The sharp drop in each of the FSR characteristics between 26 and 27 GHz is attributed to the rise in characteristic impedance with decreasing frequency in the Ka-band waveguide that houses the mixer. This is an unavoidable consequence of using a waveguide mixer. In principle, the problem could be avoided by using a planar integrated-circuit mixer structure. However, such mixers generally have inferior overall performance compared to that of the present waveguide mixer because of the difficulty in coupling radiation from free space into the planar circuit.

3-17

After the sharp drop in FSR characteristics between 26 and 27 GHz was identified, new sampling points and sample spacings were chosen to avoid these points.

After receiver characterization testing, and during the proof-of-principle tests, the sweep oscillator RF output module failed. After this module was repaired, and FSR tested, the large conversion loss at 30.5 GHz did not return. This large peak at 30.5 GHz was a due to a poor performance characteristic in the sweep oscillator RF output module.

3.6 DYNAMIC RANGE

The receiver dynamic range is defined as the range of input radiometric temperatures over which the radiometer yields accurate readings. As the FSR is configured, the dynamic range is determined at the high end (maximum signal level) by the saturation of the square-law detector and at the low end (minimum detectable signal) by the lowest input voltage that the digital voltmeter (HP 34401A) can measure. The saturation of the square-law detector occurs when its input power approaches roughly -10 dBm (100 μW), which corresponds to an output voltage of approximately 50 mV. The minimum detectable voltmeter input is approximately 10 μV. Hence, the FSR dynamic range is 50 mV/10 μV = 5000. This is adequate for field demonstrations of the FSR. For future applications, the dynamic range could be increased by adding a dc amplifier between the square-law detector and the voltmeter.

3.7 FSR ANTENNA PATTERN

In applying the FSR to the measurement of oil thickness, it is very important to
know the aperture (area) over which the measurement is being taken. This
area is related to the antenna pattern, as shown schematically in Figure 3-11.
The relative antenna pattern is a measure of the amount of power transferred by
the feed horn into the waveguide when the horn is illuminated by an ideal plane
wave of arbitrary amplitude, propagating at angle θ with respect to the axis of
the waveguide (the axis that is perpendicular to the mouth of the feed horn.)
The pattern is dictated primarily by the feed horn design. The FSR uses an
antenna that is a pyramidal tapered-waveguide feed horn designed to operate
across the entire Ka-band. Like all pyramidal feed horns, its antenna pattern is
strongest along the axis of the waveguide, and decreases rapidly with θ.

Pyramidal
Feedhorn

θ

Beamwidth

Oil

Water
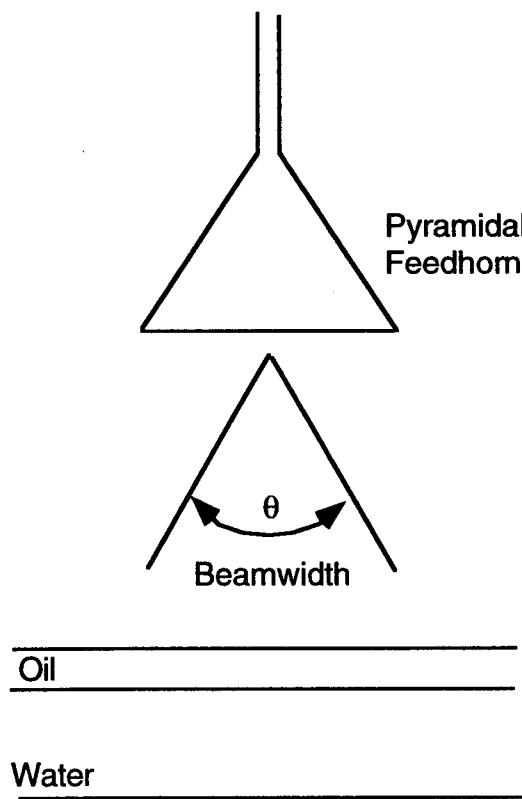
Figure 3-11. Antenna Beamwidth

3-19

The antenna pattern of the FSR was measured at two frequencies near the ends of the measurement frequency scan, namely, 26.5 and 40 GHz. At both frequencies, the antenna pattern was characterized by the angular width, $\Delta\theta$, between the points where the collected radiation was down 3 dB (50% of the peak amplitude) and 10 dB (10% of the peak amplitude) relative to the axis that is perpendicular to the mouth of the feed horn. These widths are designated as $\Delta\theta$ (3 dB) and $\Delta\theta$ (10 dB), respectively. The antenna pattern measurements were performed using two similar pyramidal feedhorns, one for transmitting and the second to receive, by stepping the transmitting horn through azimuth and elevation angles from normal incidence. The patterns are characterized with θ varying both in the plane of the electric field (E-plane) and in the orthogonal plane (H-plane). The angular widths near the end-point frequencies, and in the E- and H-plane orientations, should provide a satisfactory characterization of this pyramidal feed horn for the oil-slick measurements.

Figure 3-12 and Figure 3-13 are the plots of the measured antenna patterns at 26.5 GHz and 40 GHz, respectively, for both E-plane and H-plane orientations. The ordinate is scaled in arbitrary units proportional to watts, with the abscissa scaled in units of degrees off-axis from broadside. All four plots are identically scaled along ordinate (watts) and abscissa (degrees), so direct comparisons can be made.

Figure 3-12 shows the measured antenna patterns at 26.5 GHz. In the E-plane plot of Figure 3-12(a), $\Delta\theta$ (3 dB) = 10° and $\Delta\theta$ (10 dB) = 30°. In the H-plane plot of Figure 3-12(b), $\Delta\theta$ (3 dB) = 12° and $\Delta\theta$ (10 dB) = 22°. As is typical for this type of feed horn, the E-plane pattern is narrower than the H-plane pattern at the 3 dB point, but contains sidelobes. The first sidelobe, located approximately 20° away from broadside, is approximately 10 dB below the peak. This sidelobe contribution could be significant in certain FSR measurement situations. This will be discussed in the Section 3.8.
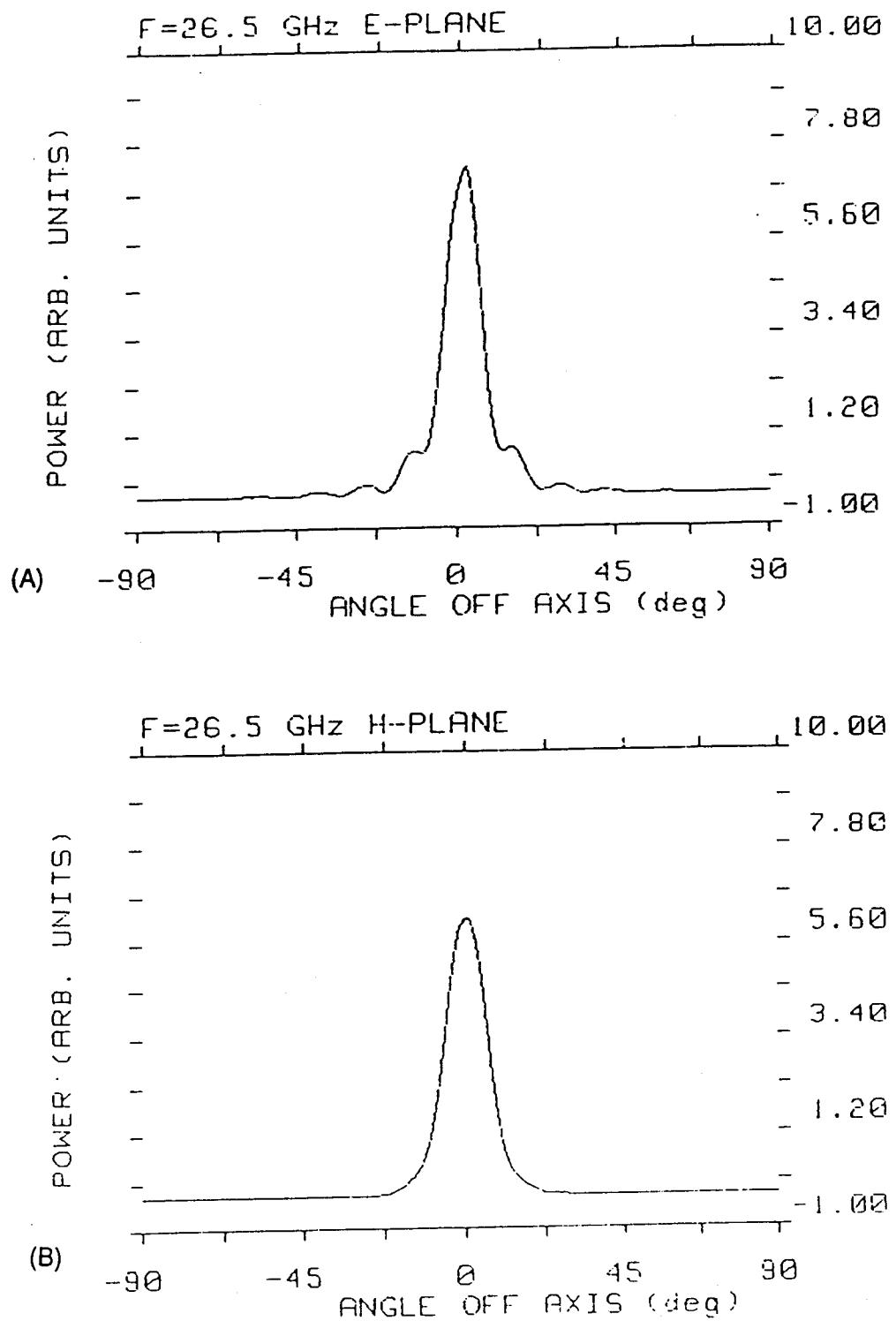
Figure 3-12. Measured Antenna Patterns at 26.5 GHz for E-plane (a)
and H-plane (b) orientations.

3-21
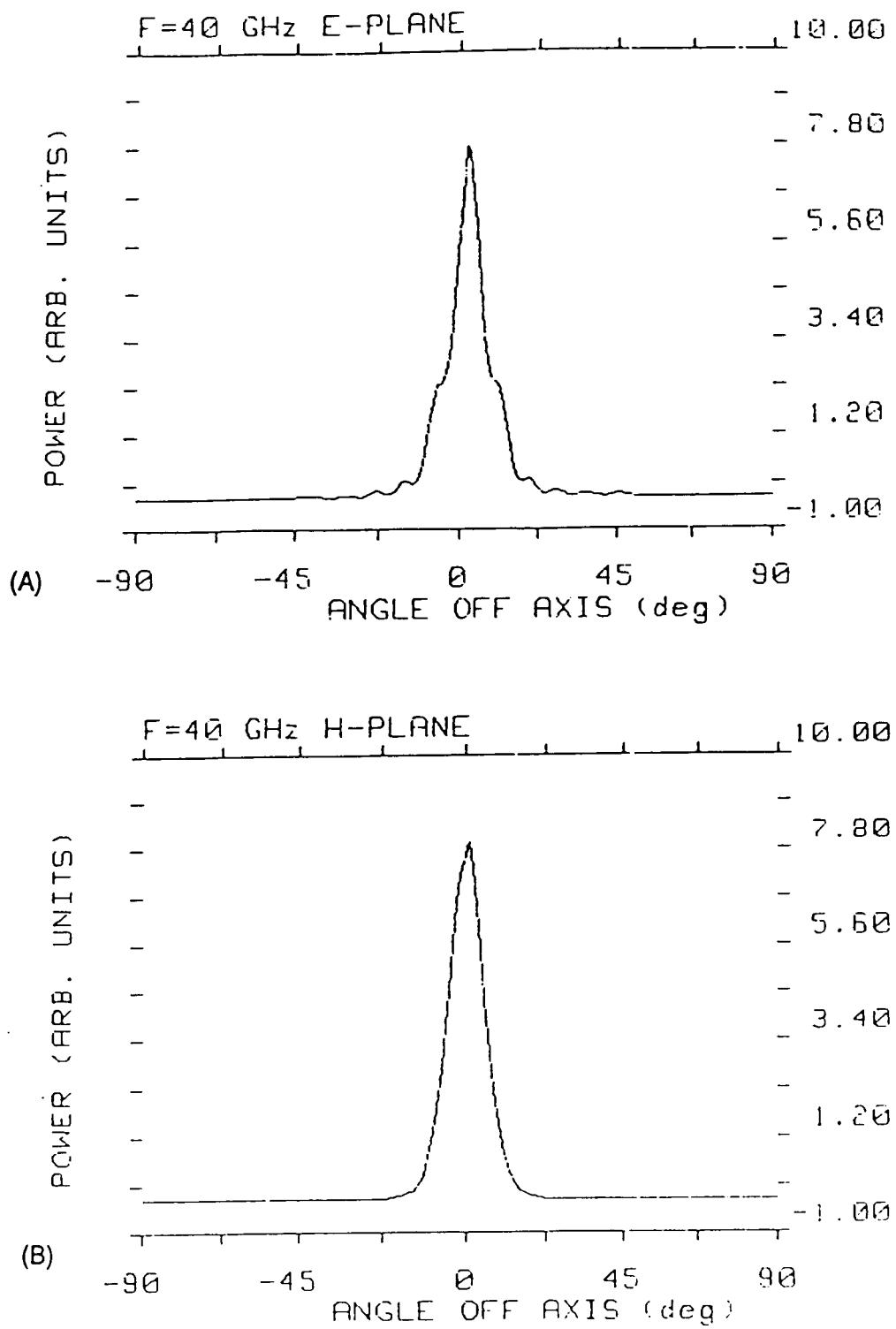
Figure 3-13. Measured Antenna Patterns at 40 GHz for E-plane (a)
and H-plane (b) orientations

Figure 3-13 shows the measured antenna patterns at 40 GHz. In the E-plane plot of Figure 3-13(a), $\Delta\theta$ (3 dB) = 8° and $\Delta\theta$ (10 dB) = 24°. In the H-plane plot of Figure 3-13(b), $\Delta\theta$ (3 dB) = 10° and $\Delta\theta$ (10 dB) = 20°. Again, the E-plane pattern is narrower than the H-plane pattern at the 3 dB point and contains sidelobes. Comparing Figures 3-12 and 3-13, it can be seen that the 40 GHz patterns are approximately 20% narrower than the corresponding 26.5 GHz patterns. The reason for this difference is similar to the reason that the receiver noise temperature is higher at lower frequencies, i.e., the characteristic impedance and dispersion of the waveguide increase significantly at the low frequency end of the waveguide band.

3.8 ANTENNA SIDELOBE SUPPRESSION

Over the Ka-band, sidelobes appear in the E-plane between 10 and 20 degrees away from broadside, and are about 10 dB down in power from the central lobe. A measurement scenario where this could cause a problem is when the thickness of the oil slick changes very rapidly with lateral position, so that the portion detected by the central lobe of the antenna has a different thickness than the portion detected by the sidelobes. In this case, there would be a spatial ambiguity in the determination of the oil slick thickness.

To avoid this problem, a superior type of waveguide antenna, namely, a scalar feedhorn could be used. This antenna is similar to a pyramidal feed horn except that grooves are cut in the inner wall of the feed horn metal. These grooves couple to radiation that tends to cancel the energy contained in the sidelobes, leading to a nearly ideal antenna pattern. In future designs, the FSR should be upgraded with this type of feedhorn. Scalar feedhorns can operate effectively over a complete waveguide band, such as our 26 - 40 GHz Ka-band, and still display a beamwidth comparable to the 10° of the present pyramidal feed horn.

3.9 RECEIVER TEMPORAL STABILITY

The receiver temporal stability was characterized by measuring the output voltage of the receiver using an ambient load as the input source, over a long period of time. Since the load temperature is nominally a constant, T_H, the variations in output voltage can be translated directly into fluctuations in minimum detectable temperature, ΔT_A. This ΔT_A is to be compared with the thermal-noise-limited value, ΔT_N, where

$$\Delta T_N = T_R / (\tau B_{IF})^{1/2}. \tag{3.6}$$

If $\Delta T_A \leq \Delta T_N$, then non-thermal fluctuations are insignificant since they do not limit the measurement and, therefore, do not affect the oil thickness determination.

The receiver temporal stability tests were performed by first allowing the instrument to warm up. Then, using an ambient load as the input source, the receiver output over the entire 26 - 40 GHz band was recorded every two minutes for one hour. Initial test results showed that the measured output was very constant except for a single glitch at the 34 minute point in all but one frequency increment. Table 3-2 shows the test frequency, the mean receiver output, V_{AVE}, and the standard deviation, ΔV, at each frequency. These numbers are transformed into ΔT_A by

$$\Delta T_A = (\Delta V / V_{AVE}) T_H \tag{3.7}$$

where $T_H = 295$ K during the measurements. For example, at 28 GHz, $\Delta T_A = 0.56$ K. For comparison, we calculate ΔT_N is calculated for the operating conditions of the receiver: $B_{IF} = 250$ MHz, $\tau = 100$ ms, and (from Figure 3-7) $T_R = 825$ K at 28 GHz. Thus, ΔT_N is computed to be 0.17 K. Since $\Delta T_A > \Delta T_N$, non-thermal fluctuations at 28 GHz were significant. However, if the glitch which occurred at minute 34 was not present, ΔT_A would decrease substantially. This

Table 3-2.
Initial Temporal Stability Test
Statistics for Hot Load

Frequency (GHz)	Mean Voltage (mV)	Standard Deviation (mV)	ΔT_A (K)
26.0	13.48	0.042	0.919
26.5	14.09	0.036	0.754
27.0	13.18	0.035	0.783
27.5	13.56	0.044	0.957
28.0	13.08	0.025	0.564
28.5	13.01	0.0009	0.020
29.0	13.06	0.029	0.655
29.5	12.23	0.029	0.355
30.0	11.40	0.025	0.647
30.5	12.03	0.027	0.662
31.0	12.76	0.040	0.925
31.5	12.79	0.028	0.646
32.0	12.85	0.030	0.689
32.5	12.87	0.027	0.619
33.0	13.06	0.029	0.655
33.5	13.14	0.032	0.718
34.0	12.90	0.027	0.617
34.5	12.58	0.025	0.586
35.0	12.39	0.031	0.738
35.5	12.50	0.034	0.802
36.0	12.65	0.030	0.700
36.5	12.74	0.031	0.718
37.0	12.77	0.034	0.785
37.5	12.87	0.031	0.711
38.0	13.64	0.034	0.735
38.5	13.93	0.018	0.381
39.0	14.15	0.018	0.375
39.5	12.61	0.034	0.866

can be seen by calculating ΔT_A at 28.5 GHz, which is the only frequency where no glitches occurred. At this frequency, $\Delta T_A = 0.20$ K, which is close to the value of ΔT_N.

Clearly, elimination of the glitches would greatly improve temporal stability. To eliminate the possible pickup of noise glitches or electromagnetic interference from external sources through the power supply or laboratory surroundings, the temporal stability test was repeated using a battery as a power supply for the mixer and amplifiers. It was assumed that there is sufficient internal filtering within the sweep oscillator to isolate its output from power line electrical interference. Two temporal stability tests were performed, one using a hot load and the other using a cold load. Table 3-3 compares the results of this test. The intent of using the cold load was to keep the temperature stable (within tenths of degrees) over the one hour test period, while the hot load test should duplicate conditions measured during the first temporal stability test. The FSR was set up outdoors with measurements collected at two minute intervals, sweeping over the 26.0 - 40.0 GHz band. The results of both of these tests indicated that no glitches were present; however, the variations in the minimum detectable temperatures were larger than in the previous test. This unexpected result occurred because of thermal drift in the gain of the FSR amplifiers that occurs outdoors.

Further tests were conducted using a hot load after the instrument had a warm-up time of over two hours. During the warm-up time a small voltage drift was observed, but after approximately two hours, no drift was observed. The results of these tests, shown in Table 3-4, indicate that during warm-up ΔT_A values were greater than ΔT_N, but after warm-up ΔT_A ranged from 0.06 to 1.26 K, with all but six of the points below 0.10 K. Thus, for all but six frequency increments, the instrument's minimum detectable temperature was thermal noise limited. This result confirmed the idea that the thermal drift affected the gain of the FSR amplifiers.

To stabilize the thermal drift in amplifier gain, the FSR electronics have been mounted on an active heat sink. The heat sink is operated at a temperature

slightly above ambient with a feedback loop stabilizing the temperature to within one degree C. Receiver temporal stability tests were not repeated after the installation of the temperature stabilization unit, however, the FSR operator has observed less drift and more consistent and repeatable results during a measurement period.

To accelerate the data acquisition process in field applications, it is anticipated that a much shorter integration time of about 10 ms could be used. In this case, the ΔT_N at 28 GHz would increase to 0.52 K, making the non-thermal fluctuations much less significant.

Tables 3-3 and 3-4 also show a decrease in the mean voltage compared with the results of the temporal stability tests in Table 3-2. Referring to Table 3-2, the mean voltage for a hot load varied between 11.4 mV and 14.2 mV. During the measurements reported in Table 3-3 and Table 3-4, the mean voltages for a hot load varied between 6.1 mV and 7.9 mV. This reduction in measured voltage was a result of using the 12 V battery to power the mixer and amplifiers instead of the 15 V power supply used to acquire the test data shown in Table 3-2 and Table 3-3. This loss of signal gain is a characteristic of the bipolar transistor amplifiers used in the system and is not a cause for concern.

Table 3-3.
Temporal Stability Test
Cold/Hot Load Comparison

	Statistics for Cold Load			Statistics for Hot Load		
Freq.	Mean Voltage	Standard Deviation	ΔT_A	Mean Voltage	Standard Deviation	ΔT_A
(GHz)	(mV)	(mV)	(K)	(mV)	(mV)	(K)
26.0	6.145	0.010	0.469	7.167	0.021	0.881
26.5	6.367	0.014	0.657	7.575	0.027	1.068
27.0	5.741	0.010	0.532	7.079	0.026	1.089
27.5	5.917	0.011	0.567	7.307	0.022	0.885
28.0	5.617	0.011	0.584	7.016	0.031	1.295
28.5	5.636	0.009	0.495	7.014	0.031	1.285
29.0	5.665	0.009	0.481	7.048	0.030	1.251
29.5	5.143	0.008	0.490	6.53 1	0.030	1.350
30.0	4.747	0.008	0.502	6.099	0.029	1.386
30.5	5.610	0.014	0.755	6.770	0.026	1.119
31.0	5.502	0.011	0.598	7.057	0.033	1.381
31.5	5.552	0.010	0.516	7.099	0.033	1.374
32.0	5.587	0.021	1.140	7.074	0.028	1.147
32.5	5.593	0.010	0.510	7.079	0.032	1.336
33.0	5.680	0.012	0.630	7.123	0.031	1.275
33.5	5.746	0.009	0.474	7.178	0.031	1.266
34.0	5.579	0.009	0.508	6.987	0.030	1.262
34.5	5.398	0.009	0.526	6.840	0.030	1.299
35.0	5.340	0.009	0.494	6.755	0.030	1.289
35.5	5.390	0.009	0.502	6.834	0.030	1.305
36.0	5.544	0.009	0.482	6.984	0.030	1.264
36.5	5.572	0.009	0.476	7.033	0.031	1.303
37.0	5.546	0.009	0.484	7.032	0.032	1.324
37.5	5.615	0.009	0.499	7.076	0.031	1.295
38.0	6.009	0.013	0.626	7.425	0.031	1.229
38.5	6.296	0.011	0.522	7.714	0.031	1.181
39.0	6.506	0.010	0.457	7.908	0.031	1.145
39.5	5.687	0.009	0.487	6.969	0.029	1.224
40.0	4.993	0.007	0.437	6.316	0.028	1.296

Table 3-4.
Temporal Stability Test Statistics
During/After Warm-Up

	Hot Load During Warm-Up			Hot Load After Warm-Up		
Freq.	Mean Voltage	Standard Deviation	ΔT_A	Mean Voltage	Standard Deviation	ΔT_A
(GHz)	(mV)	(mV)	(K)	(mV)	(mV)	(K)
26.0	7.114	0.030	1.253	7.0873	0.0242	1.0249
26.5	7.501	0.015	0.596	7.5042	0.0225	0.9012
27.0	7.026	0.014	0.597	7.0157	0.0294	1.2581
27.5	7.249	0.015	0.631	7.2489	0.0256	1.0577
28.0	6.952	0.016	0.709	6.9778	0.0018	0.0762
28.5	6.966	0.041	1.748	6.9861	0.0018	0.0787
29.0	6.994	0.034	1.458	7.0074	0.0016	0.0695
29.5	6.483	0.035	1.601	6.5005	0.0017	0.0788
30.0	6.055	0.027	1.345	6.0741	0.0014	0.0667
30.5	6.694	0.054	2.413	6.6652	0.0051	0.2308
31.0	7.009	0.032	1.391	7.0276	0.0015	0.0628
31.5	7.052	0.032	1.351	7.0747	0.0018	0.0760
32.0	6.911	0.132	5.743	6.7590	0.0204	0.9064
32.5	7.029	0.028	1.183	7.0545	0.0014	0.0609
33.0	7.059	0.015	0.625	7.0794	0.0019	0.0787
33.5	7.121	0.018	0.748	7.1477	0.0016	0.0661
34.0	6.929	0.015	0.637	6.9504	0.0017	0.0753
34.5	6.786	0.015	0.659	6.8088	0.0017	0.0729
35.0	6.695	0.016	0.700	6.7189	0.0014	0.0629
35.5	6.778	0.017	0.749	6.8037	0.0019	0.0824
36.0	6.926	0.014	0.598	6.9461	0.0018	0.0764
36.5	6.974	0.020	0.862	7.0023	0.0017	0.0716
37.0	6.967	0.017	0.750	6.9923	0.0016	0.0691
37.5	7.015	0.020	0.872	7.0446	0.0015	0.0627
38.0	7.339	0.018	0.750	7.3608	0.0019	0.0778
38.5	7.635	0.020	0.784	7.6615	0.0017	0.0684
39.0	7.840	0.022	0.836	7.8669	0.0022	0.0835
39.5	6.935	0.030	1.302	6.9737	0.0024	0.1049
40.0	6.254	0.019	0.907	6.2829	0.0018	0.0848

CHAPTER 4 - TEST RESULTS

4.0 INTRODUCTION

This chapter describes the proof-of-principle tests undertaken to measure oil slick thicknesses after the FSR equipment had been characterized. The test procedures followed and equipment fabricated to support the tests are described. Experimental results obtained with uniform thickness oil layers will be compared with corresponding theoretical predictions of T^B versus frequency. The results will be discussed in detail. Measurements of stepped thickness oil gradients, patchy oil, and emulsions which were intended to simulate real-world conditions will be included and compared to theoretical predictions and measured uniform oil layers that have the same 'average' depth within the antenna field of view.

4.1 TEST PROCEDURE - UNIFORM OIL LAYERS

Oil-thickness measurements were conducted in an outdoor laboratory environment using the 26 - 40 GHz FSR after the receiver characterization tests (described in Chapter 3) were complete. Measurements were collected under various atmospheric conditions to test the system's all-weather capability and multiple measurements show the repeatability of results. Different oil types were used to show that the results are consistent for various oil type. Table 4-1 contains a summary of the measurements taken as part of the proof of principle tests outlined in the original statement of work. Oil thickness measurements ranged from 0 mm (no oil present) to 9 mm, in increments of 1 mm.

Prior to the start of an oil thickness measurement, the instrument was calibrated using hot and cold loads to obtain the receiver noise temperature using the Y-factor calibration method outlined in Section 3.2. Briefly, a hot load consisting of microwave absorbing material ('Eccosorb') at room temperature was placed in front of the feed horn. The microwave absorbing material covered the entire field of view of the antenna. Data for the hot load was then collected over the 26 - 40 GHz band. A bath of liquid nitrogen was used to saturate a similar sheet of microwave absorbing material to create a cold load. This was then

re-introduced in front of the feed horn and cold load data was collected. The receiver noise temperature was computed as detailed in Section 3.2. Once the receiver noise temperature (T_R) at each sample frequency was known, a direct computation of the oil slick brightness temperature at each sample frequency was made by applying T_R to each measurement (Equation 3.3). The time and date, measurement type, sample frequencies and brightness temperatures are recorded in files on the laptop computer for further analysis.

The measurement tank is a portable, rectangular Plexiglas tank, with internal dimensions of 40 cm long by 25 cm wide by 20 cm deep. The tank was constructed such that (1) the surface area dimensions were larger than area measured by the antenna and (2) a surface area was created that had an easily measurable volumetric conversion for defining oil thicknesses. The surface area of the liquid is 1000 cm^2, so, a measured volume of 100 ml of oil will create an oil thickness of 1 mm. This tank was placed on a sheet of microwave absorbing material so that a consistent and repeatable background feature was formed. Fresh (tap) water was poured into the tank to an approximate depth of 5 cm. After measurements of water T^B were obtained, oil was carefully added to the tank so that it will form a layer of uniform thickness above the water surface.

Table 4-1. Summary of Uniform Thickness Measurements

Date	Oil Type	Ambient Conditions
8 Oct. 1993	Pump oil	Day, mostly sunny, high cirrus clouds, 26° C
15 Oct. 1993	Pump oil	Day, overcast, slight drizzle, 12° C
2 Dec. 1993	Aviation Fuel	Day, overcast, 7.9° C
9 Dec. 1993	Aviation Fuel	Day, mostly sunny, high thin clouds, 3.8° C
14 Dec. 1993	Aviation Fuel	Day, overcast with light rain, 20.5° C
		Night, light drizzle, 7° C
17 Dec. 1993	Aviation Fuel	Night, clear sky, 1° C
15 Feb. 1994	Crude oil	Day, partly sunny, high stratus clouds, 9.5° C

Consistent with the results of the receiver characterization tests, the FSR was configured to scan programmed steps with an individual bandwidth of 500 MHz. The step time at each of the frequency measurements was approximately 0.5 seconds, with a 0.1 second integration time. Over the progressive months of data collection and analysis, it was found that the number of sampled frequency steps could be decreased from 29 to 16. This allows for a faster sweep over the frequency band (less dwell time) with no resulting degradation in the characteristic shape of the T^B curves. Additionally, if Fourier transform processing of the data is undertaken, 16 samples is an optimum sample set to utilize; it is a power of two, and no zero filling or further data set reduction will be necessary.

During the measurements, an entry in the laboratory notebook was made concerning each of the following items:

- ambient temperature (in °C),
- weather conditions (sunny, raining, overcast) including a comment concerning cloud cover,
- file names for each recorded measurement,
- oil types, quantities, and thicknesses used for each measurement, and,
- any observed aberrations in equipment operation.

To assure that the uniform layer measurements were repeatable within the same measurement day, independent looks at oil thicknesses were made by collecting a set of measurements at oil thicknesses of 0 mm to 9 mm in 1 mm steps. The calibrated tank was then cleaned, and a second set of measurements was collected at the specified oil thicknesses (0 - 9 mm in 1 mm steps). Measurements using this procedure were made over different days, using different oil types, and under different ambient conditions. The Section 4.2 will compare the results of these uniform layer measurements.

As experience was gained during the measurement program, it was found that the best results were obtained by frequently calibrating the instrument by measuring V_H. The new V_H was then used in calculating T^B by

$$T^B(i) = T_R(i) \cdot ((1 - R(i))/R(i)) + T_{amb}/R(i) \qquad (4.1)$$

where $R(i) = V_H(i)/V_{oil}(i)$ and i was the index of the sample frequency, $V_H(i)$ was the voltage measured at Freq(i) when looking at the hot and cold load, and $V_{oil}(i)$ was the voltage measured while looking at the oil.

This re-calibration was accomplished after each set of T^B measurements were completed on a given oil thickness. All measurements completed after 17 December 1993 were conducted in this manner.

As with any real data collection system, measurements were collected that created problems with the processing and interpretation of results. Most notably, in measurements before 17 December 1993, a large conversion loss at 30 GHz caused the T^B samples near this frequency to be noticeably low during the December measurements; in the October measurements there was a large loss at 32.0 GHz. In all of the comparisons to follow, data points for all of the data sets of the days shown below are interpolated from the two neighboring measurements.

Date	Interpolated point
8 Oct. 1993	32.0 GHz
2 Dec. 1993	30.0 GHz
9 Dec. 1993	30.5 GHz
14 Dec. 1993	30.1 GHz

All of the uniform depth measurements used in this report were conducted using the radiometer set-up on the roof of the main laboratory building. Since the Lincoln Laboratory is a radar testing facility, no control can be exerted over signals radiating from the rooftop antennas within the radiometer bandwidth. On some occasions, unrealistically high T^B measurements were recorded. It was found that these bad measurements were limited to a small span of time. When the measurement was repeated one to two minutes later, the expected result was obtained. It was suspected that the errors are due to nearby millimeter wave (MMW) transmissions of short duration. During this same time period (late December 1993), a degradation in the output performance of the sweep oscillator

was experienced. It was unclear if local MMW radiation or the degradation in sweep oscillator performance caused the unrealistic T^B measurements during this time period; however, no suspect measurements are used in any of the comparisons for this report. The sweep oscillator was repaired in January 1994. Recent measurements taken with the radiometer on the rooftop occasionally have produced spurious readings, however when repeated minutes later, the measurement was fine.

4.2 UNIFORM OIL THICKNESS MEASUREMENT RESULTS

This section describes specific comparisons made with the data collected by the FSR using uniform oil layers at selected thicknesses. In each comparison of measured data, an a theoretical prediction of the oil brightness temperature is shown.

A complete set of uniform thickness measurements for each of the following comparisons are included in Appendix A. Selected measurements are used in the following sections as illustrations for comparison purposes. Theoretical predictions for each of the comparison types were made using Equation (2.6). The dielectric constant of the oil, water salinity and temperature were held constant, and the ambient temperature was adjusted so that the predicted T^B of water was close to an actual measured value.

The comparisons made in this section will show that the expected T^B response is independent of oil type, day/night variation, and ambient weather conditions. Additionally, the ability of the FSR to measure thin oil layers will be shown.

4.2.1 <u>Different Oil Types</u>

Three different oil types were used during the proof-of-principle experiments, namely a heavy pump oil, a light fuel oil (kerosene) and North Slope Crude Oil. This first set of comparisons shows that the oil brightness temperature versus frequency for a given uniform thickness of oil is consistent for different types of oil over the range of oil layer thickness examined. In addition to the actual data, a set of theoretical predictions is shown.

Date	Oil Type	Ambient Conditions
8 Oct. 1993	Pump oil	Day, mostly sunny, high cirrus clouds, 26° C
17 Dec. 1993	Kerosene	Night, clear sky, 1° C
15 Feb. 1994	Crude oil	Day, partly sunny, high stratus clouds, 9.5° C

At thicknesses less than 3 mm, the pump oil and in some cases the crude oil created clumpy and patchy areas without full coverage of the water in the test tank. Because the oil thickness was not considered uniformly distributed, comparisons of the three oil types as a function of these depths was not undertaken.

Figures A-1 to A-8, found in Appendix A, provide a complete set of the curves comparing the three oil types at oil thicknesses of 3 mm to 9 mm in 1 mm steps. The water brightness temperature along with 4 mm and 9 mm oil thickness measurements are included in this section for illustrative purposes.

Figure 4-1 shows the measured brightness temperature as a function of frequency for water only (0 mm oil). Because the brightness temperature is a function of ambient conditions, large variations in the T^B mean can be expected on a daily basis with small variations over a measurement time frame. Shifts of the mean may be due to either thermal-gain drift within the instrument or sky temperature variations or both. Prior to using frequent recalibration, rising means over the duration of a measurement set were common. What is important to bear in mind, in spite of the daily variations in absolute T^B, is that the resulting T^B curves follow the **shape** of the expected (theoretical) brightness temperature curve. All of the curves in Figure 4-1 exhibit a linear slope as a function of frequency similar to the theoretical prediction for water.

Referring to Figure 4-2, results of the 4 mm measurements show very good agreement between the pump oil, kerosene and crude oil data sets. The mean value of the measured points is above the T^B for water. Above 30 GHz, all of the measurements follow the rising slope of the theoretical prediction while below 30 GHz the pump oil and kerosene curves exhibit slight inflection.
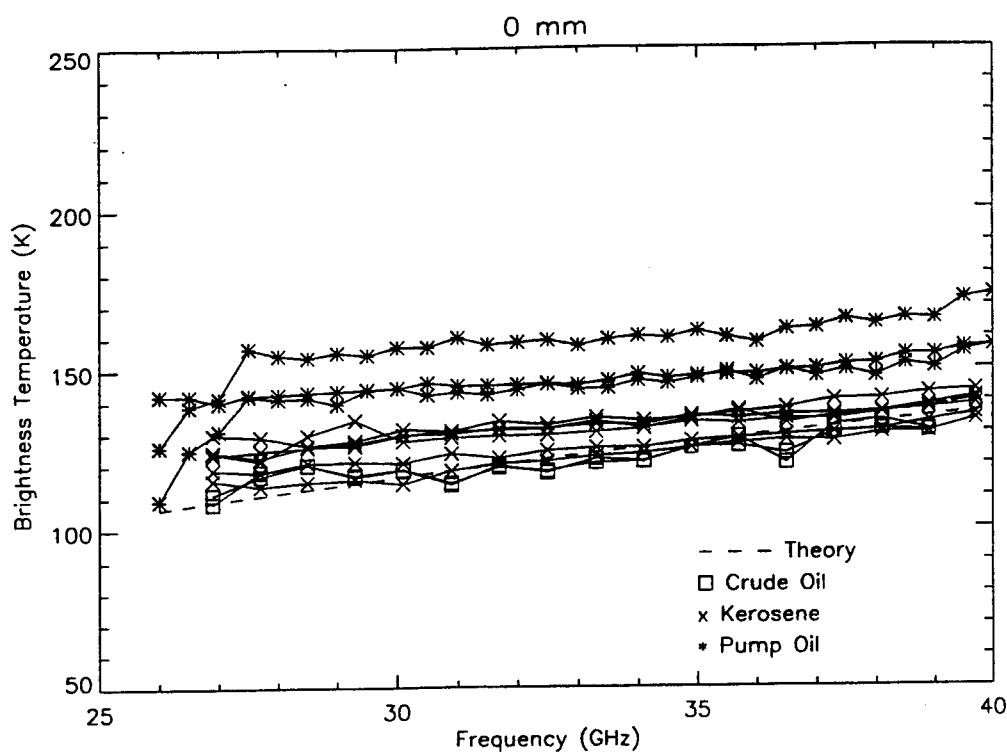
Figure 4-1. Oil Type Comparison, Water Only Measurement
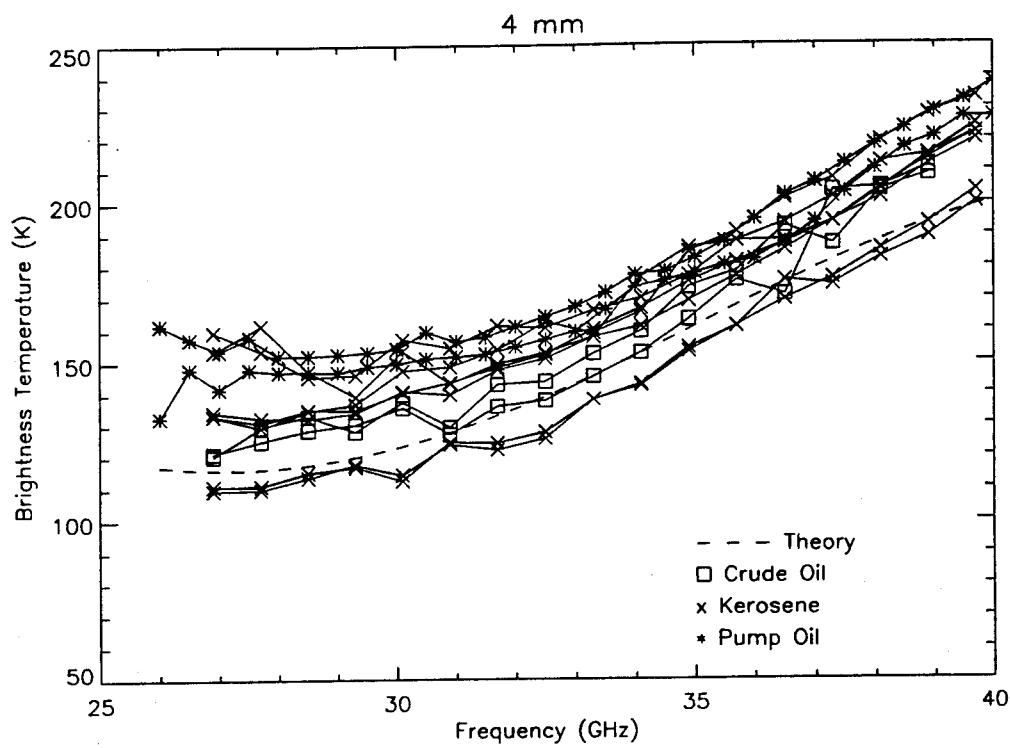
Figure 4-2. Oil Type Comparison, 4 mm Uniform Thickness

4 - 7

At 9 mm, Figure 4-3, the sinusoidal variation of T^B vs. frequency is quite evident. The complete measurement data set, shown in Appendix A, matches the shape of the theoretical prediction quite well.

Since the curves for the different oils exhibit similar properties for each depth examined, and compare favorably to the characteristics predicted by theory, it can be postulated that the T^B responses for pump oil, kerosene, and crude oil have similar characteristics. With this in mind, field measurements of actual oil thicknesses can be performed using predetermined theoretical profiles for ambient conditions and oil type; there is no need to sample the oil to obtain an a-priori dielectric constant estimate. The ambient water conditions can be measured by the radiometer to set the operational parameters for that measurement day. During the course of this experiment, kerosene was used as the primary measurement target because it was easy to obtain, easy to clean-up, and could produce thin uniform oil layers.
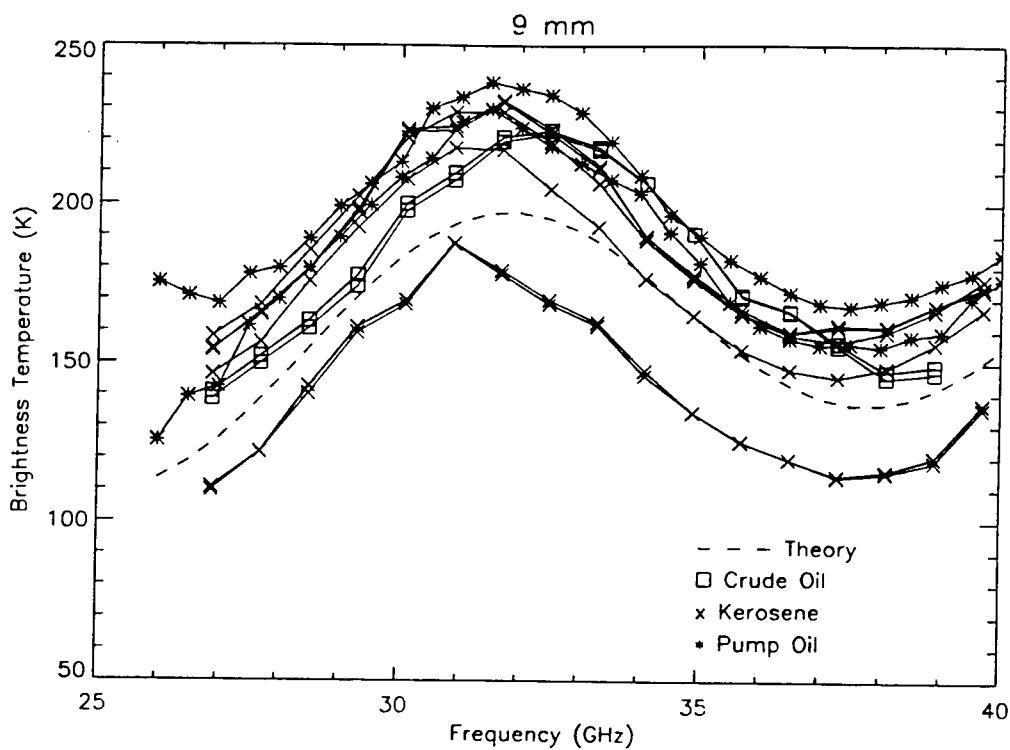
Figure 4-3. Oil Type Comparison, 9 mm Uniform Thickness

4.2.2 Day versus Night

For a comparison of day versus night conditions, two data sets were chosen. This set of comparisons shows that the T^B vs. frequency relationship for a given thickness of oil is consistent over the diurnal period. In both day and night measurements the same type of oil was used, namely, kerosene, and the ambient temperatures are close. The cloud cover conditions were quite different.

Date	Oil Type	Ambient Conditions
2 Dec. 93	Kerosene	Day, overcast, 7.9° C
17 Dec. 93	Kerosene	Night, clear sky, 1° C

Figures A-9 to A-23 provide a complete set of the curves comparing the two conditions at oil thicknesses from 1 mm to 9 mm in 1 mm steps. The water brightness temperature along with 1 mm, 4 mm and 8 mm oil thickness measurements are included in this section for illustrative purposes.

Figure 4-4 illustrates the measured and predicted brightness temperatures for water. At a 1 mm oil depth, shown in Figure 4-5, the rise in brightness temperature above water is easily observed, and the T^B curve appears as a straight line with a positive slope. The sinusoidal variation of T^B is not evident at this oil depth because the frequency of the T^B variation is too low to be measured across the Ka-band. All of the measured day/night variation curves exhibit this positive slope feature.

As shown in Figure 4-6, at the 4 mm oil depth, the measured data curves again follow the shape of the theoretical prediction. At this oil thickness, the sinusoidal variation is beginning to become apparent between 26 - 29 GHz. The T^B curve is at a minimum between these points.
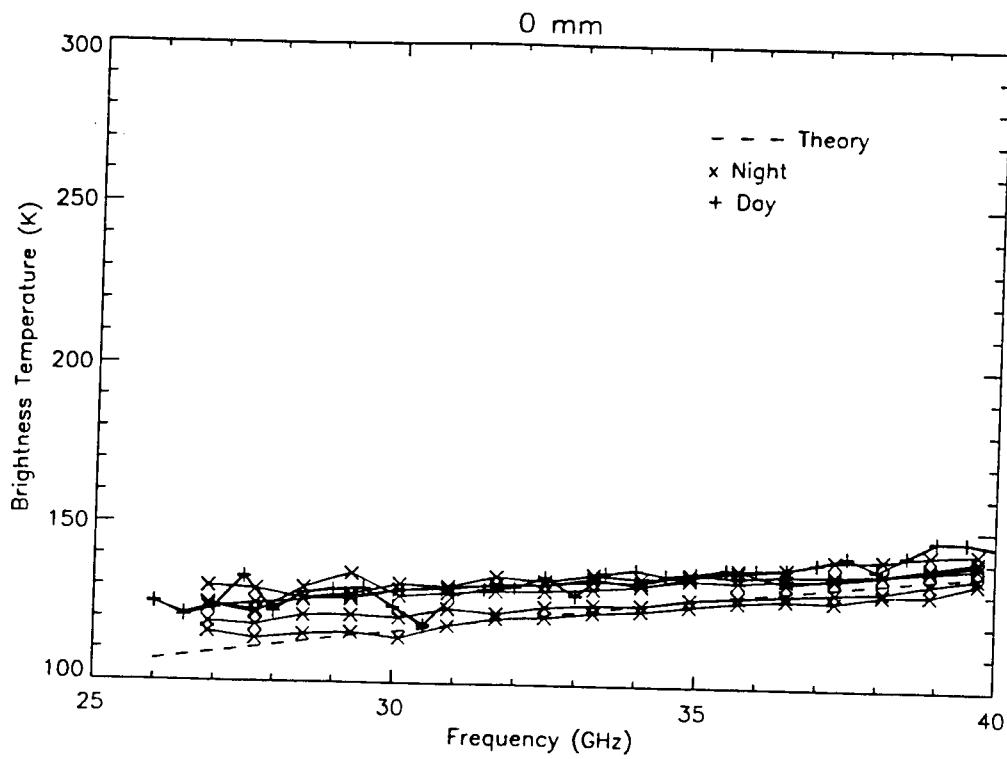
Figure 4-4. Diurnal Comparison, Water
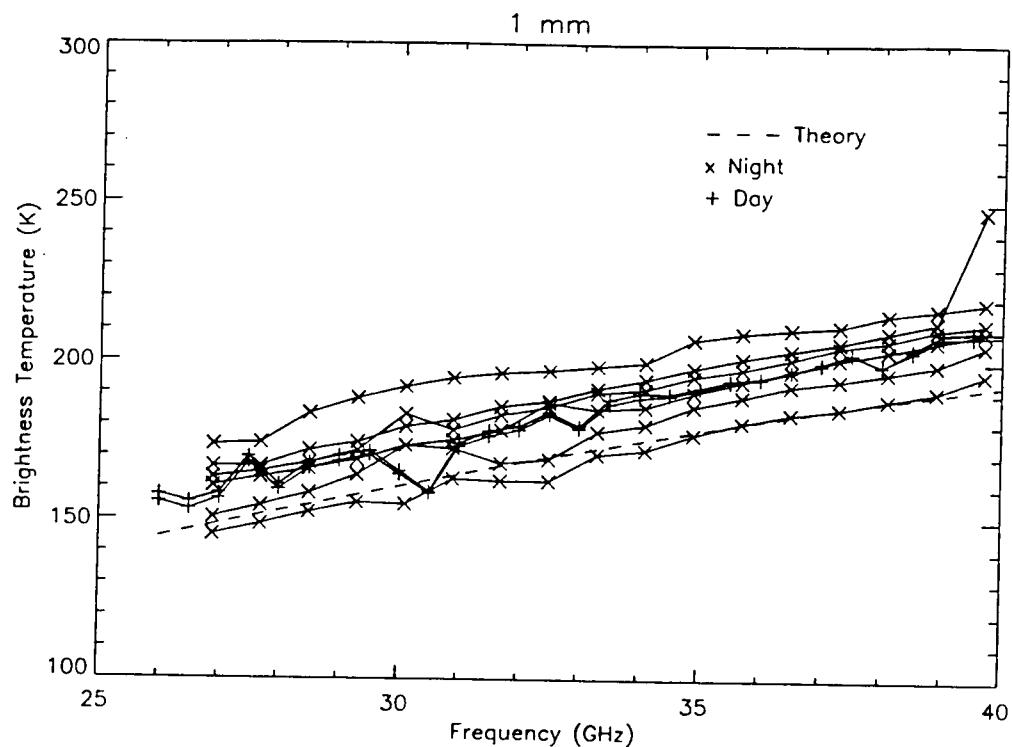
Figure 4-5. Diurnal Comparison, 1 mm Uniform Thickness

Figure 4-7 shows the measured data points for the 8 mm oil thickness. In this plot, the points taken during the day measurements appear to have a different T^B variation frequency. Upon reviewing the technique used to measure the oil volume added, an error was found in the oil volume added to the tank during the transition between the 4 mm layer and the 5 mm layer. An additional 0.5 mm layer was accidentally added. When this was taken into account, the plots of the 2 Dec. 93 daytime measurements agree well with the theoretical predictions. An example of this is shown in Figure 4-8, with additional examples provided in Appendix A. The measured data shown in Figure 4-8 seems to exhibit large jumps; it is believed that the aberrant data points below 30 GHz and above 39.5 GHz were a precursor to the sweep oscillator RF module failure.

Based on the favorable comparisons of T^B measurements taken over day/night periods, including Figures A-9 to A-23, it has been shown that the FSR can measure oil thickness characteristics without regard to diurnal variation.

Figure 4-6. Diurnal Comparison, 4 mm Uniform Thickness

8 mm
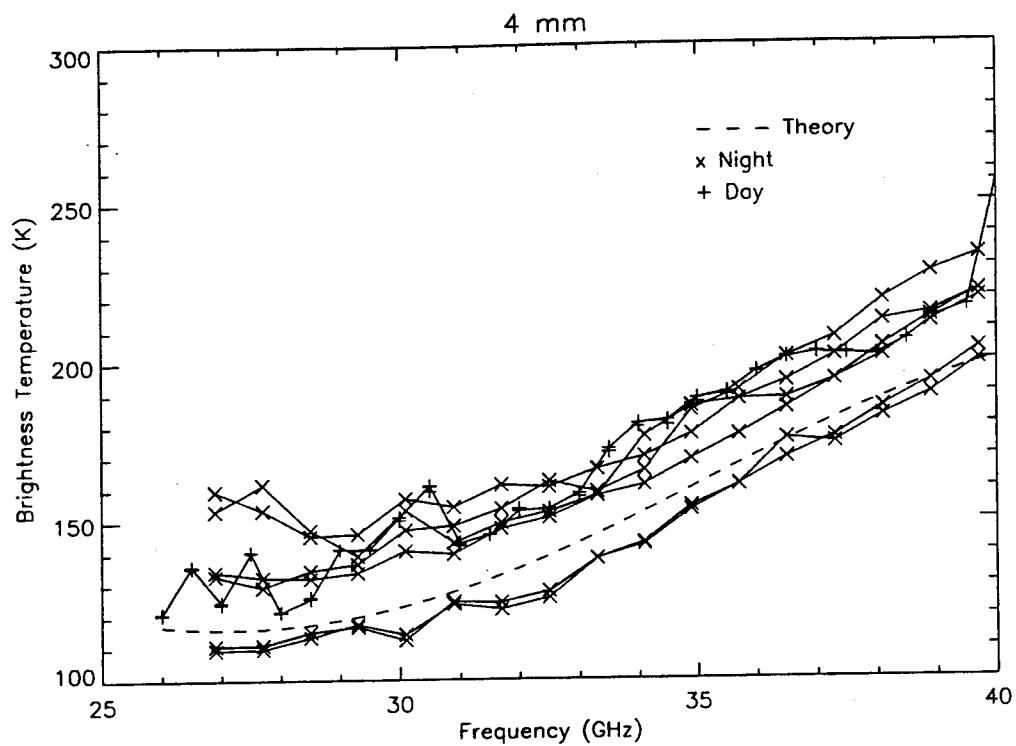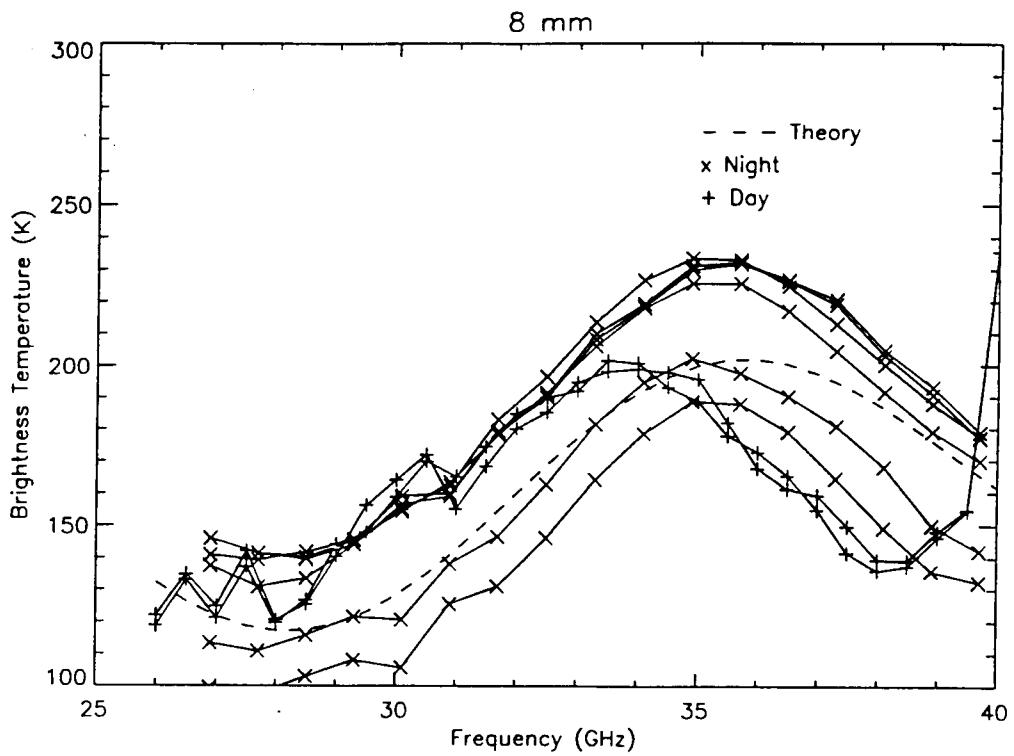
Figure 4-7. Diurnal Comparison, 8 mm Uniform Thickness
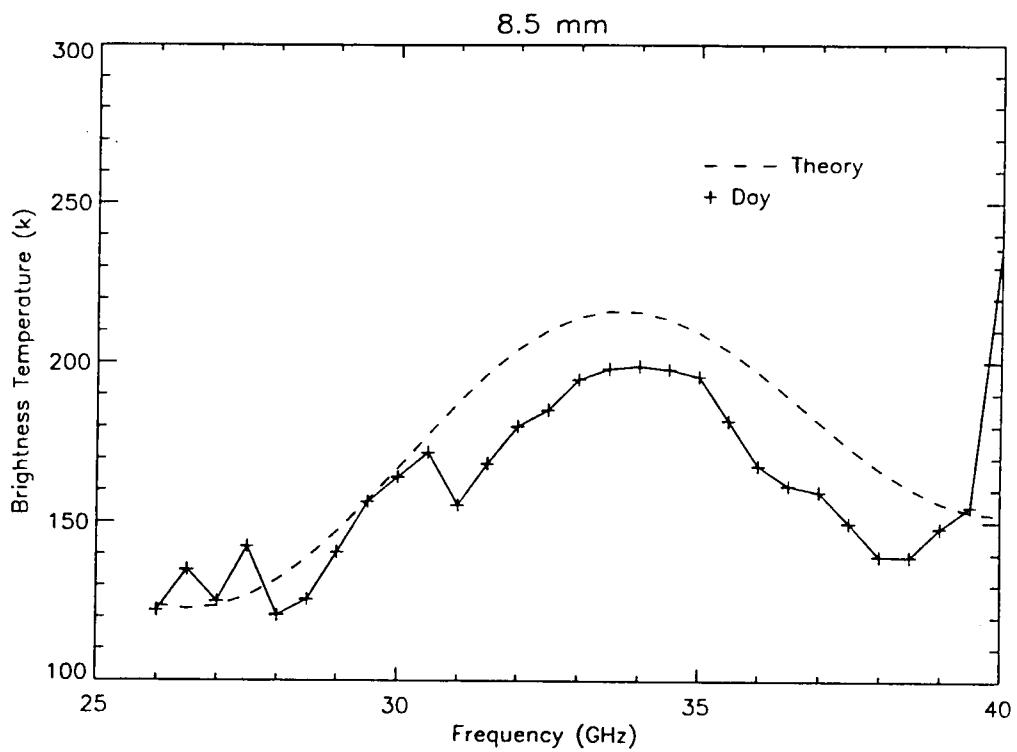
8.5 mm

Figure 4-8. Diurnal Comparison, 8.5 mm Estimated Uniform Thickness

4.2.3 Different Daytime Weather Conditions

Data was collected under different daytime weather conditions. This comparison illustrates that the expected T^B vs. frequency response is independent of weather conditions. Measurements were conducted under sunny conditions and at a later date, collected under an overcast sky in a light drizzle. In both cases the same type of oil was used.

Date	Oil Type	Weather Conditions
8 Oct. 1993	Pump oil	Mostly sunny, high cirrus clouds, 26° C
15 Oct. 1993	Pump oil	Overcast, slight drizzle, 12° C

The measurements taken on 15 October 1993 do not contain a measured water T^B curve. The theoretical predictions for this day were based on using the 4 mm oil layer as the calibration source. Additionally, no measurements were made on 15 October at oil depths less than 4 mm because, based on the experience of 8 October, the viscous pump oil would not form a uniform thin layer.

Figures A-24 to A-29 contain the provide a set of curves comparing the two conditions at oil thicknesses from 4 mm to 9 mm in 1 mm steps. The 4 mm and 8 mm oil thickness measurements are included in this section for illustrative purposes.

Figure 4-9 illustrates the T^B response measured at the 4 mm uniform layer thickness under clear and overcast with drizzle conditions. Both measurements consistently follow the theoretical prediction.

Figure 4-10 illustrates the measured T^B response for a 7 mm uniform layer thickness; note that the 7 mm curve has a characteristic dip at mid-band. The measured oil brightness temperatures again consistently follow the prediction.
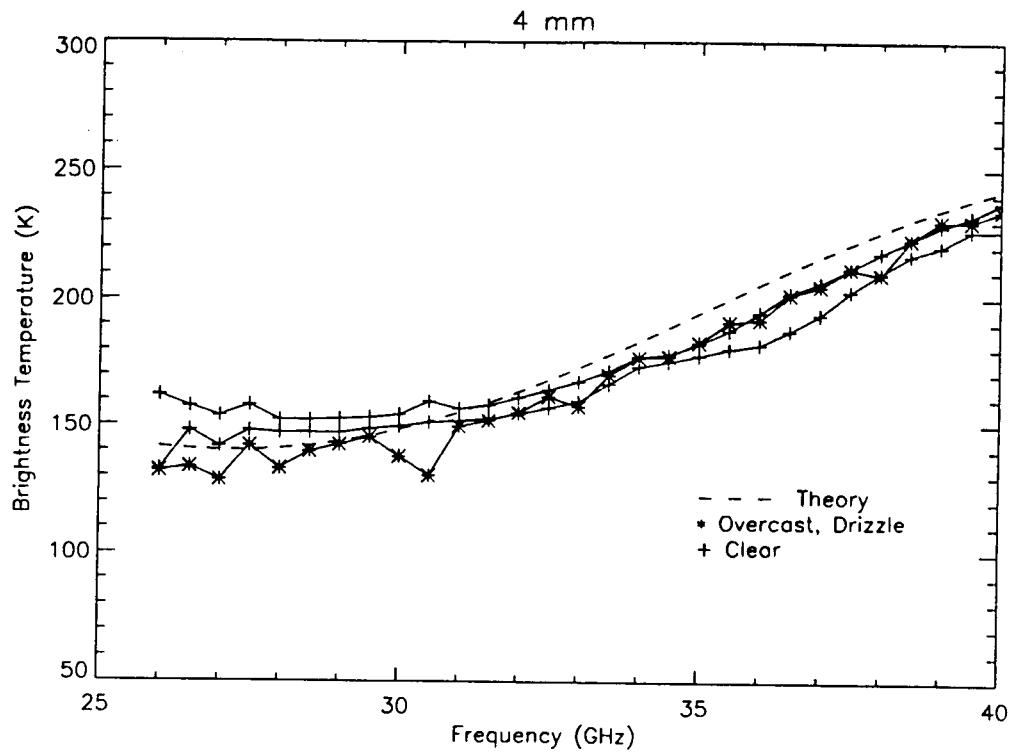
Figure 4-9. Weather Comparison, 4 mm Uniform Thickness
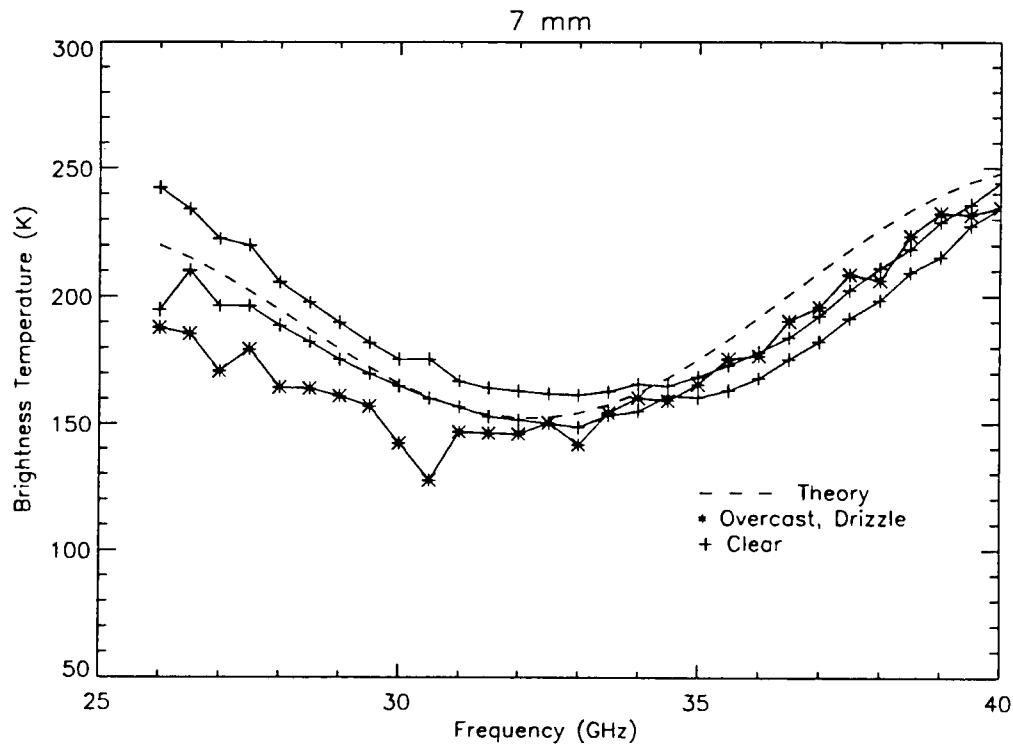
Figure 4-10. Weather Comparison, 7 mm Uniform Thickness

Based on the favorable comparisons of T^B measurements taken under distinctly different weather conditions, including Figures A-24 to A-29, it has been shown that the FSR can measure oil characteristics under clear and rainy conditions.

4.2.4 Response at Small Increases of Thickness

Thin uniform oil layers were measured on 23 March 1994 using kerosene. The oil thickness was increased in increments of 0.1 mm, starting with a water background (0 mm) to a final oil thickness of 1.0 mm. The FSR was re-calibrated using a hot load between each T^B measurement, and water T^B was measured often to verify that the apparent offset in brightness temperature above water was in fact due to the presence of thin layers of oil. Figure 4-11 shows that the uniform oil layers of 0.2 mm and 0.5 mm have a slightly higher T^B than water. The slope of the oil measurement curves is nearly the same as water, however, the rise in mean T^B is measurable and conforms to the expected rise due to the $\sin^2$ relation of increasing depth. Figure 4-12 shows the results for depths of 0.7 mm to 1.0 mm compared to water.

To create these thin layers, 10 ml of oil were added to the test tank for each step. Small oil measurement errors due to liquid remaining in the graduated cylinder after pouring could cause mis-registration of oil depth. It is believed that this effect might have occurred because the predicted curves shown in Figure 4-12 actually correspond to depths as follows:

Measurement Depth (mm)	Theoretical Depth (mm)
0.7	0.525
0.8	0.675
0.9	0.775
1.0	0.875

Note the increase in slope and higher mean T^B characteristic at oil thicknesses of 0.7 mm and above. Clearly, with a well-calibrated, stable instrument, thin uniform oil layers can be measured by the FSR.
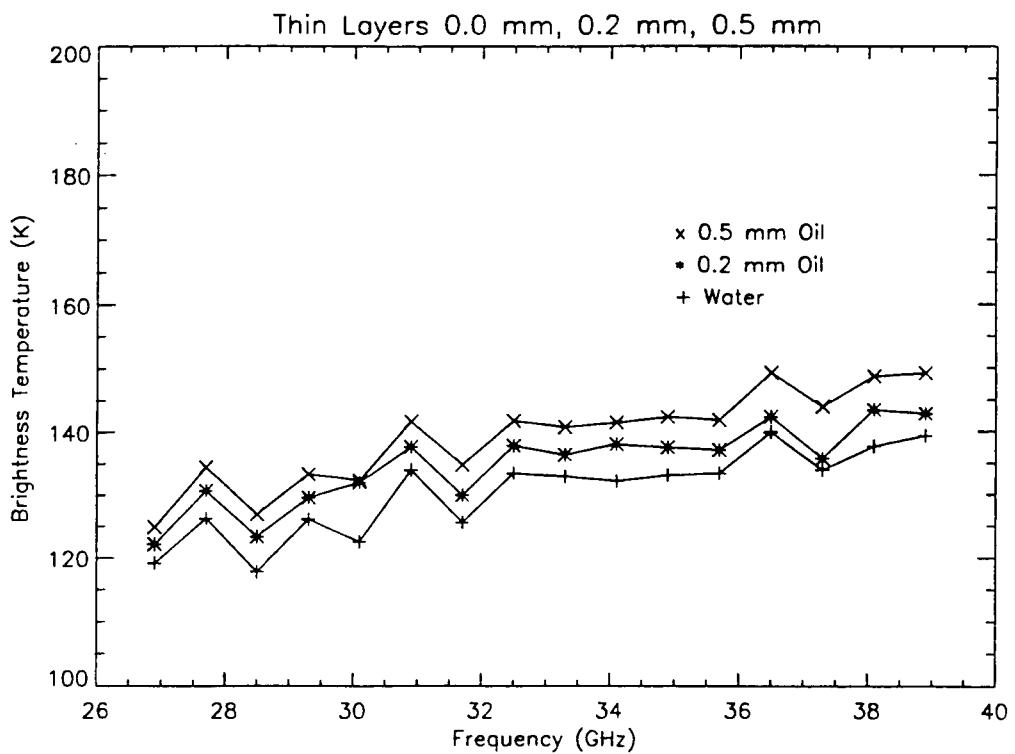
Figure 4-11. Thin Uniform Layers, 0.0 mm, 0.2 mm, and 0.5 mm
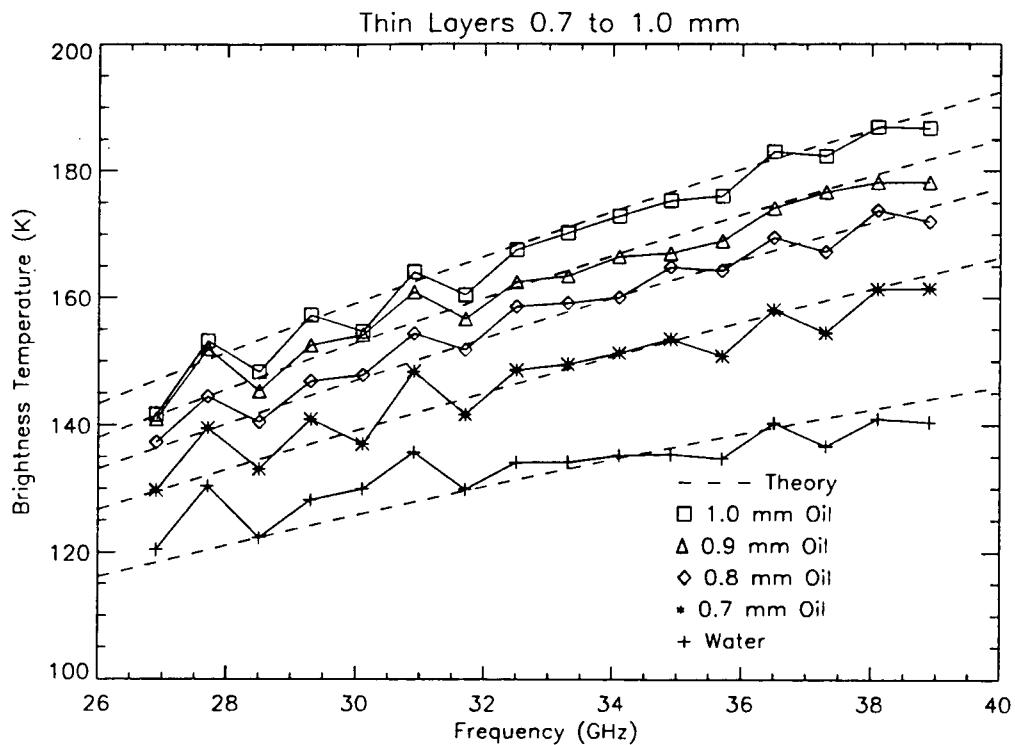
Figure 4-12. Thin Uniform Layers, 0.0 mm, 0.7 mm to 1.0 mm

4.3 EMULSIFIED OIL

Emulsions of oil and water were made by mixing SAE10W30 motor oil with water such that the percentage of oil and water was known. The three different emulsions were produced that contained 20% water, 40% water, and a saturated emulsion containing approximately 56% water by volume.

To produce the 20% water/oil emulsion, 100 ml of water were mixed with 400 ml of oil. The 40% water/oil emulsion contained 200 ml of water and 300 ml of oil. The third emulsion was made by adding measured quantities of water to oil and mixing the liquid until no additional water would mix with the emulsion. After mixing and settling, the remaining water volume was measured. Approximately 260 ml of water had mixed with 200 ml of oil, creating a 56% water/oil emulsion.

The 20% and 40% emulsions were created by using a hand-held blender, and mixing until the liquid had a consistent texture. The saturated emulsion was created by using a shaker at 2.6 cycles over a 12-inch stroke for 5 minutes. The shaking frequency was then increased to 60 cycles for 23 seconds. The emulsion was allowed to stand for 1 hour, then the remaining water was decanted and measured.

Date	Percentage Water	Ambient Conditions
15 Feb. 94	56%	Day, sunny, clear, 5.6° C
4 Mar. 94	20%	Day, sunny, 7° C
4 Mar. 94	40%	Day, sunny, 7° C

The emulsified oil was opaque and viscous which made measuring the exact oil volume quite difficult. As much as 9 ml was found to remain in the 100 ml graduated cylinder after pouring and letting the remaining emulsion in the graduated cylinder settle.

Figures B-1 to B-7 provide a complete set of measured brightness temperature plots for water and emulsions as a function of frequency for emulsion depths of

approximately 1, 3, 5, 7, 9, and 10 mm. The 1 mm and 5 mm emulsion thickness T^B measurements are included in this section for illustrative purposes.

Figure 4-13 illustrates the measured T^B response for an approximately 1 mm thickness of emulsified oil. Clearly, the measured brightness temperatures are higher than theoretical predictions for pure oil at the same uniform thickness; this is not an unexpected result. Also apparent is that the trend of the 20% emulsion seems to follow the trend of the 1 mm pure oil prediction. Based on just the large increase in brightness temperature over water, the presence of an water/oil emulsion can be detected.

A 5 mm emulsion is illustrated in Figure 4-14. Again, the measured T^B responses are higher than theoretical predictions for pure oil at the same uniform thickness, and the 20% emulsion shows a trend similar to the 5 mm pure oil characteristic.

The rise in T^B above water for the emulsions clearly indicate the presence of oil. At a 20% by volume water/oil emulsion, the dielectric constant has not increased significantly [reference 14], so the trend of the measured T^B curves should not differ considerably from the theoretical prediction for non-emulsified oil. For emulsions above 30% water by volume, the real and imaginary parts of the dielectric constant increase considerably above the nominal value resulting in the observed elevation of T^B across the FSR band. This is not an unexpected result. Consistent with previous simulations and experimental results [reference 14], the FSR T^B measurements of water and oil emulsions show elevated brightness temperatures between 200 and 250 K with less sinusoidal variation in T^B. The higher mean brightness temperature is attributed to the change in both the real and imaginary terms of the complex dielectric constant; the electrical length of the oil layer is increased and more noise is generated from the oil itself [reference 14]. The reduction in the amplitude fluctuation ($\sin^2$ response) term is also attributed to a rise in the ε of the oil. The larger ε results in a higher refractive index, n_o. An increase in n_o results in an increase of the field reflectivity at the oil water interface, $r_{o/w}$. Recall that $\rho_{ow} \equiv r_{ow}^2$, and refer to Equation (2.7). As ε increases, ρ_{ow} increases, decreasing the multiplicative term $(\rho_{aw} - \rho_{ow})$. This creates a smaller amplitude fluctuation term which in turn damps the sinusoidal response of T^B.

1 mm EMULSION
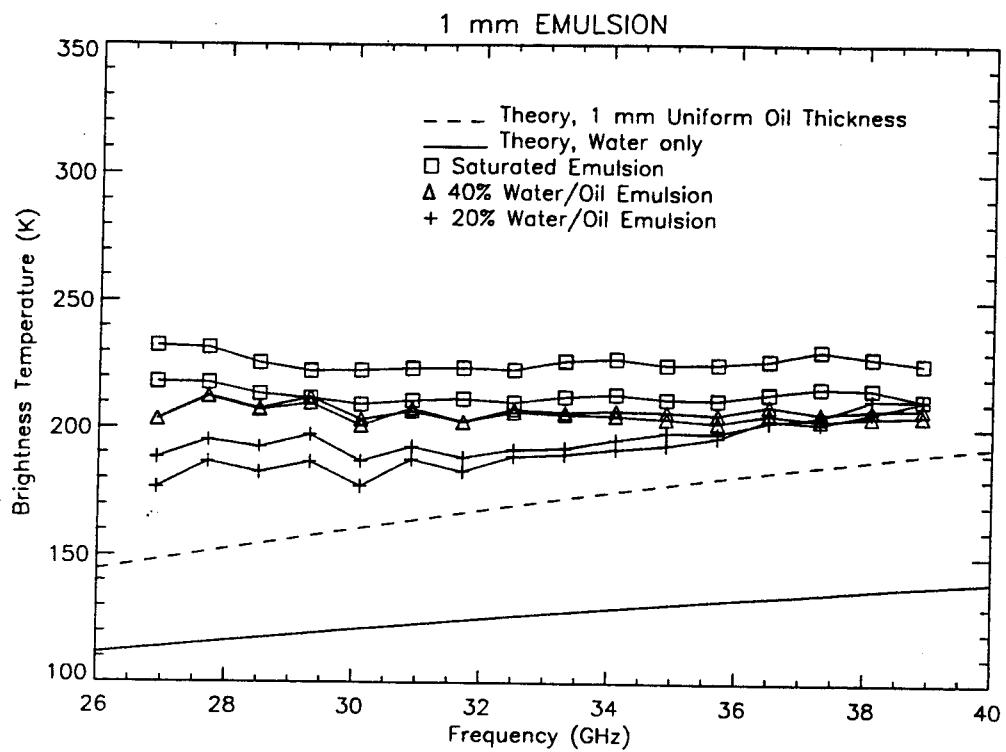
Figure 4-13. Emulsified Oil, 1 mm Thickness

5 mm EMULSION
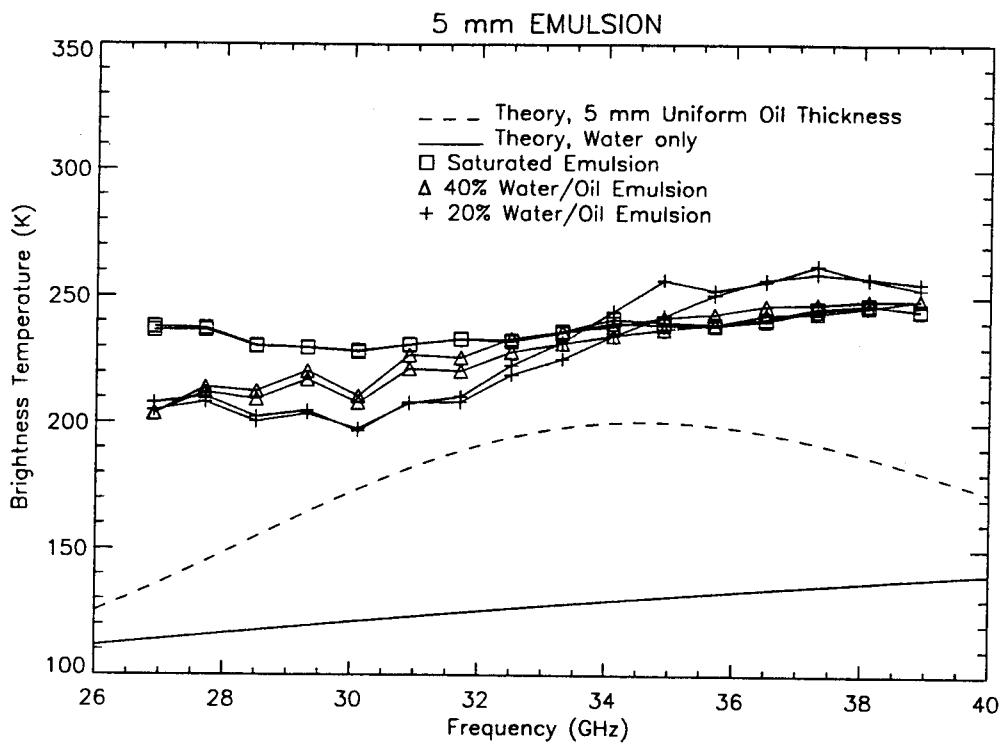
Figure 4-14. Emulsified Oil, 5 mm Thickness

4.4 NON-UNIFORM OIL THICKNESS MEASUREMENTS

Measurements of non-uniform oil thicknesses were undertaken to understand the phenomenology of various real-world oil slick characteristics. These measurements included split aperture uniform depth measurements, step thickness functions, step thickness gradients, and patchy oil . A brief description of the measurement and the real-world characteristic it is modeling follows.

1. Split Aperture Uniform Depth Measurement. The split aperture uniform depth measurement was considered as the first experiment for measuring different uniform oil depths within the antenna aperture. The measurement tank was divided in half using a piece of Plexiglas. Various combinations of two uniform thicknesses that each covered 50% of the antenna field of view were measured. The split aperture measurements simulated a distinct step in oil-layer thickness as might be encountered in a "windrow" situation.

2. Step Thickness Function. A step function of oil was created by using a vertical mylar cylinder to enclose an area in the antenna field of view where thicker oil was constrained to a single depth. The oil filled cylinder was surrounded by sheen oil to simulate "tarballs" and glob-shaped oil masses within a thin oil slick. The area covered with step thickness function oil within the antenna field-of-view was approimately 60%; the remaining 40% of the area within the antenna field-of-view was covered with an oil sheen.

3. Step Thickness Gradient. The step gradient measurement setup was similar to that used for the step function experiment, however, instead of one distinct oil thickness against a background, six distinct oil thicknesses were created by using concentric mylar cylinders to constrain the oil. This experiment was meant to simulate a transition from thin to thick oil within an instantaneous field of view. This occurrence might be seen in a windrow or along the edge of an oil slick. The area covered with step gradient oil within the antenna field-of-view was approimately 80%, the remaining 20% of the area within the antenna field-of-view was water.

4. Patchy Thicknesses. The patchy oil experiment created three randomly spaced defined areas of measured oil thickness within the antenna field of view. This experiment simulated the response expected when multiple patches of oil or tarballs are measured. The area covered with patchy oil within the antenna field-of-view was approimately 50%, the remaining 50% of the area within the antenna field-of-view was water.

4.4.1 Split Aperture Uniform Depth Measurements

The split aperture uniform depth measurements were made on 11 January 1994 and 4 April 1994 as shown below. Results of each of the measurements are shown in Figures C-1 to C-11. Selected T^B vs. frequency plots are included in this section for illustrative purposes.

Date	Measurement Depth Tank Side A (mm)	Measurement Depth Tank Side B (mm)
11 Jan. 94	1	5
	2	5
	3	5
	4	5
	5	5
4 Apr. 94	0	1
	1	1
	1	2
	1	3
	1	4

The measurement tank was divided in half using a piece of Plexiglas. Uniform layers of oil (kerosene) were poured in each half of tank, with the antenna field of view set such that each uniform layer in the tank would make a 50% contribution to the T^B response. The antenna position for the initial water calibration was set such that it did not have the divider in the field of view. After the initial water

4 - 21

calibration, the antenna was moved so that the divider was in the field of view of the antenna, surrounded by water (no oil). The results of these measurements are shown in Figure 4-15. The presence of the Plexiglas divider in the background adds a small brightness temperature contribution against the water background. This increase in brightness temperature was taken into account in the theoretical prediction curves.

On 4 April 1994, after the initial setup, 50 cc of oil (kerosene) was added to one side of the tank, creating a 1 mm uniform thickness next to a water only area. The measured results and theoretical prediction is shown in Figures 4-16. The prediction was computed using a 50% contribution from water and a 50% contribution from a 1 mm oil layer. Note that the measured data falls nearly mid-way between the two uniform thickness predictions.

Next, 50 cc (1 mm) of oil was added to the water side of the tank, creating a 1 mm uniform layer throughout the tank. After the 1 mm uniform layer was measured, oil was added 1 mm at a time to one side of the test tank. After each addition of oil, a measurement was taken. This continued until half of the test tank was at an oil thickness of 4 mm. Figure 4-17 illustrates the theoretical prediction and measured T^B response for a 50% contribution of a uniform layer of 1 mm and a 50% contribution of a uniform layer of 2 mm. Note that the measured T^B has a nearly flat slope, as would be expected from a linear combination of a rising slope from a 1 mm layer and a descending slope from a 2 mm layer.

During an earlier test on 11 January 1994, a 5 mm layer was set on one side of the measurement tank and 1 mm layers were added to the thin oil side of the tank. Measurements were taken after each 1 mm increase, and oil added until both sides of the tank were at the 5 mm oil thickness. Figure 4-18 illustrates the theoretical prediction and measured T^B response for a 50% contribution of a uniform layer of 2 mm and a 50% contribution of a uniform layer of 5 mm. Note that the curve does exhibit traits of both the 2 mm and 5 mm uniform layer curves, namely, the 5 mm trait of peaking at approximately 35 GHz, and the 2 mm trait of a fairly flat to somewhat negative slope.
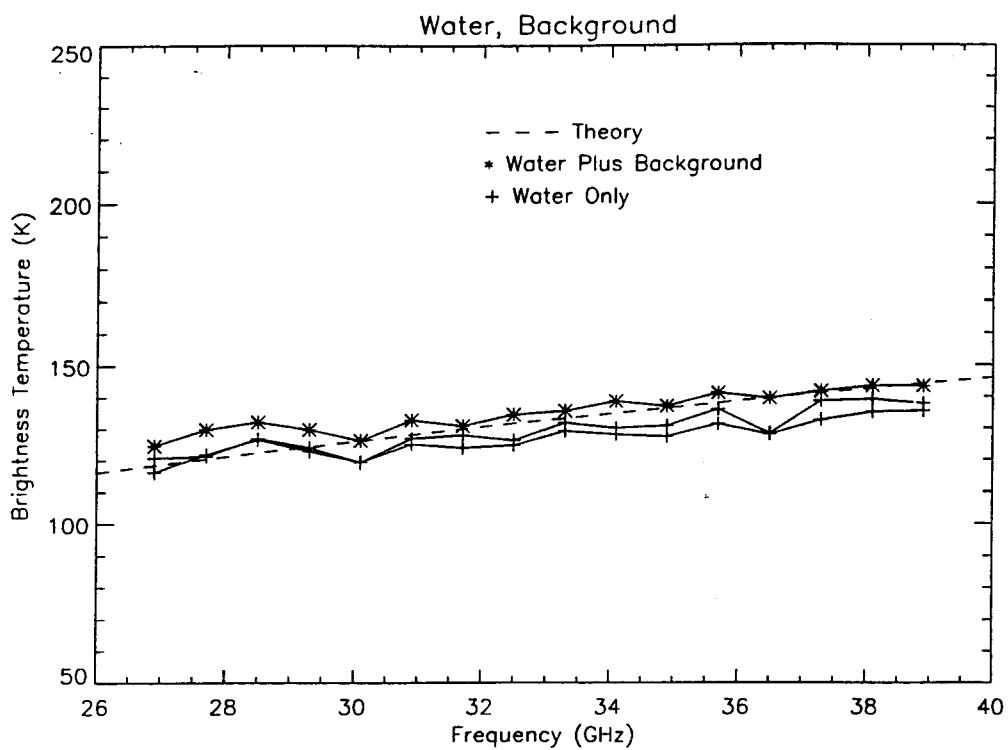
Figure 4-15. Split Tank Measurement, Water and Background
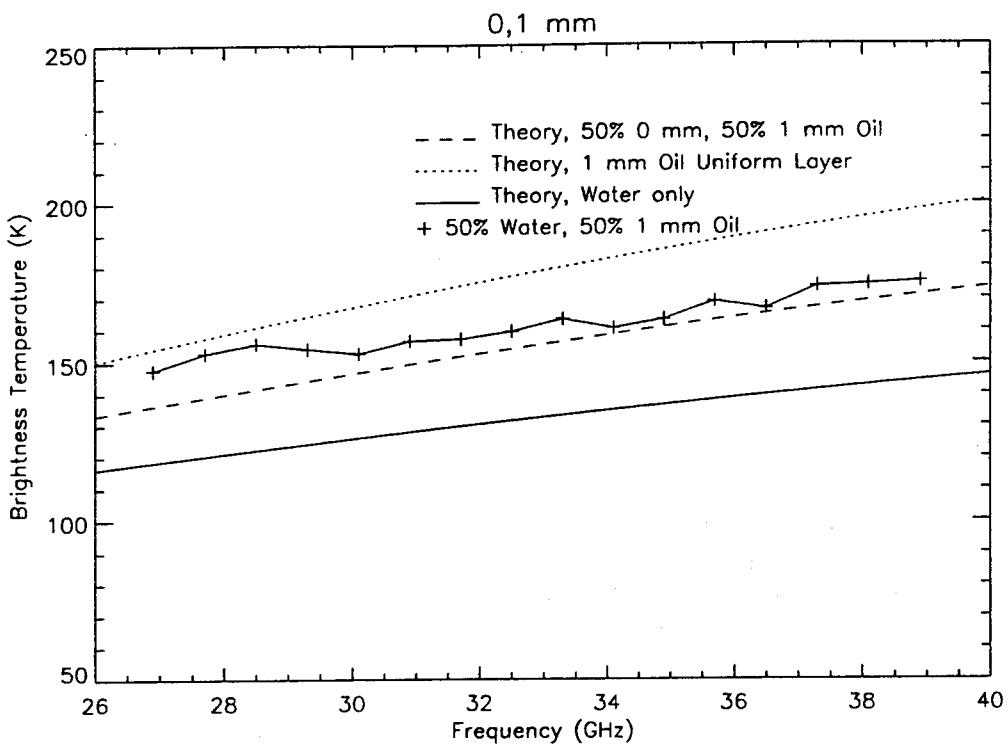
Figure 4-16. Split Tank Measurement, 0 mm and 1 mm Oil
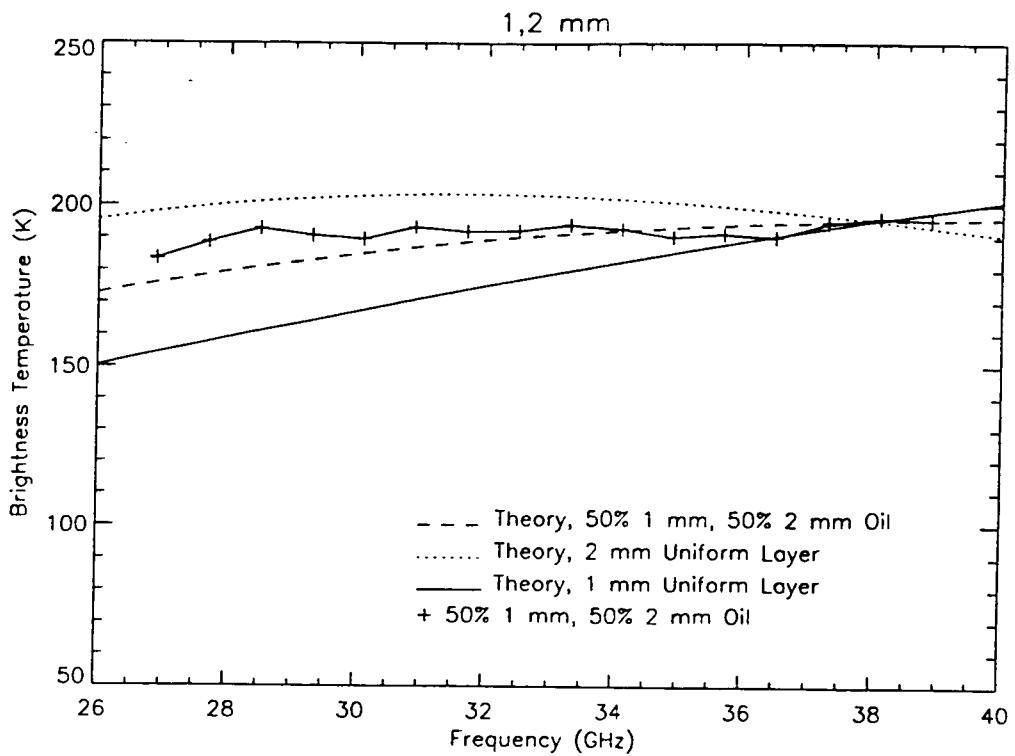
Figure 4-17. Split Tank Measurement, 1 mm and 2 mm Oil
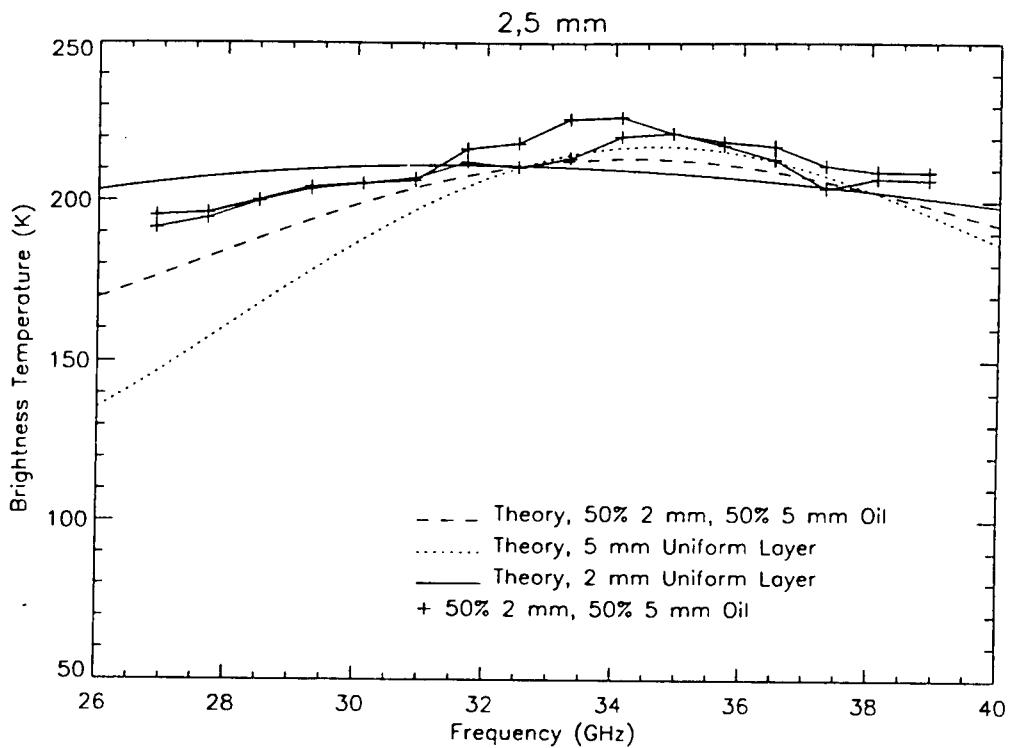
Figure 4-18. Split Tank Measurement, 2 mm and 5 mm Oil

4-24

In all cases examined for the spit tank measurements, including Figures C-1 to C-11, the presence of oil is detectable by the increase in T^B. Combinations of the characteristic traits of each of the oil thicknesses can be seen in the split tank results.

4.4.2 Step Gradients of Oil

Two experiments investigated the response of step gradients of oil thickness. In one experiment, a step function of a given oil thickness was created by using a single mylar cylinder, placed vertically in the test tank to create a single step between the surrounding liquid and oil. The second experiment used six concentric mylar cylinders to create a staircase (wedding cake) gradient of oil using seven discrete oil thicknesses, from the water background to a maximum oil depth. The oil type used in both experiments was kerosene.

4.4.2.1 Step Thickness Function

A step function of given oil thickness was created by using a single mylar cylinder, placed vertically in the test tank to create a single step between the surrounding liquid and oil. The FSR antenna was placed such that half of the antenna pattern would view the liquid surface surrounding the tube, while the other half of the antenna pattern would be filled with the cylinder containing oil. The diameter of the mylar tube was 7.0 cm, which created a surface area of 38.5 cm^2; thus 3.85 cc of oil were added for each mm of oil thickness. Measurements were conducted on 2 March 1994, at six specific oil thicknesses inside the enclosed cylinder, from 1 mm to 6 mm, in 1 mm steps, with the surrounding liquid surface covered with approximately 0.5 mm of oil. Figures C-12 to C-21 provide plots of all of the results from this experiment. Selected plots are shown here for illustrative purposes.

Figure 4-19 shows the measured water T^B response and response for the background oil and mylar tubes. The background oil layer was estimated to be a uniform layer approximately 0.5 mm thick.
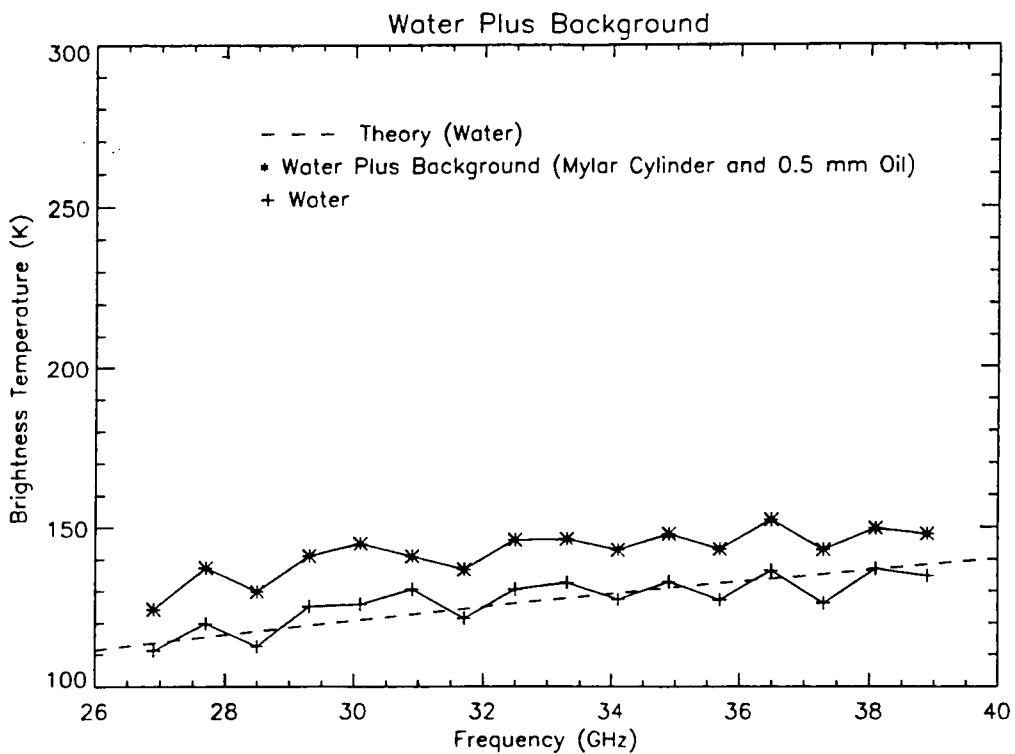
Figure 4-19. Step Function, Water and Background

Figure 4-20 is a plot of the measured brightness temperature response for a 5 mm step, occupying approximately 60% of the antenna field of view, against a uniform background of 0.5 mm oil. Note that the measured curve appears to peak at 32 GHz instead of the expected 35 GHz peak. Using this information, a revised estimate of the oil thickness shows that a 5.5 mm step occupying 60% of the antenna beam fits the measured data, Figure 4-21. This is an example of how oil thicknesses can be estimated visually by curve fitting techniques. All of the results shown in Figures C-12 to C-21, after adjustment for the estimated oil thickness, agree well with the theoretical predictions.
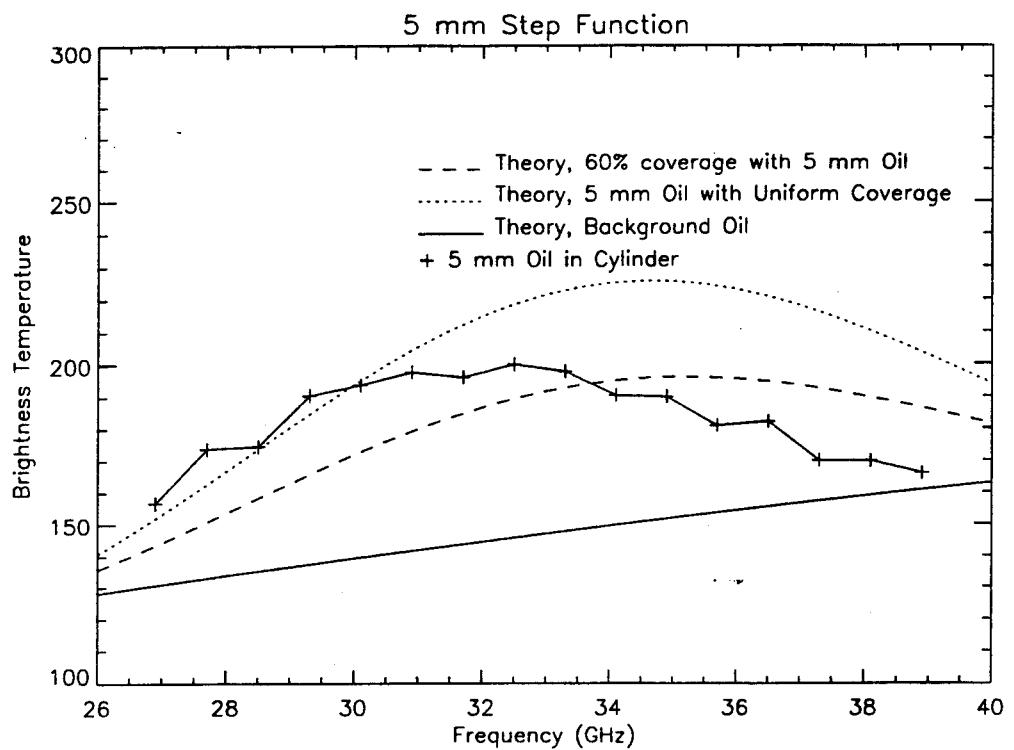
5 mm Step Function

Figure 4-20. Step Function, 5 mm Oil
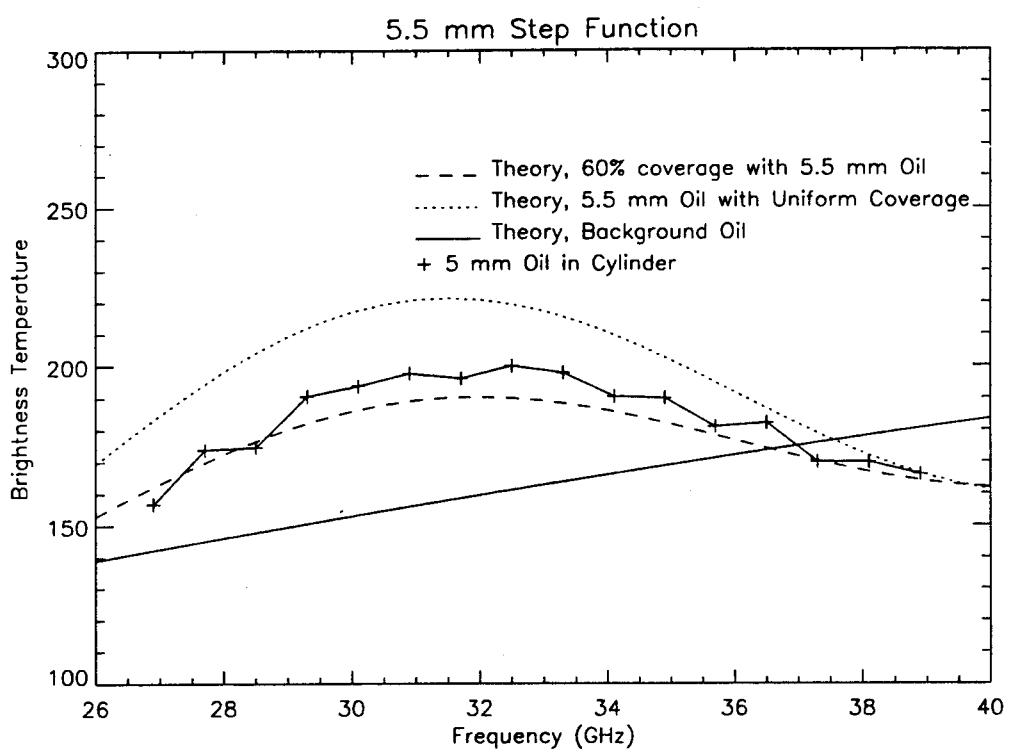
5.5 mm Step Function

Figure 4-21. Step Function, 5.5 mm Oil Estimate

4.4.2.2 Step Thickness Gradient

An experiment, conducted on 4 March 1994, investigated the response of multiple step gradients of oil, from a background of no oil (water), progressing in five steps from 0.5 mm to 2.5 mm, with the final progressive step either at 3 mm, 6 mm, or 9 mm. Each oil thickness gradient was contained within a vertical mylar cylinder, and these six cylinders were placed concentrically in the test tank, within the full beam of the antenna.

The diameter, enclosed surface area, and oil volume is shown below for the set of concentric rings used for the multiple step gradient test.

Ring Number	Diameter (cm)	Enclosed Area (cm²)	Oil Volume (cc)
1	2.8	6.16	1.85 per 3.0 mm
2	3.4	9.08	0.75
3	4.8	18.1	1.80
4	5.5	23.8	0.855
5	6.2	30.2	0.640
6	6.8	36.3	0.31

Figures C-22 to C-25 provide the T^B versus frequency plots for these measurements. The results of these measurements did not track well with the theoretical prediction curves. The presence of oil was detected by the slight rise in T^B over most of the band. Because of the small percentage contribution from each thickness, no obvious shape characteristic is observed as is observed in other non-uniform layer measurements.

4.4.3 Patchy Oil

Patchy oil measurements were conducted on 2 March 1994. To create controlled patchy areas, three cylinders were made from mylar and placed vertically in the test tank so that all three cylinders were in the antenna beam. The diameter of the cylinders were 7.0 cm, 3.4 cm, and 4.7 cm making enclosed areas of 38.5 cm^2, 9.1 cm^2, and 17.35 cm^2, respectively. Kerosene was the oil type used to create thicknesses from 0 mm to 7 mm in all of the three cylinders against a background of water. The patchy oil covered approximately 50% of the antenna field-of-view.

Figures C-26 to C-34 provide the complete set of measured brightness temperature plots for patchy oil. The 1 mm and 5 mm oil thickness T^B measurements are included in this section for illustrative purposes.

Shown in Figure 4-22 is the measured T^B for 1 mm patchy oil as well as the theoretical predictions. Note that the T^B for patchy oil lies above the predicted water curve, thus making the presence of patchy oil detectable. Figure 4-23 illustrates a 3 mm patchy oil measurement. Again, as shown in Figures C-26 to C-34, the presence of oil has increased the T^B above the water T^B level, and the amplitude of the curve above water T^B is a function of the percentage area of oil in the antenna field-of-view.
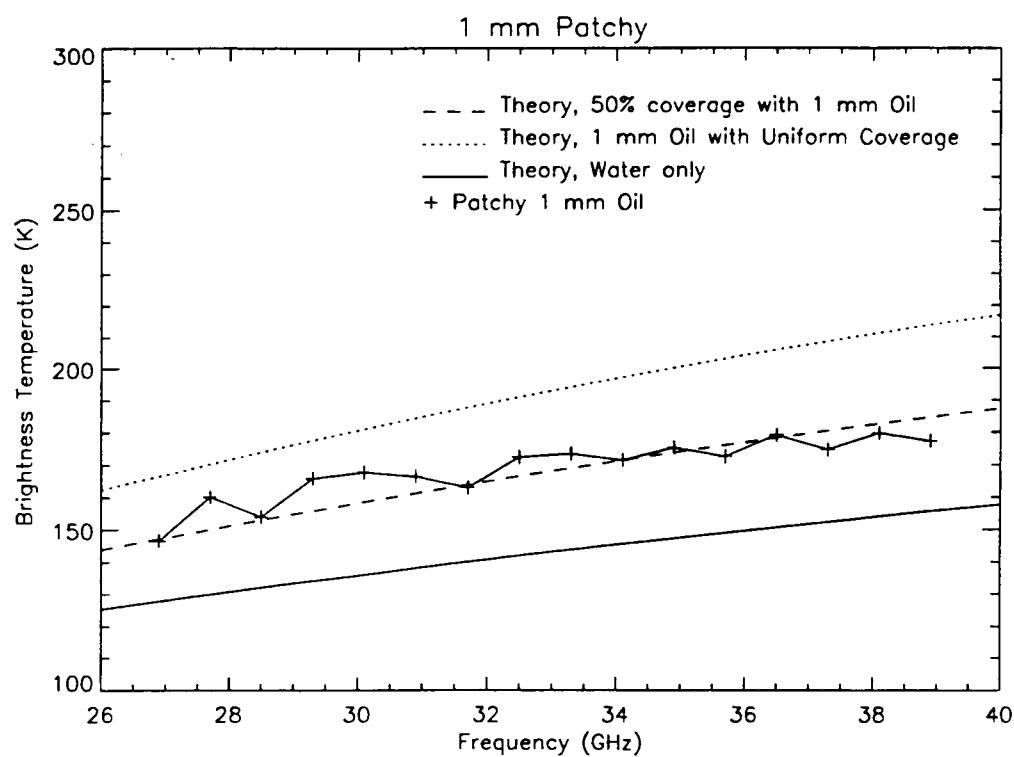
Figure 4-22. Patchy Oil, 1 mm Thickness
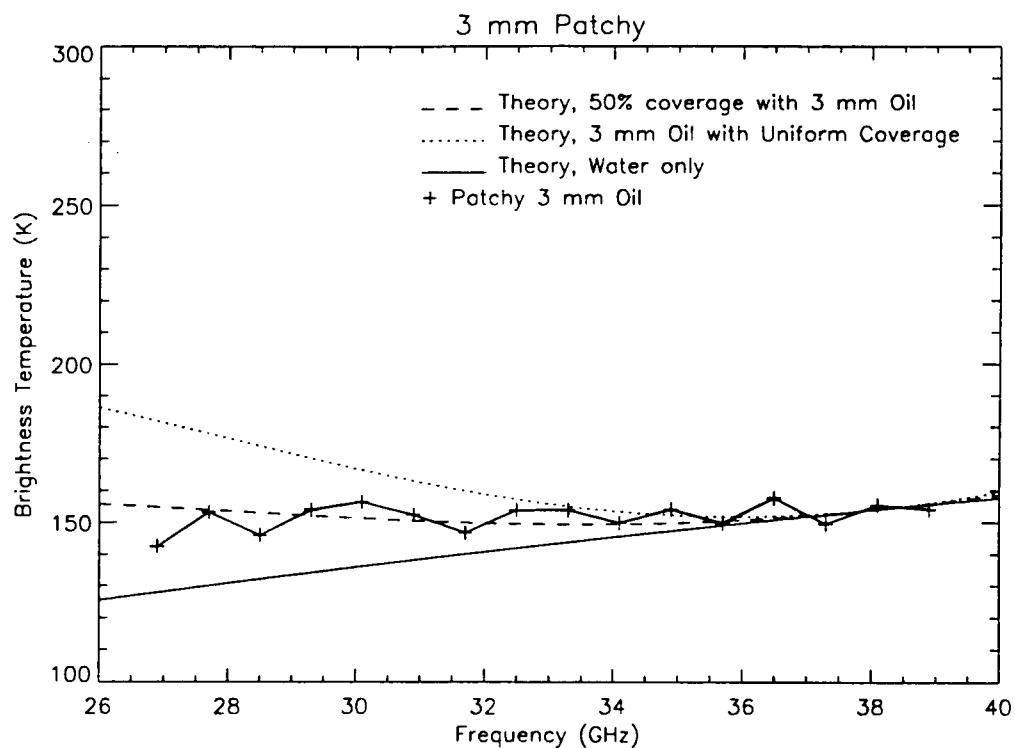
Figure 4-23. Patchy Oil, 3 mm Thickness

4.5 COMPARISONS OF "AVERAGE" THICKNESSES WITHIN THE FIELD OF VIEW

The usefulness of using an FSR to collect oil T^B measurements to discriminate uniform oil layers from non-uniform measurements will be investigated. In this section comparisons using the same average oil thickness within the antenna field of view will be made. Data files collected over the course of the FSR measurement program will be chosen for comparison. The average depths for these comparisons are 0.5 mm, 1.0 mm, 2.0 mm, and 3.0 mm.

To investigate any properties that might make non-uniform oil measurements distinguishable from uniform oil measurements, the daily dependence of the mean T^B shift due to background temperature is removed. This is accomplished by subtracting a measured water T^B for that day from the T^B of the oil thickness measurement.

An average oil thickness (within the antenna field of view) of 0.5 mm is illustrated in Figure 4-24. Table 4-2 lists the type measurement, data and approximate beam fill ratio for the measurements compared in Figure 4-24. The 0.5 mm uniform oil thickness curve has a mean value approximately 10 K above water, and has virtually zero slope. The split tank, step function, and patchy oil curves exhibit a higher mean value than the 0.5 mm uniform thickness, and have a positive slope; these two characteristics indicate the presence of oil in the antenna field of view thicker than the 0.5 mm uniform layer. The positive slope and linear traits of these curves exhibit the same features as a 1.0 mm oil thickness, which in fact was the oil thickness for these non-uniform layers.

Table 4-2. 0.5 mm Average Thickness Comparison

Type	Date	Estimated Beam Fill
Uniform	23 Mar. 1994	100% 0.5 mm
Split	4 Apr. 1994	50% 1 mm, 50% water
Step	2 Mar. 1994	60% 1 mm, 40% 0.5 mm
Patchy	2 Mar. 1994	50% 1 mm, 50% water

An average oil thickness (within the antenna field of view) of 1.0 mm is illustrated in Figure 4-25. Table 4-3 lists the type measurement, data and approximate beam fill ratio for the measurements compared in Figure 4-25. Included in this comparison is a split tank measurement which actually has an average depth of 1.5 mm. The 1.0 mm uniform oil thickness curve has a mean value approximately 30 K above water, and has a positive slope. The split tank and step function oil curves again exhibit higher mean values than the uniform layer with the patchy oil having a similar mean value. The most evident difference in this comparison is that a negative slope is observed for the split tank, step function, and patchy oil measurements. This negative slope is a characteristic of an oil thickness of 2.0 mm, which was the thickness of oil used to create the non-uniform oil/water targets.

Table 4-3. 1.0 mm Average Thickness Comparison

Type	Date	Estimated Beam Fill
Uniform	14 Dec. 1993	100% 1 mm
Split	4 Apr. 1994	50% 1 mm, 50% 2 mm
Step	2 Mar. 1994	60% 2 mm, 40% 0.5 mm
Patchy	2 Mar. 1994	50% 2 mm, 50% water

An average oil thickness (within the antenna field of view) of 2.0 mm is illustrated in Figure 4-26. Table 4-4 lists the type measurement, data and approximate beam fill ratio for the measurements compared in Figure 4-26. The 2.0 mm uniform thickness curve exhibits a negative slope. The step function and patchy oil measurements have a slightly positive slope, and the split tank measurements have a zero slope. The 4 mm T^B vs. frequency curve shape has a characteristic of a low mean above water, with a positive slope; this is observed in the step function and patchy oil measurements. The 3.0 mm T^B vs. frequency curve shape has a slightly negative slope and when averaged with a 1.0 mm T^B vs. frequency curve, the expected slope should be zero to slightly positive. This is observed in the split tank measurement result.
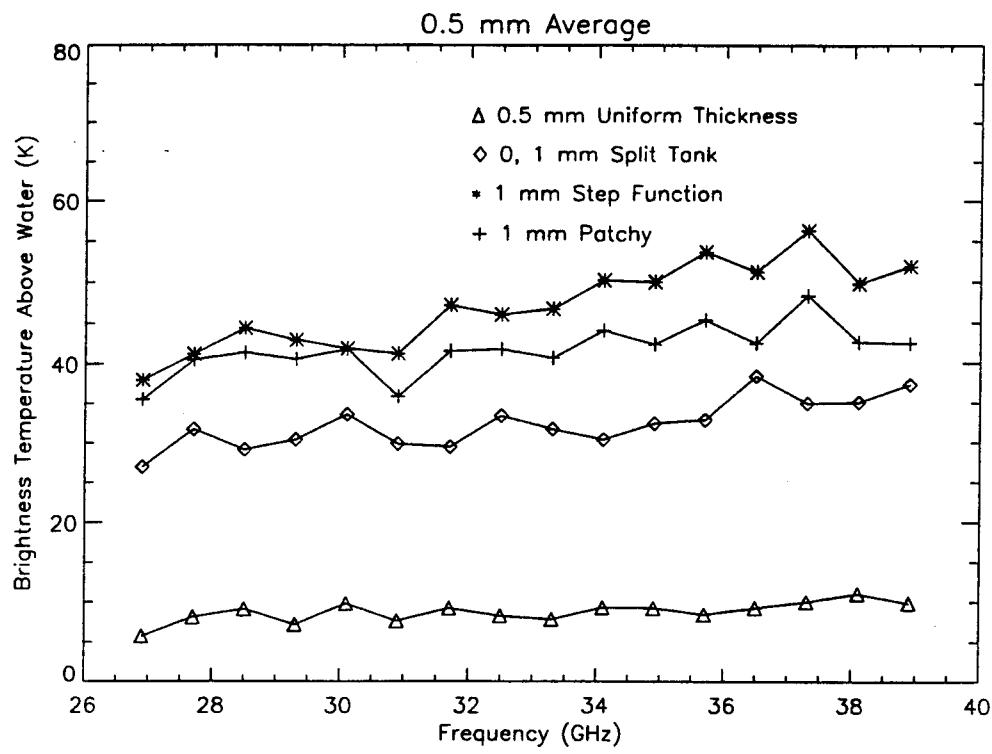
0.5 mm Average

Figure 4-24. Average Oil Depth 0.5 mm
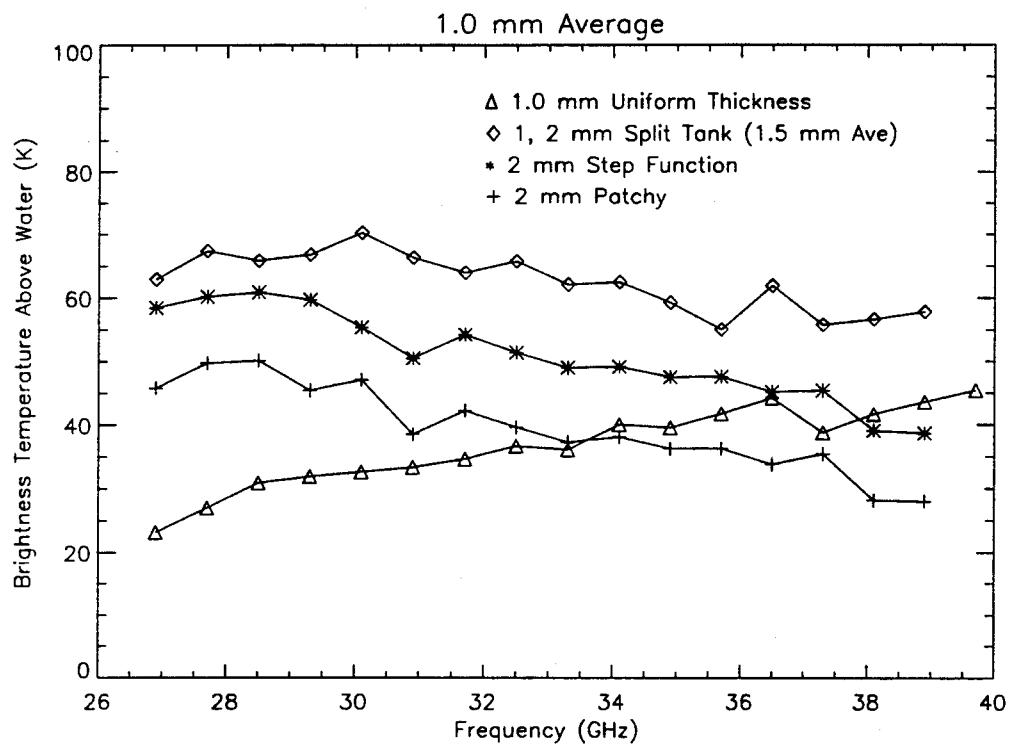
1.0 mm Average

Figure 4-25. Average Oil Depth 1.0 mm

Table 4-4. 2.0 mm Average Thickness Comparison

<u>Type</u>	<u>Date</u>	<u>Estimated Beam Fill</u>
Uniform	14 Dec. 1993	100% 2 mm
Split	4 Apr. 1994	50% 1 mm, 50% 3 mm
Step	2 Mar. 1994	60% 5 mm, 40% 0.5 mm
Patchy	2 Mar. 1994	50% 4 mm, 50% water
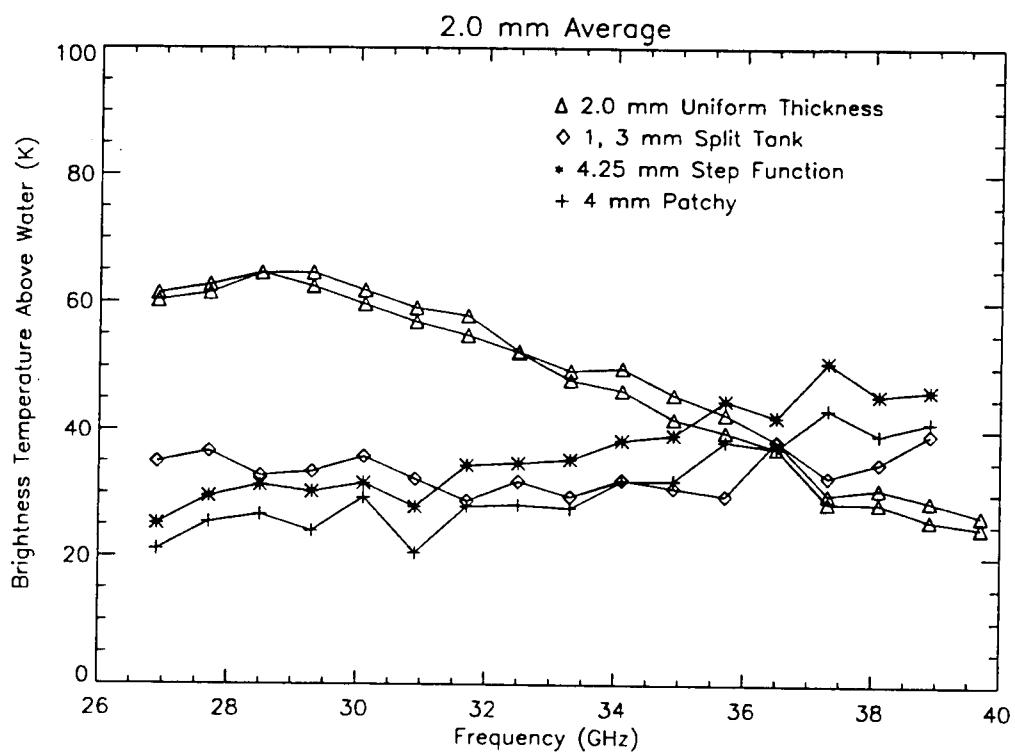
Figure 4-26. Average Oil Depth 2.0 mm

An average oil thickness (within the antenna field of view) of 3.0 mm is illustrated in Figure 4-27. Table 4-5 lists the type measurement, data and approximate beam fill ratio for the measurements compared in Figure 4-27. The 3.0 mm uniform thickness curve exhibits a negative slope, and for the case shown, T^B goes below the water brightness temperature. During the uniform thickness experiments, the FSR was not calibrated as often between measurements, causing the mean T^B to drift which could cause a T^B measurement to go below the water brightness temperature. The split tank, step function, and patchy oil measurements all have very different characteristics. The split tank results show a positive slope, as is expected with the averaging of a 1 mm (positive slope) and 4 mm (positive slope) T^B. The step function result has a characteristic peak near the center of band which is the expected result a 5 mm oil thickness contribution. The patchy oil exhibits a peak near 28 GHz, which is the expected result of a 6 mm oil thickness contribution. Clearly, once the sinusoidal characteristics of T^B variation become measurable, their traits enhance the ability to determine the oil thickness.

Table 4-5. 3.0 mm Average Thickness Comparison

Type	Date	Estimated Beam Fill
Uniform	14 Dec. 1993	100% 3 mm
Split	4 Apr. 1994	50% 1 mm, 50% 4 mm
Step	2 Mar. 1994	60% 5 mm, 40% 0.5 mm
Patchy	2 Mar. 1994	50% 6 mm, 50% water
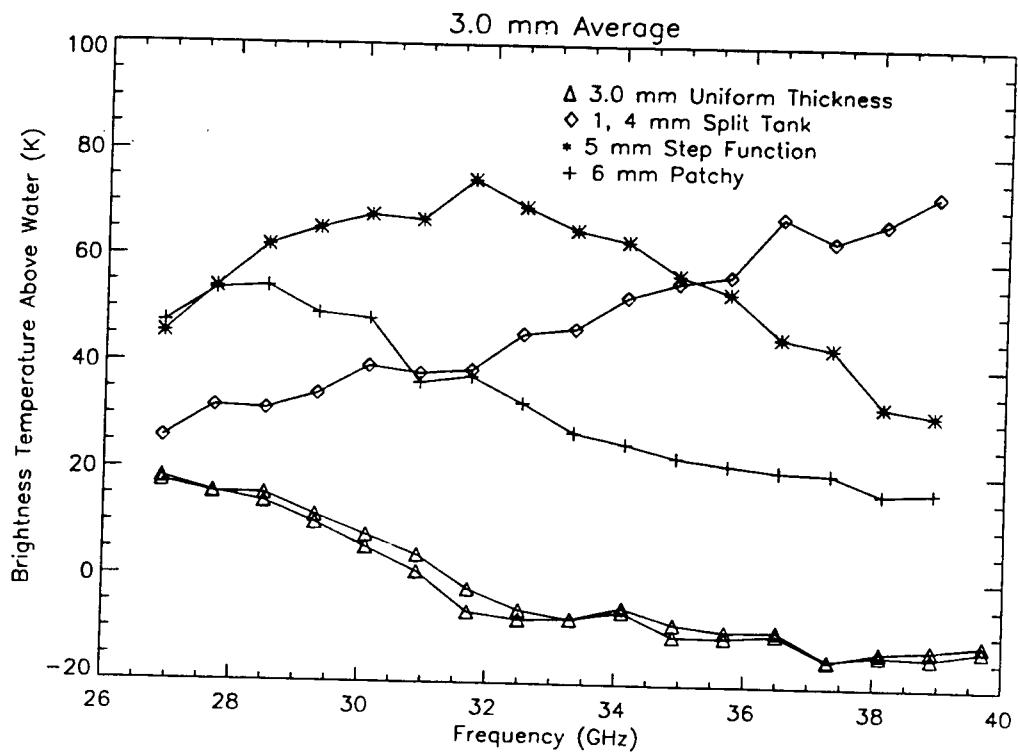
Figure 4-27. Average Oil Depth 3.0 mm

CHAPTER 5 - CONCLUSIONS AND RECOMMENDATIONS

5.1 FREQUENCY SCANNING RADIOMETER HARDWARE

This section summarizes the conclusions presented for the FSR hardware in Chapter 3 and discusses recommended upgrade paths for the FSR instrumentation.

5.1.1 Conclusions

The characterization of the frequency scanning radiometer showed that the instrument operates within the anticipated design parameters. Early proof-of-principle tests and demonstrations (prior to receiver-characterization tests) showed that the characteristic sinusoidal T^B response curve was measured as a function of frequency for uniform oil layers.

Major upgrades to the original FSR equipment included (1) the replacement of a large HP computer with a laptop computer in order to facilitate data file transfer and file storage capability, and (2) the addition of an active heat sink to the receiver electronics to minimize thermal drift effects of the bipolar transistor amplifiers. The first of these upgrades was planned in the statement of work. The second upgrade was not anticipated but was needed to ensure system stability over the measurement period.

The reliability of the FSR hardware has generally been good. The FSR has operated successfully outdoors under all types of ambient conditions from rain, drizzle, and snow to sunny warm weather. The equipment has been mounted on a laboratory cart, and wheeled from the laboratory to the rooftop with no special shock mounting or protection from the elements. Only two equipment malfunctions have occurred in over one year, and the cause of the failure was evident. During receiver characterization, the Ka-band mixer degraded causing a rise in the receiver noise temperature and the conversion loss. A backup mixer was installed and the faulty Ka-band mixer was repaired at minimal cost. A second equipment failure occurred during oil-thickness phenomenology

measurements. The Ka-band output module in the sweep oscillator failed.
Fortunately, this module was still under warranty and was repaired at no cost.

5.1.2 Recommendations

During the receiver characterization tests, areas that needed additional
improvements were identified. Low cost and easy (minimum effort)
improvements were made to the FSR so that a consistent measurement set
could be obtained. The improvements were also done in a manner that would
yield a field-capable unit.

It is our recommendation that the FSR continue to be hardened for use as a
measurement instrument in the field. Over the short term, the following items
have been identified as hardware that can improve the measurement capabilities
of the FSR.

1. Replace the existing pyramidal feed horn with a scalar feed horn. This will
reduce antenna sidelobe effects. The scalar feed horn would be an off-the-shelf
product.

2. Add a second antenna to monitor sky brightness temperature. This will
eliminate anomalous measurements caused by short-term variations in T_{sky}.

3. Modify the receiver to provide internal Dicke switching to measure V_{HOT} at
each measurement frequency. This will eliminate anomalous measurements
caused by variations in the system electronic gain. The Dicke switch would be
computer controlled and would switch the input of the Ka-band mixer between
the antenna and a terminated load.

4. Mount the sweep oscillator unit in a portable (19-inch rack mount), shock
mounted, waterproof enclosure for future field use. Continue to field harden the
FSR receiver electronics package by mounting it in a waterproof enclosure.

As a long term recommendation, the utility of a multiple channel upgrade should
be considered. As the system matures from a field unit to an airborne unit, the

dwell time per sample frequency becomes an issue; with the existing system sampling over 16 frequencies, each measurement sweep takes approximately 11 seconds. The existing FSR architecture would require a stop-and-sample flight profile for an airborne system. By adding a frequency de-multiplexer after the existing Ka-band mixer, the received signal would be split into at least 8 (parallel) receiver channels. This would enable the FSR to collect a complete sweep within a single receiver dwell time (tenths of a second). Thus the system could collect data over a small, contained footprint while the airborne platform remains in motion. The frequency de-multiplexer needed to accomplish this modification is commercially available. The existing sweep oscillator would be replaced by a fixed-frequency local oscillator in the multichannel unit, and the existing single channel receiver electronics would become one channel. Along with the frequency de-multiplexer, only additional receiver electronics would have to be purchased. Upon successful testing of the single channel FSR as a field deployable unit, the design and incorporation of parts from the single channel FSR into the multichannel unit for tests using an airborne platform should be considered.

To develop a commercially available instrument, the FSR technology should be transitioned to industry. This transition can take place at one of two stages: (1) prior to the start of multichannel FSR design and modification, enter into a Cooperative Research and Development Agreement (CRADA) with an interested commercial vendor or (2) after Lincoln Laboratory has completed a proof-of-principle demonstration of the mulitchannel FSR, hand off the technology that was developed under this program. In both cases, Lincoln Laboratory should serve in a technical guidance role to supervise the development of the commercial unit and act as an independent source to verify test results.

5.1.3 Dual Band Radiometer

The theoretical curves for the 26 - 40 GHz FSR predict that at oil thicknesses near 3.5 mm a null will extend over nearly all the band. The expected oil T^B will not vary much above water, which will make detecting the presence of oil at this thickness difficult. One solution to this problem is to provide a single frequency radiometric measurement in the 75 - 100 GHz band, possibly near 94 GHz where a T^B maximum is expected for 3.5 mm oil. This additional single point could also

aid in the detection of thin oil layers, potentially down to a minimum thickness of 0.05 mm.

The development of a single frequency radiometer at this higher frequency band opens the possibility of developing a dual band FSR. The technology now exists for using off-the-shelf parts to build a 75 - 100 GHz FSR. A 75 - 100 GHz FSR operating in parallel with the 26 - 40 GHz FSR could unambiguously use Fourier techniques to measure oil thicknesses down to 0.5 mm. Using curve fitting techniques similar to those described for continued algorithm development, thinner layers could be measured. An effort to design, build, and test this dual-band FSR should be considered.

5.2 FREQUENCY SCANNING RADIOMETRY MEASUREMENTS

This section summarizes the conclusions presented for the FSR measurements described in Chapter 4 and outlines a recommended field demonstration and measurement program.

5.2.1 Conclusions

Results of FSR measurements under various atmospheric conditions, namely day and night, clear, overcast, drizzle, and snow have been obtained. All of the measurements show results for uniform layers that are consistent with theoretical predictions. Through measurements of crude oil, motor oil, and kerosene, it has been demonstrated that the results are independent of oil type. Thus, a laboratory version FSR can be operated to successfully measure uniform oil thicknesses.

Measurements of non-uniform oil thicknesses were conducted in an attempt to model expected real-world scenarios. Patchy oil measurements were meant to model the presence of tarballs while step-function and gradient measurements modeled the effect of windrows. For each of the scenarios investigated, the characteristic change of T^B versus frequency due to the oil layer was a function of antenna fill factor; the percentage of the layer filling the antenna field of view. These measurements were compared against uniform oil measurements that have the same "average" oil thickness in the antenna field of view. For the same

average thickness, characteristics of the thicker non-uniform oil layer were evident in the resulting curves.

The 20%-water emulsion measurements seem to follow the shape of theoretical predictions for uniform (pure) oil layers, although the measured mean T^B is much higher. Although not an unexpected result, the 40%-water emulsion and saturated emulsions also have a high mean T^B than the uniform oil predictions, and the measurements do not follow the shape of the uniform oil layer curves. The fact that the mean T^B for emulsions is much different from water and uniform oil indicates that the emulsion is distinguishable from both water and oil.

5.2.2 Recommendations

All of the measurements conducted under this project have been done under controlled laboratory conditions. The next phase of the project should be to measure oil thicknesses at an outdoor facility capable of creating more realistic scenarios.

Outlined briefly, the steps to follow for this test program should address the following issues:

1. The FSR receiver electronics package must be modified to be compatible with the mounting requirements at the selected test facility.

2. After final equipment field hardening modifications are complete, but prior to departure to the test facility, the equipment must demonstrate the capability to measure uniform, patchy, step function, and emulsified oil with an antenna to liquid surface spacing of several meters. It is assumed that this antenna-to-liquid surface distance is sufficient to keep the FSR antenna dry from splashes during actual on-site tests.

3. Once the equipment has arrived on-site, the demonstrated capabilities should be repeated using the laboratory test tank. This will verify that (1) the FSR operating parameters were unchanged during shipment, and (2) electromagnetic interference at the site is minimal.

4. Multiple-look (3 to 5 independent samples) measurements will be made of various types of oil in the test tank beginning with uniform oil layers under calibration, smooth, and rough water conditions. On-site assessment of the data should be made and water roughness should be increased until either the maximum wave generating capability is reached or until measurements become anomalous. Oil type and thickness (or volume spread over a known area), ambient weather, and wave conditions will be recorded.

5. Measurements similar to item (4) above should be made on emulsified oil under calibration, smooth, and rough water conditions using various percentage mixtures of oil and water.

The present method of determining oil thickness is to visually compare the measured data against a theoretical prediction curve. Although a trained operator can identify the presence of oil and estimate its thickness based on curve characteristics, an airborne FSR will need automatic thickness measurement capabilities in order to create an oil depth map. Algorithms need to be developed and tested for automatic thickness measurement. These algorithms must first detect the presence of oil, then in an attempt to determine oil volume, classify the oil based on thickness or type (pure oil or emulsion) and antenna beam fill. The presence of oil in the antenna field of view is evident from the rise in T^B above water, and the shape of the measured data curve. For thin layers (less than 0.5 mm), the slope of the curve is similar to water, so the small change in T^B is the only thickness discriminant. For layers between 0.5 mm and 4.5. mm the rise in T^B plus a linear slope characteristic is the thickness discriminant, and for layers above 4.5 mm the shape of the sinusoidal variation is a powerful discriminant.

In addition to the field test program, theoretical work should continue in the area of developing a model for predicting T^B for both uniform and emulsified oil.

REFERENCES

1. Hollinger, James P., "The Determination of Oil Slick Thickness by Means of Multifrequency Passive Microwave Techniques", Dept. of Transportation, No CG-D-31-75, U.S.C.G., ORD, Washington, D.C., 1974.

2. Lodge, A.E., ed., <u>The Remote Sensing of Oil Slicks</u>, pp. 18-19, 35, 70, 85, John Wiley and Sons, 1989.

3. Vissen, H., "Teledetection of the Thickness of Oil Films on Polluted Water Based on the Oil Fluorescence Properties", App. Optics, 18, p. 1749, 1979.

4. Reuter, R., "Lidar Investigates Natural and Oil Polluted Sea Water", Lambda Highlights, Lambda Physik GmbH, 1989.

5. Hoge, F.E. and Swift, R.N., "Oil Film Thickness Measurement Using Airborne Laser-Based Water Raman Backscatter", Applied Optics, Vol. 19, pp. 3269-3281, 1980.

6. Horvath, R., Morgan, W.L., and Stewart, S.R., Optical Remote Sensing of Oil Slicks: Signature Analysis and Systems Evaluation, U.S. Coast Guard Report No. 1156, Willow Run Laboratories, Univ. of Michigan, October 1971.

7. Skou, N. "Microwave Radiometry for Oil Pollution Monitoring , Measurements and Systems", IEEE Trans. Geoscience and Remote Sensing, GE-24, No. 3, pp. 360—367, May 1989.

8. Gruner, K. et al., "Contributions to Oil Spill Detection and Analysis with Radar and Microwave Radiometry, Results of the Archimedes II Campaign", Proceedings of IGARSS '86 Symposium, pp. 1375-1380, Zurich, Sept.1986

9. Croswell, W. et al., "Ocean Experiments and Remotely Sensed Images of Chemically Dispersed Oil Spills", IEEE Trans. on Geoscience and Remote Sensing, GE-21, No. 1, pp. 2-15, January 1983.

10. Skou, N., Communication to D. Staelin, MIT, "Example of Airborne Scanner: The TUD System and its Application for Oil Pollution Monitoring", excerpt from Technical University of Denmark report, 1989.

11. Kong, J., Electromagnetic Wave Theory, Chapter 3, John Wiley & Sons, Inc. 1986.

12. Apel, J, Principles of Ocean Physics, Chapter 7, Academic Press, 1987.

13. Ulaby, F.T., Moore, R.K., and Fung, A.K., Microwave Remote Sensing: Active and Passive, Vol. III, pp. 2020-2025, Artech House, 1986.

14. Laaperi, A., "Experimental Results From Oil Thickness Measurements with the Microprocessor Controlled Microwave Radiometer", IGARSS '83, pp. 6.1- 6.5, 1983.

APPENDIX A
UNIFORM LAYER MEASUREMENTS

The complete set of measured data comparisons undertaken to verify the Chapter 4 uniform oil thickness test results is included as this appendix. For each plot, the legend describes the attributes that are compared, and a theoretical prediction of a nominal brightness temperature is included.

Figures A-1 to A-8 illustrate the oil type comparisons for crude oil, pump oil, and kerosene. Uniform thickness measurements of oil that are available for comparison purposes are oil depths of 0 mm, 3 mm, 4 mm, 5 mm, 6 mm, 7 mm, 8 mm, and 9 mm.

Figures A-9 to A-23 illustrate diurnal comparisons of oil. Uniform thickness measurements of oil that are available for comparison purposes are 0 mm, 3 mm, 4 mm, 5 mm, 6 mm, 7 mm, 8 mm, and 9 mm. Because of a volumetric measurement error during the day of 14 Dec. 1993, the T^B curves have a different frequency of variation characteristic for depths greater than 5 mm. Using the theoretical model, it is estimated that the oil depth was 0.5 mm deeper than expected. Plots to verify this, Figures A-19 to A-23, show data consistent with oil layer thicknesses of 5.5 mm, 6.5 mm, 7.5 mm, 8.5 mm, and 9.5 mm.

Figures A-24 to A-29 illustrate T^B measurements collected under variants of weather conditions. Uniform thickness measurements that are available for comparison purposes are oil depths of 4 mm, 5 mm, 6 mm, 7 mm, 8 mm, and 9 mm.
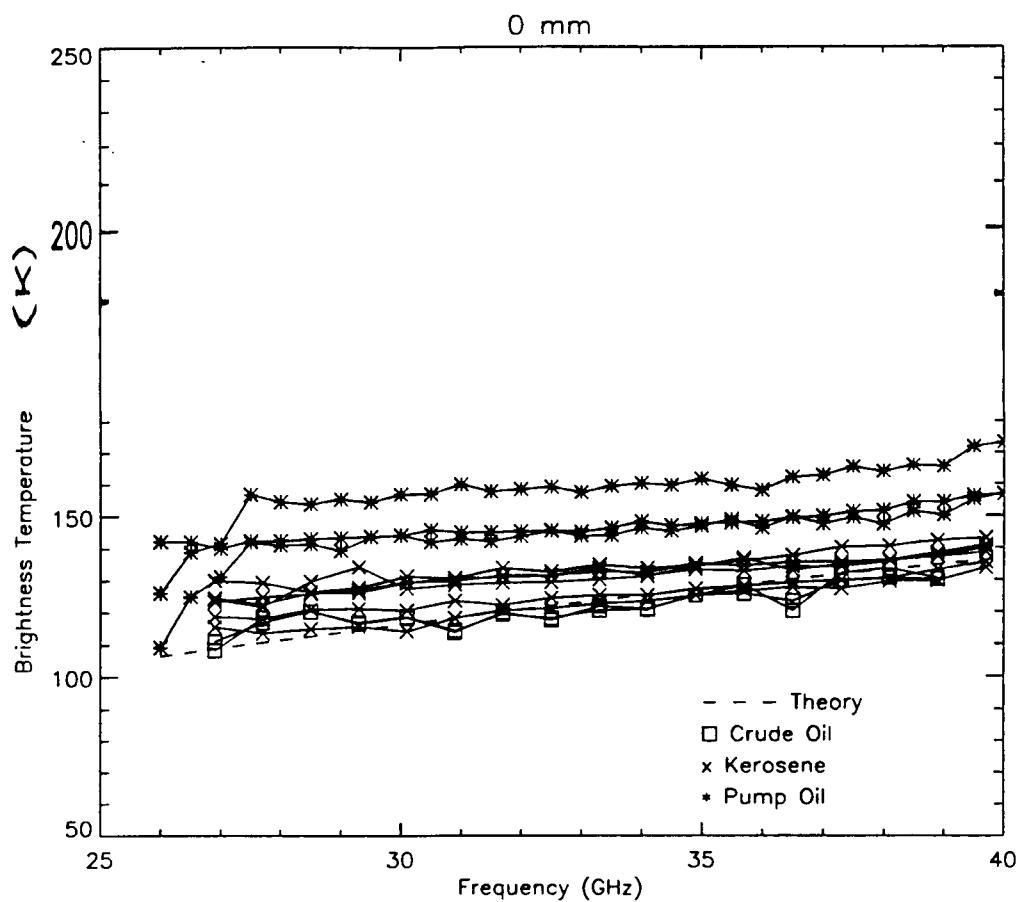
Figure A-1. Oil Type Comparison, Water
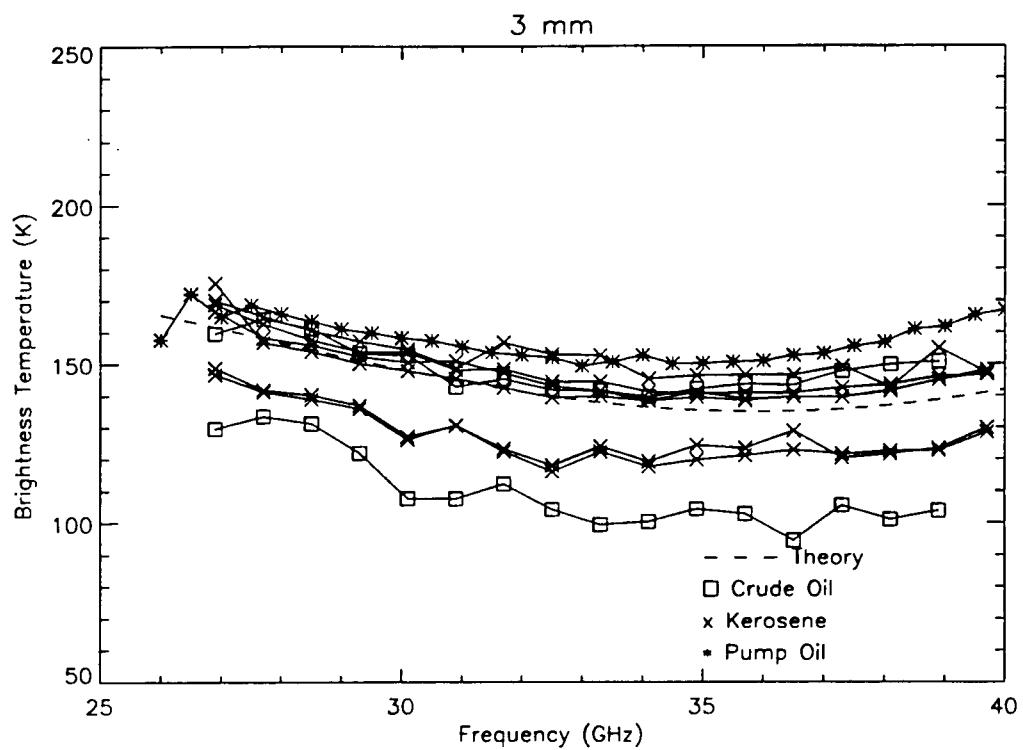
Figure A-2. Oil Type Comparison, 3 mm Uniform Thickness
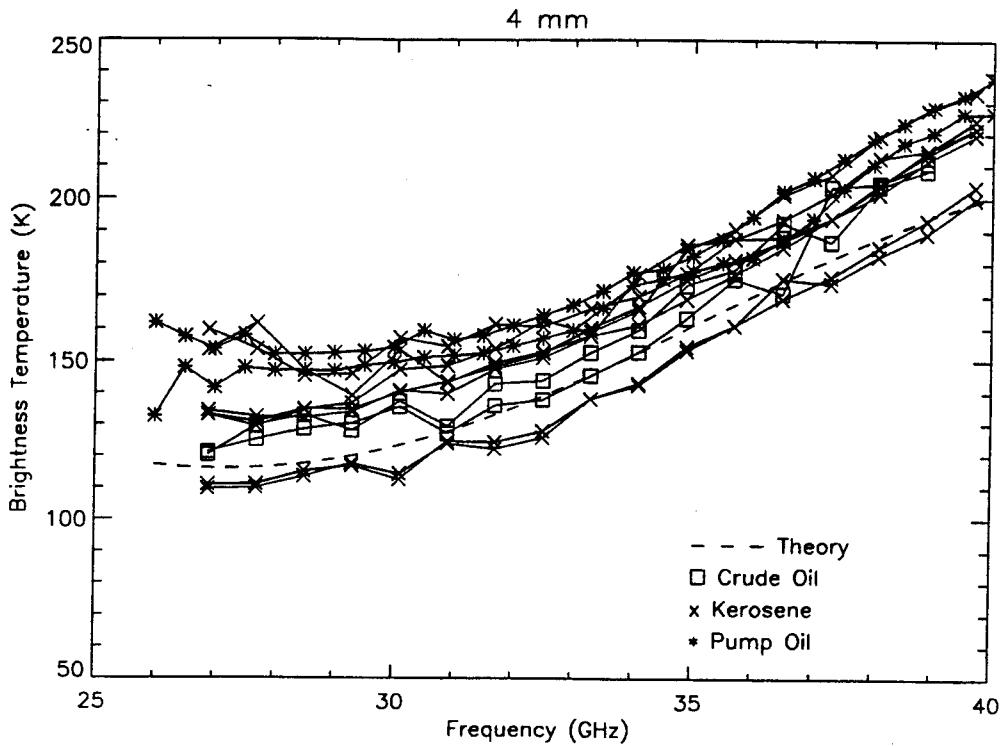
Figure A-3. Oil Type Comparison, 4 mm Uniform Thickness
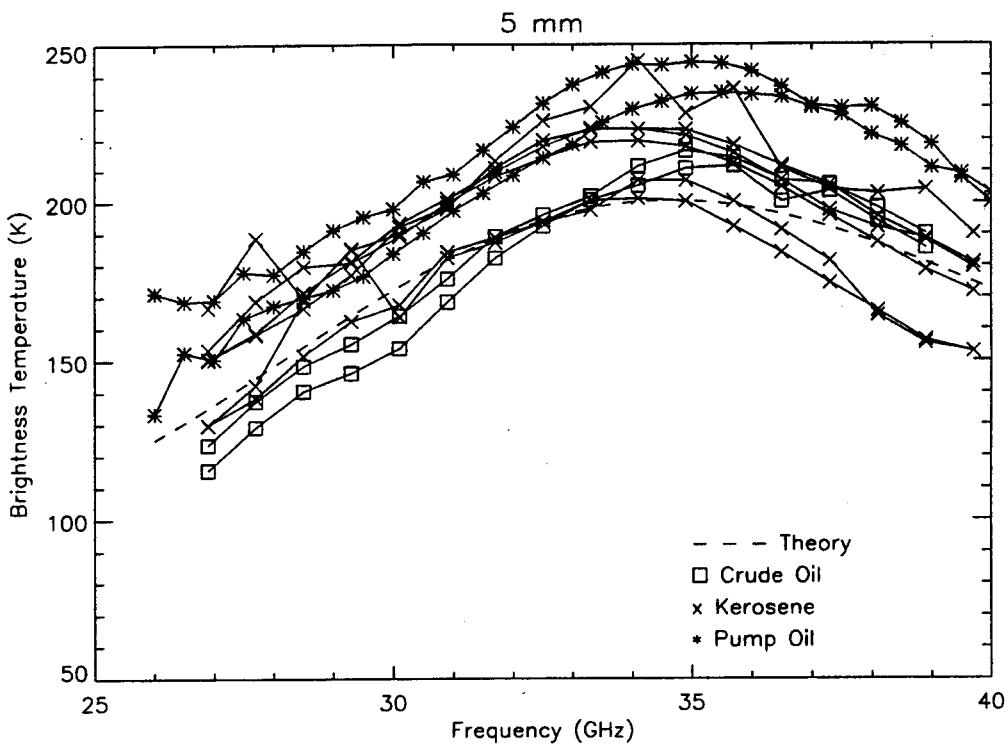
Figure A-4. Oil Type Comparison, 5 mm Uniform Thickness
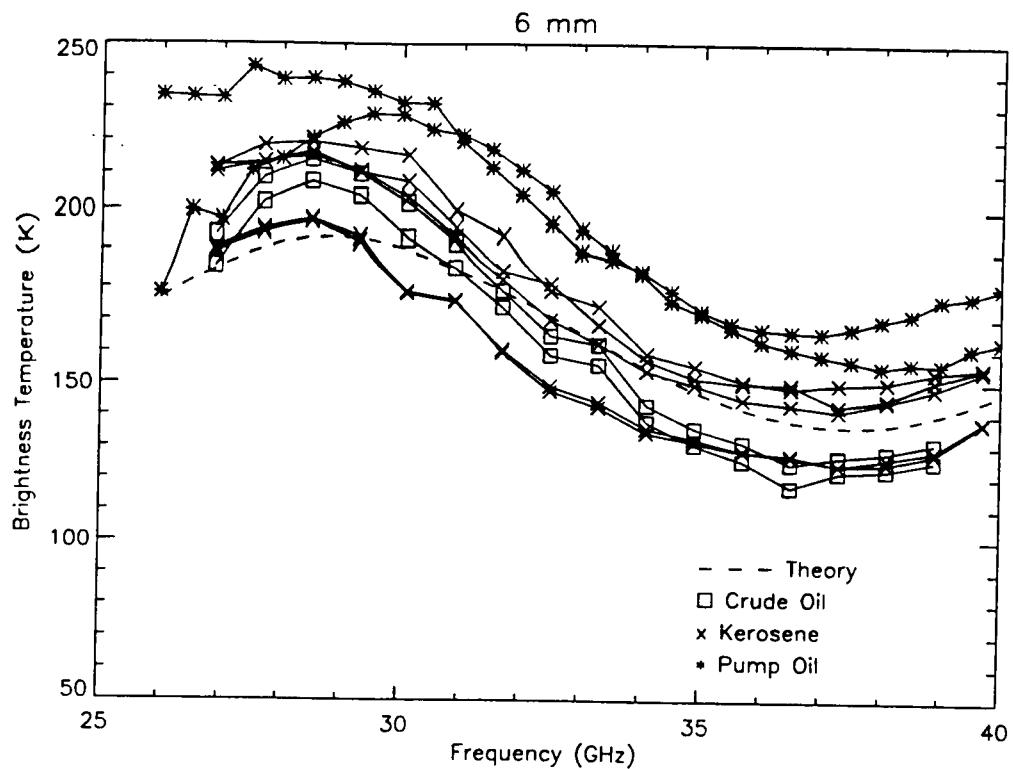
Figure A-5. Oil Type Comparison, 6 mm Uniform Thickness
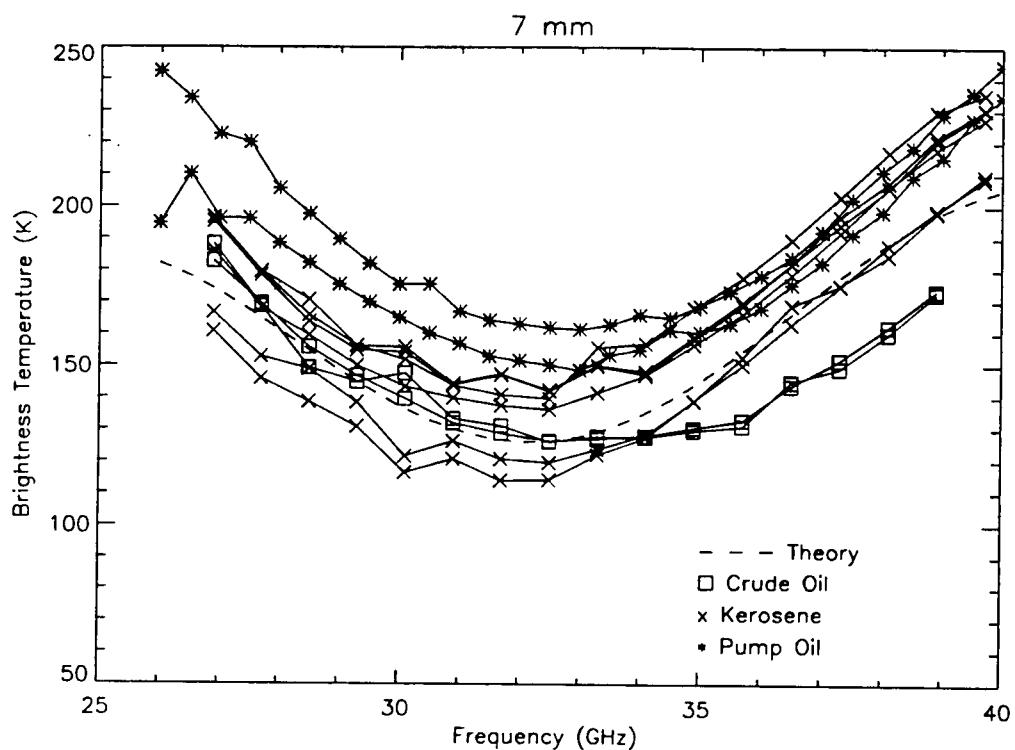
Figure A-6. Oil Type Comparison, 7 mm Uniform Thickness

A-4
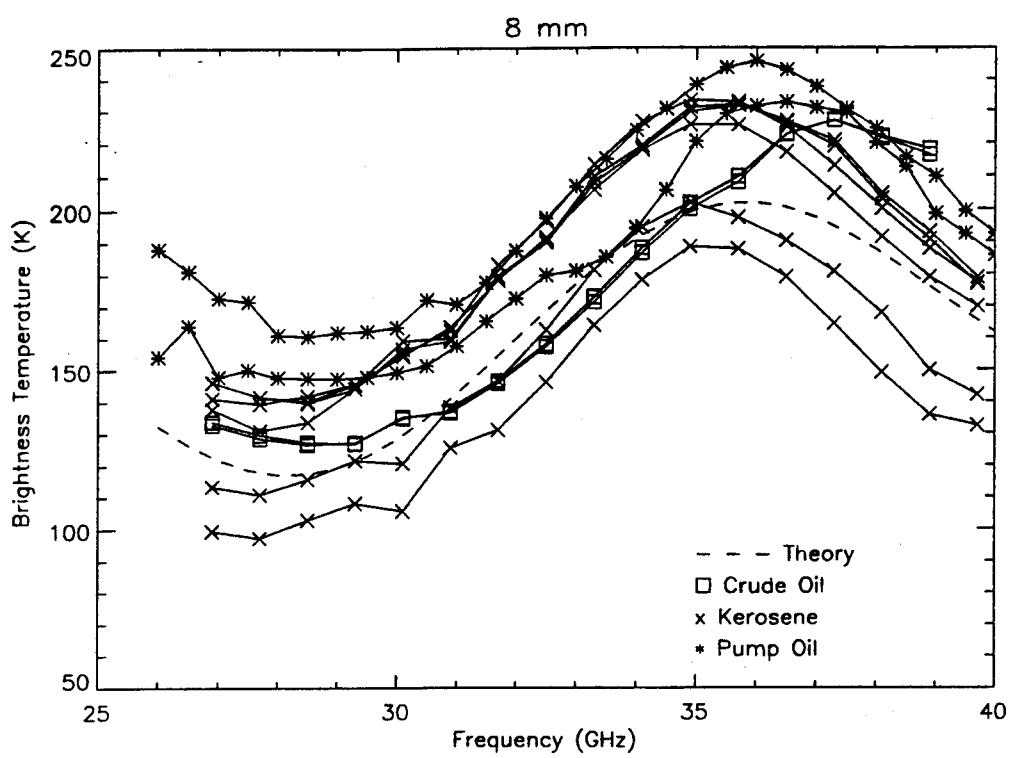
Figure A-7. Oil Type Comparison, 8 mm Uniform Thickness
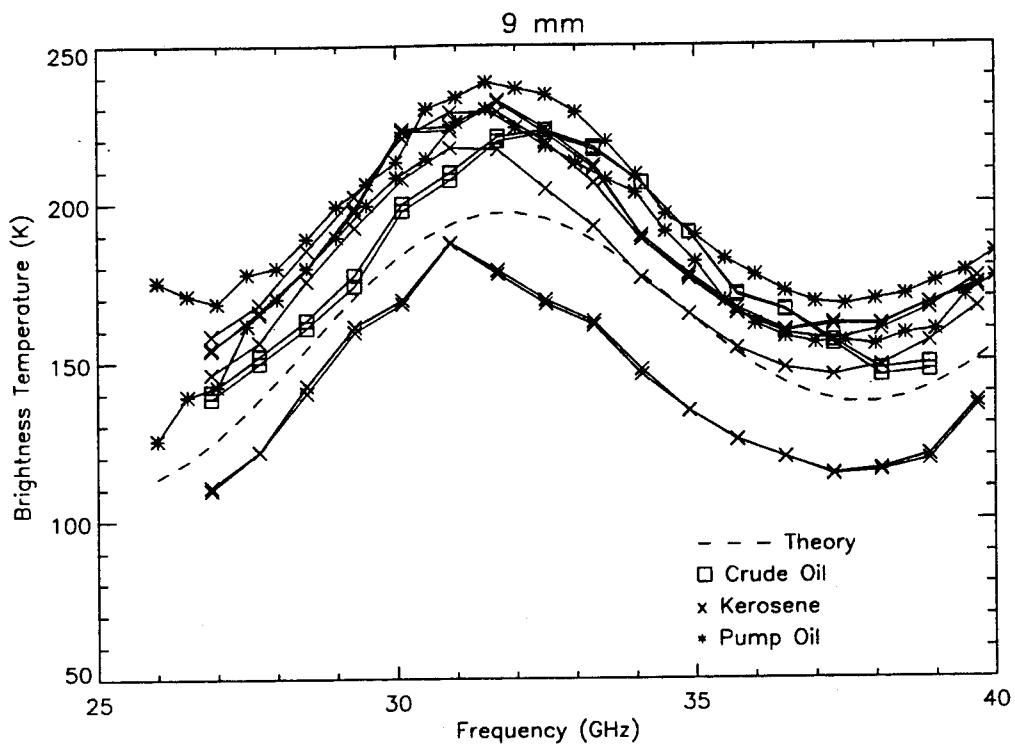
Figure A-8. Oil Type Comparison, 9 mm Uniform Thickness
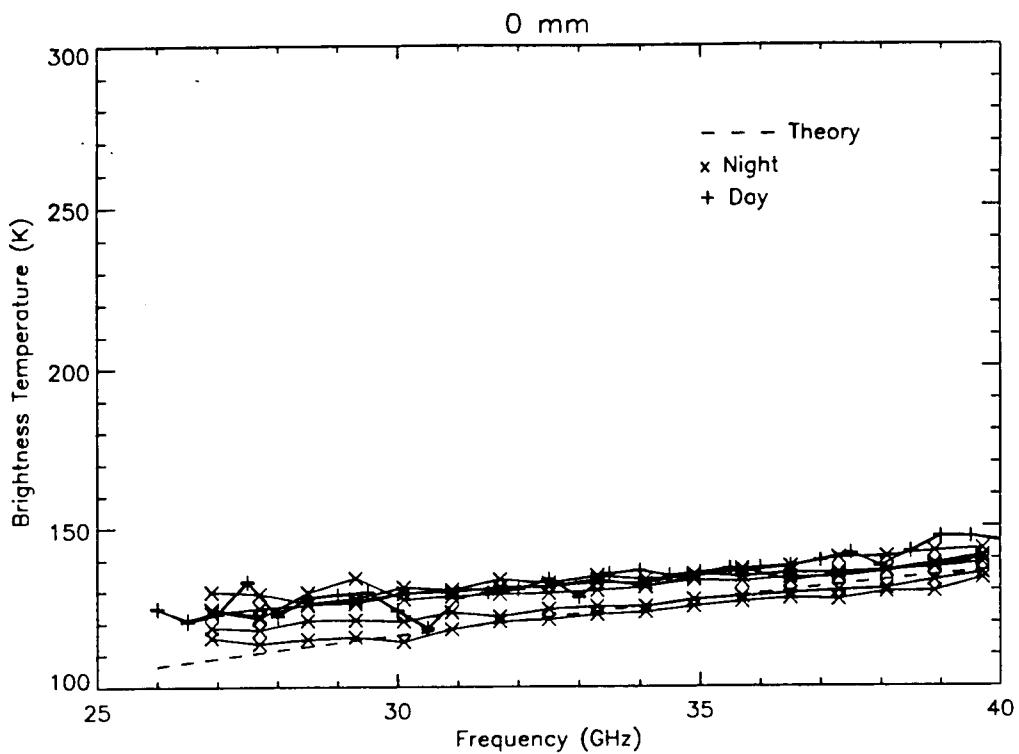
Figure A-9. Diurnal Comparison, Water
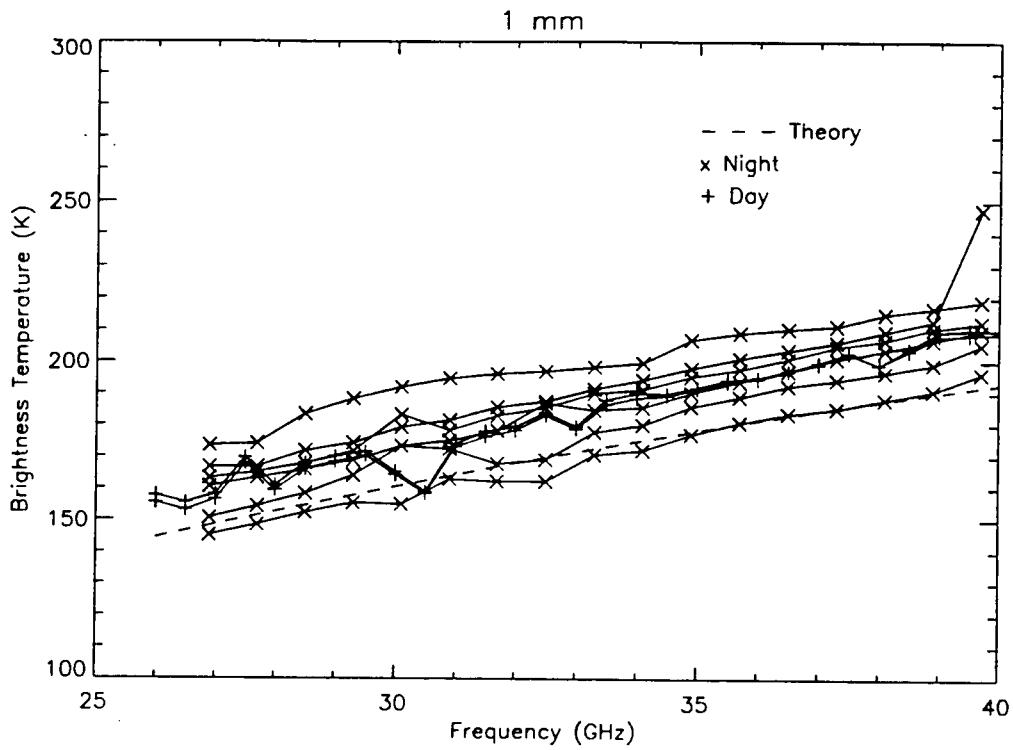
Figure A-10. Diurnal Comparison, 1 mm Uniform Thickness

2 mm
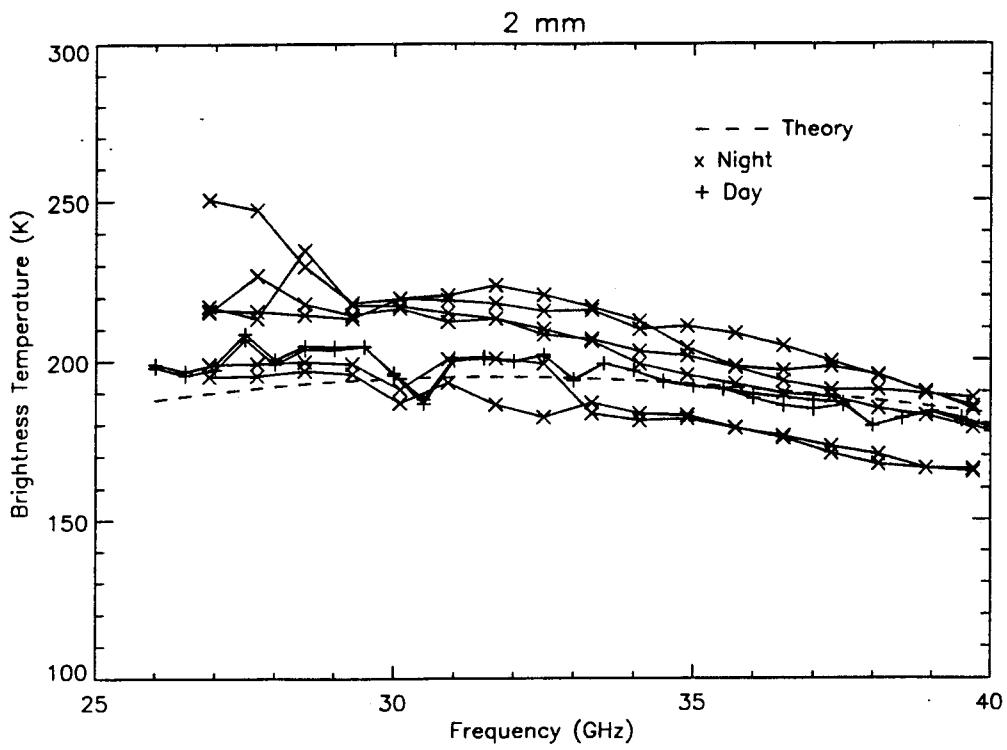
Figure A-11. Diurnal Comparison, 2 mm Uniform Thickness

3 mm
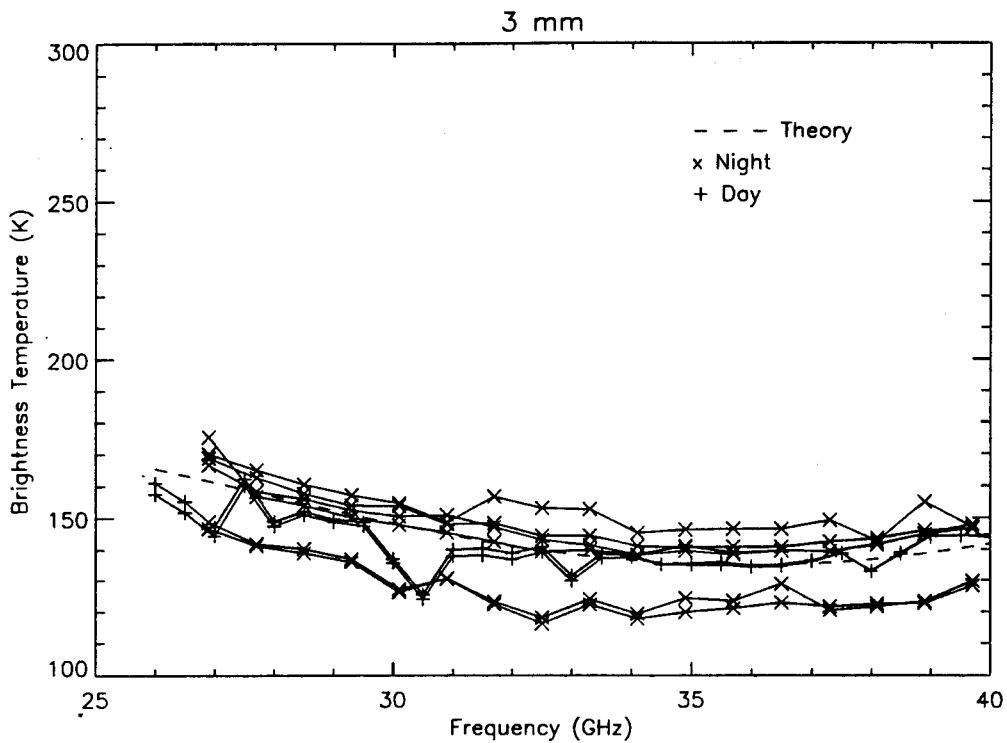
Figure A-12. Diurnal Comparison, 3 mm Uniform Thickness
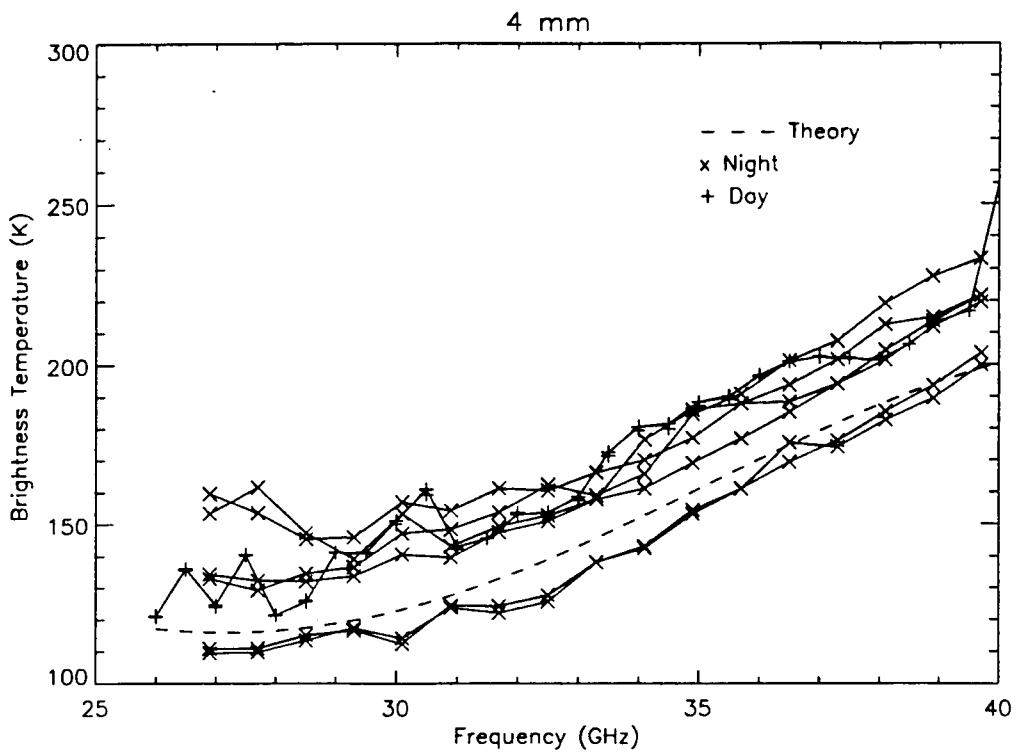
Figure A-13. Diurnal Comparison, 4 mm Uniform Thickness
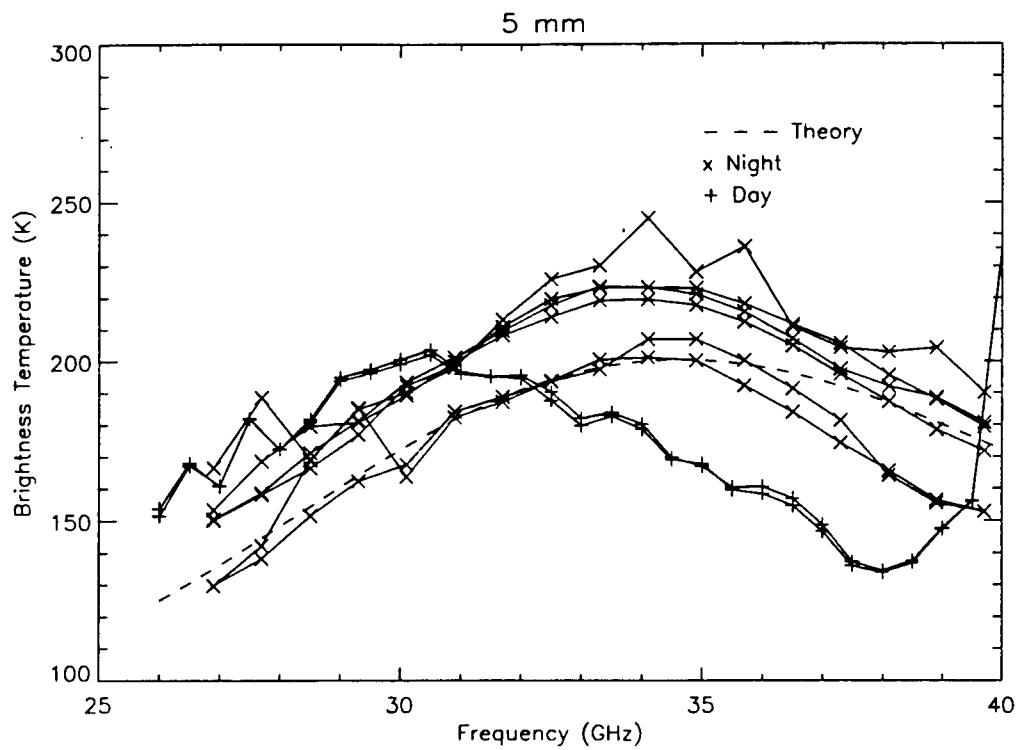
Figure A-14. Diurnal Comparison, 5 mm Uniform Thickness
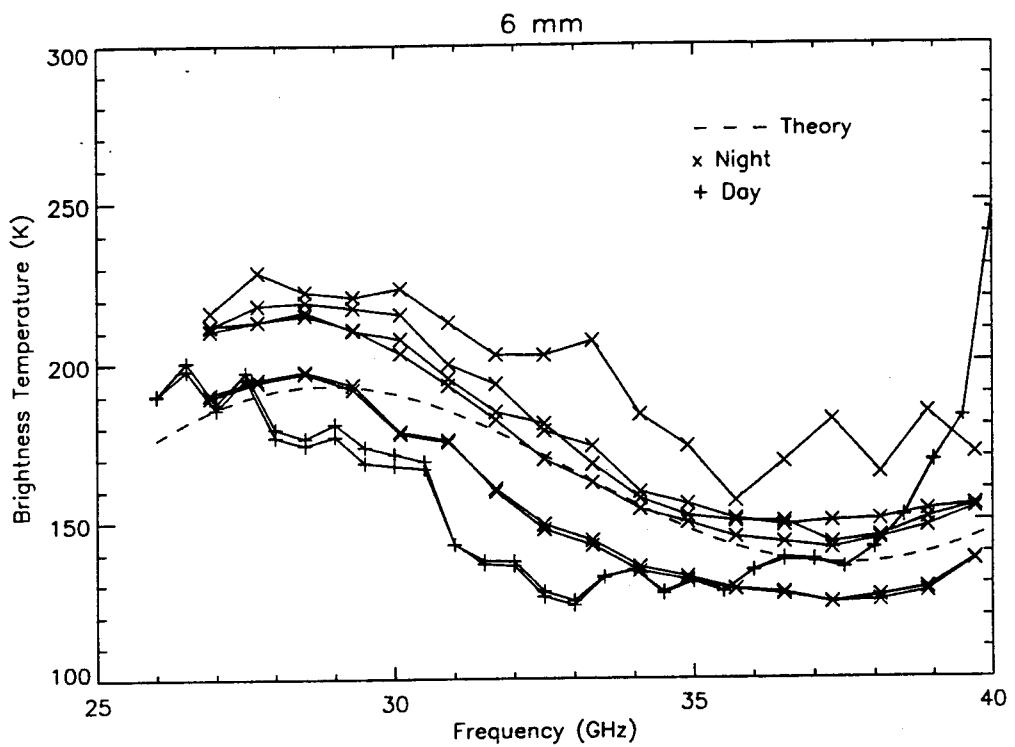
Figure A-15. Diurnal Comparison, 6 mm Uniform Thickness
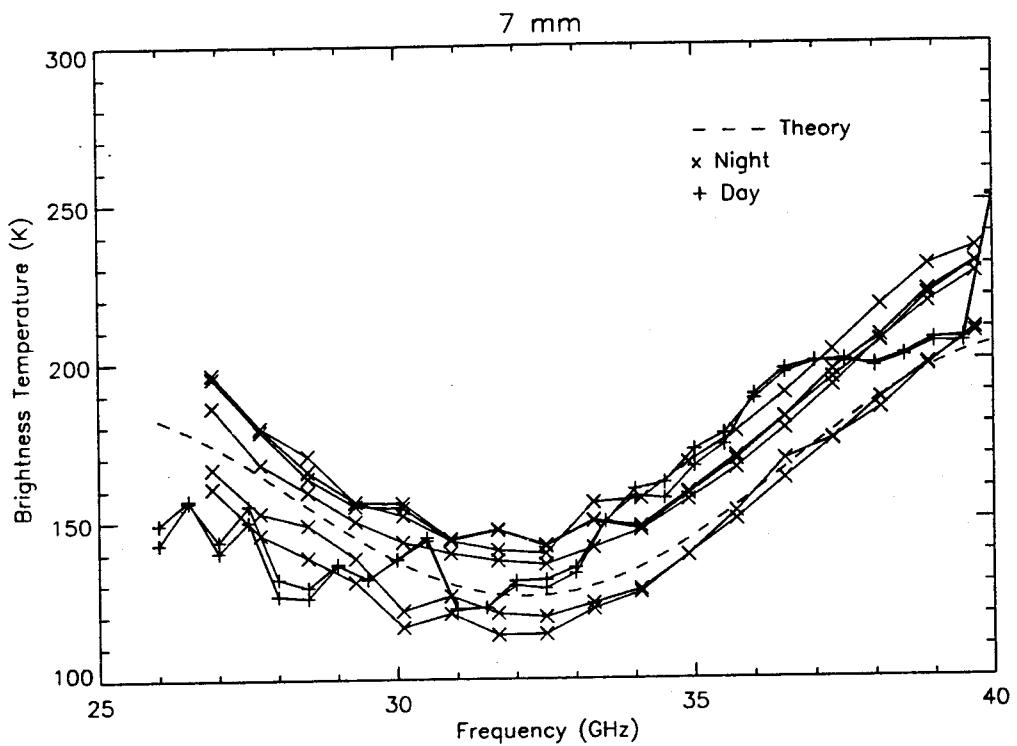
Figure A-16. Diurnal Comparison, 7 mm Uniform Thickness
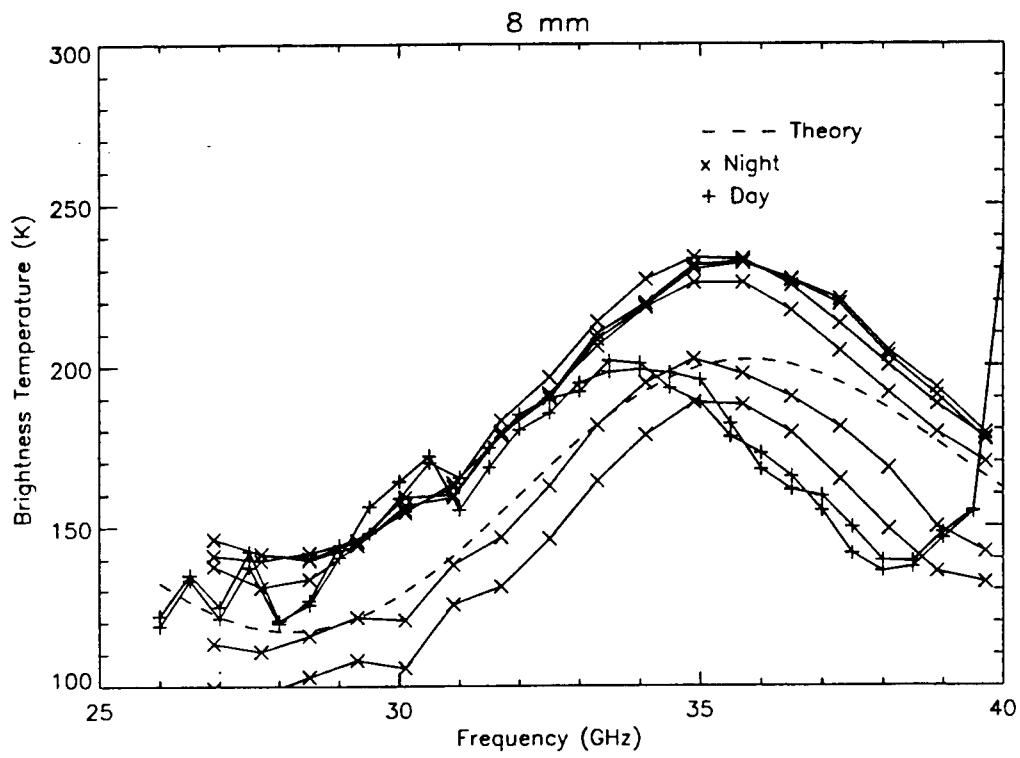
Figure A-17. Diurnal Comparison, 8 mm Uniform Thickness
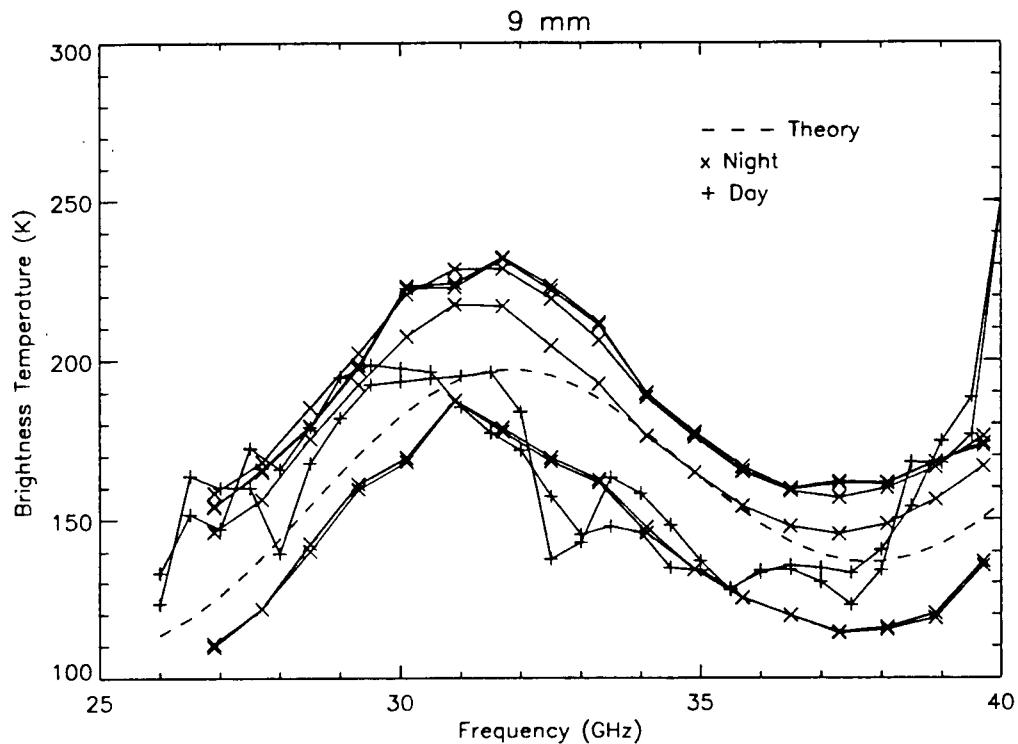
Figure A-18. Diurnal Comparison, 9 mm Uniform Thickness

A-10
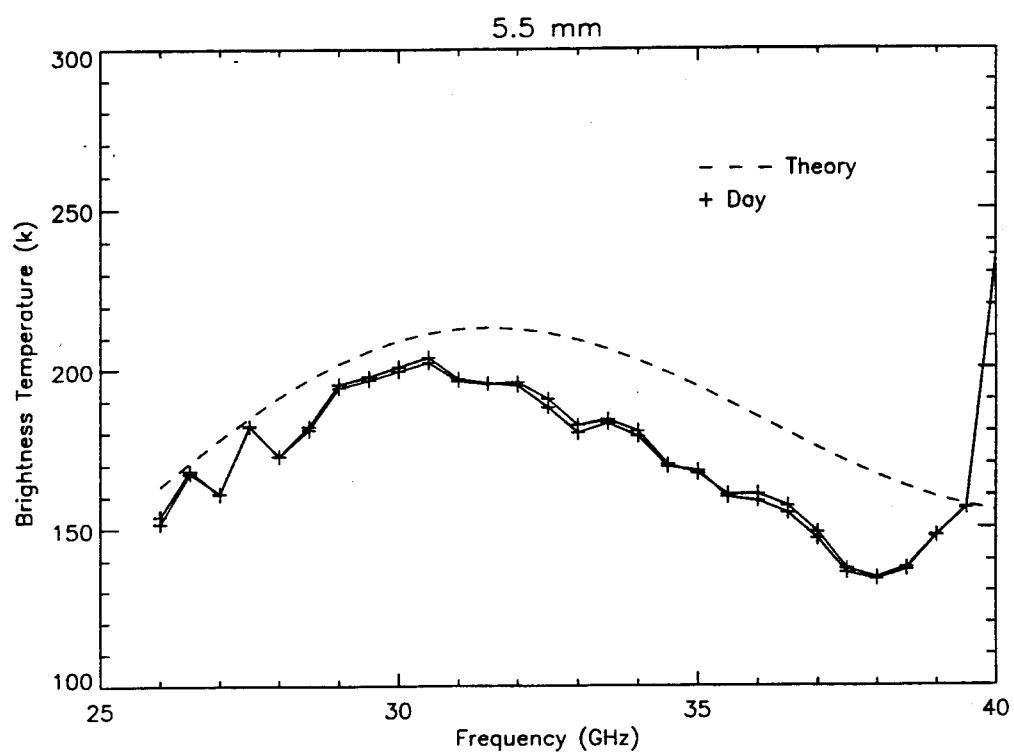
5.5 mm

Figure A-19. Diurnal Comparison, 5.5 mm Estimated Thickness
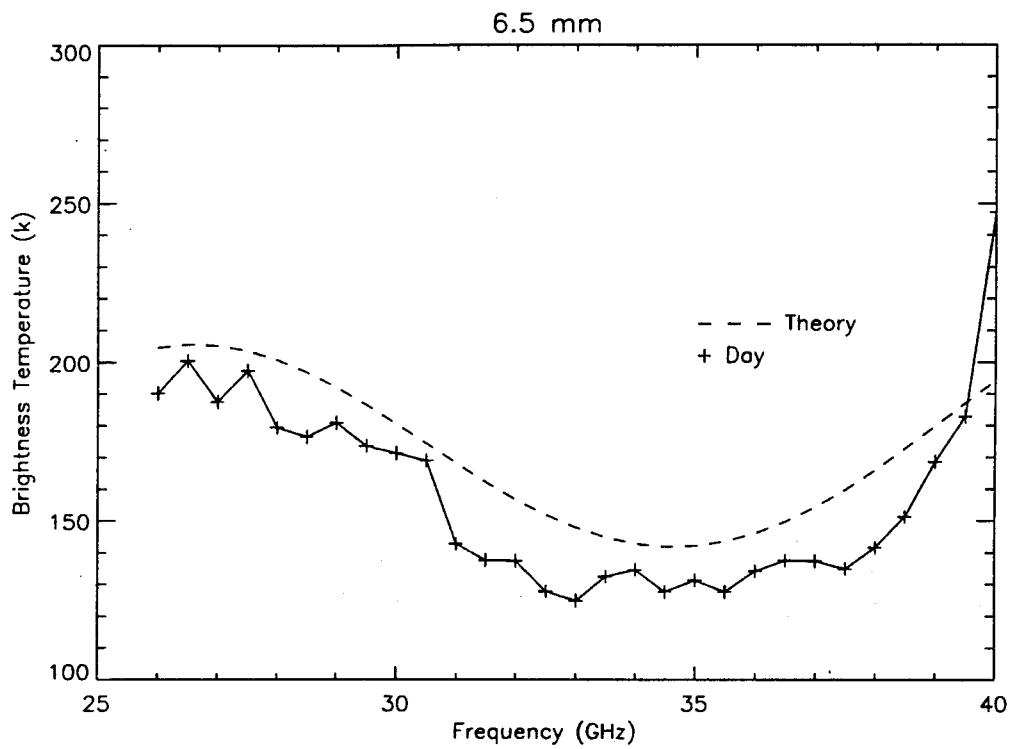
6.5 mm

Figure A-20. Diurnal Comparison, 6.5 mm Estimated Thickness
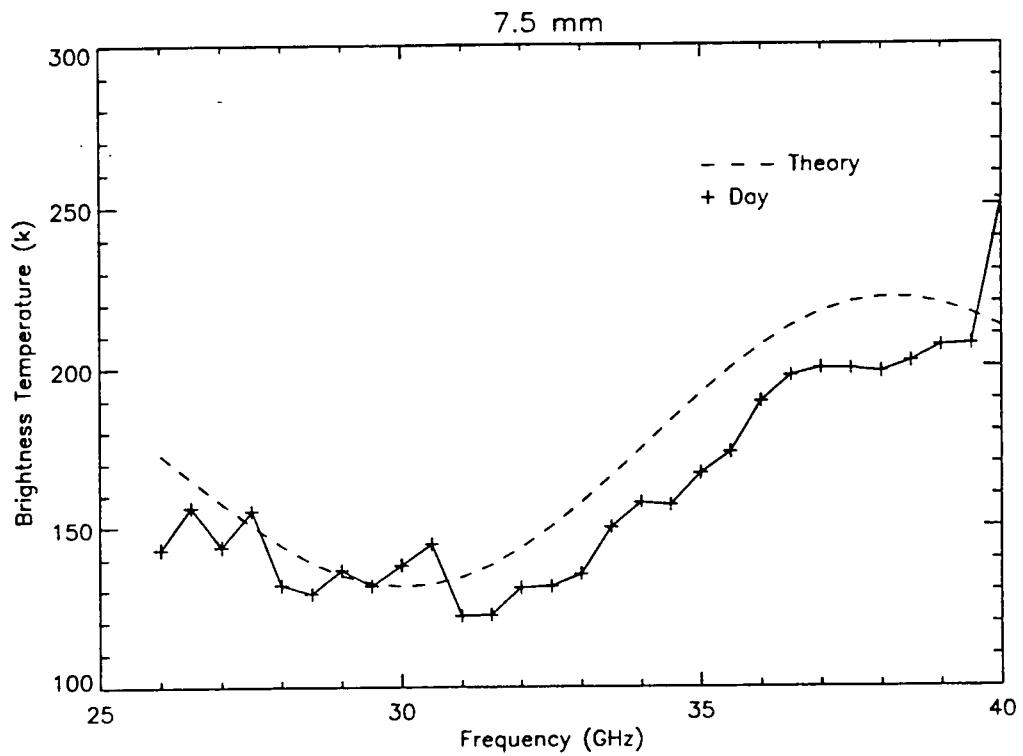
7.5 mm

Figure A-21. Diurnal Comparison, 7.5 mm Estimated Thickness
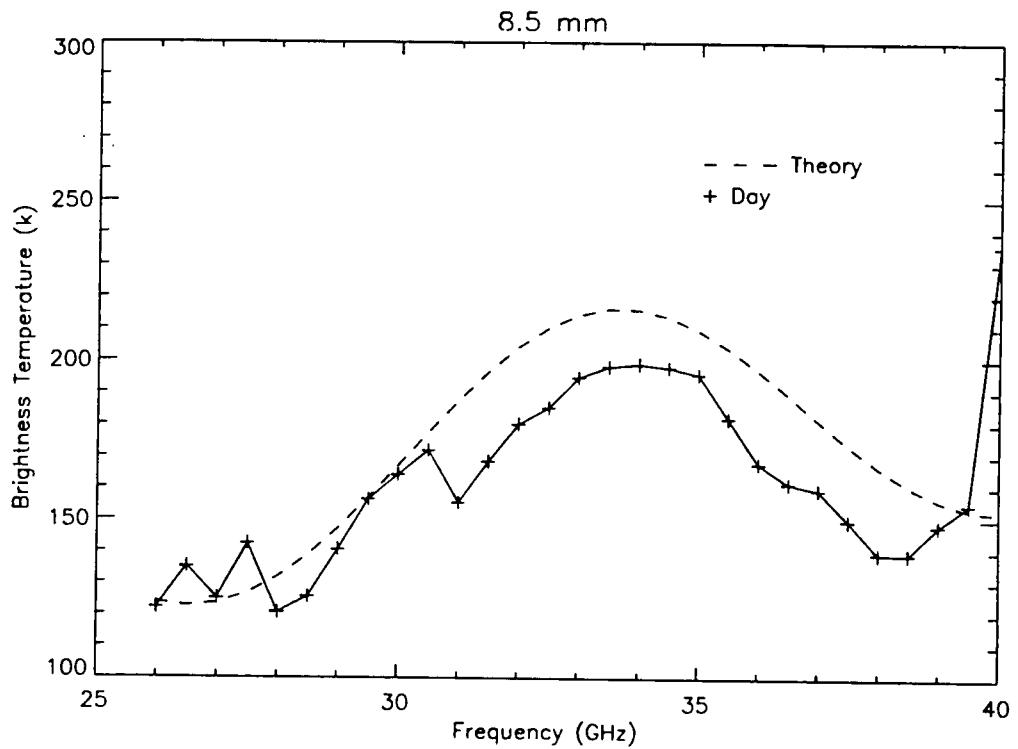
8.5 mm

Figure A-22. Diurnal Comparison, 8.5 mm Estimated Thickness
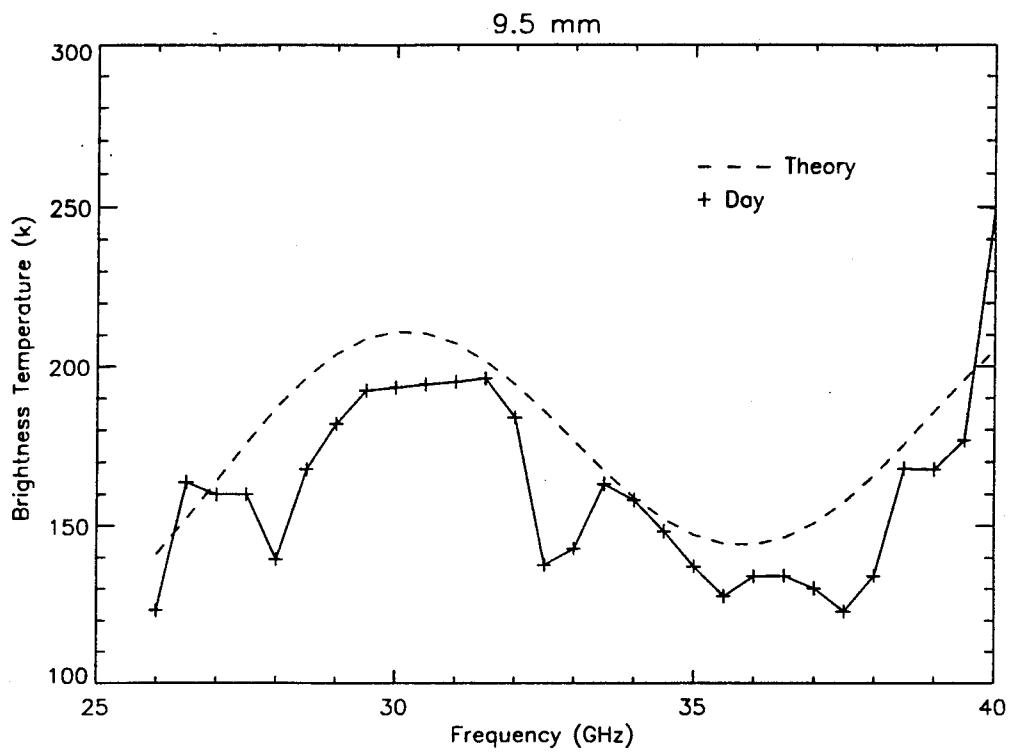
Figure A-23. Diurnal Comparison, 9.5 mm Estimated Thickness
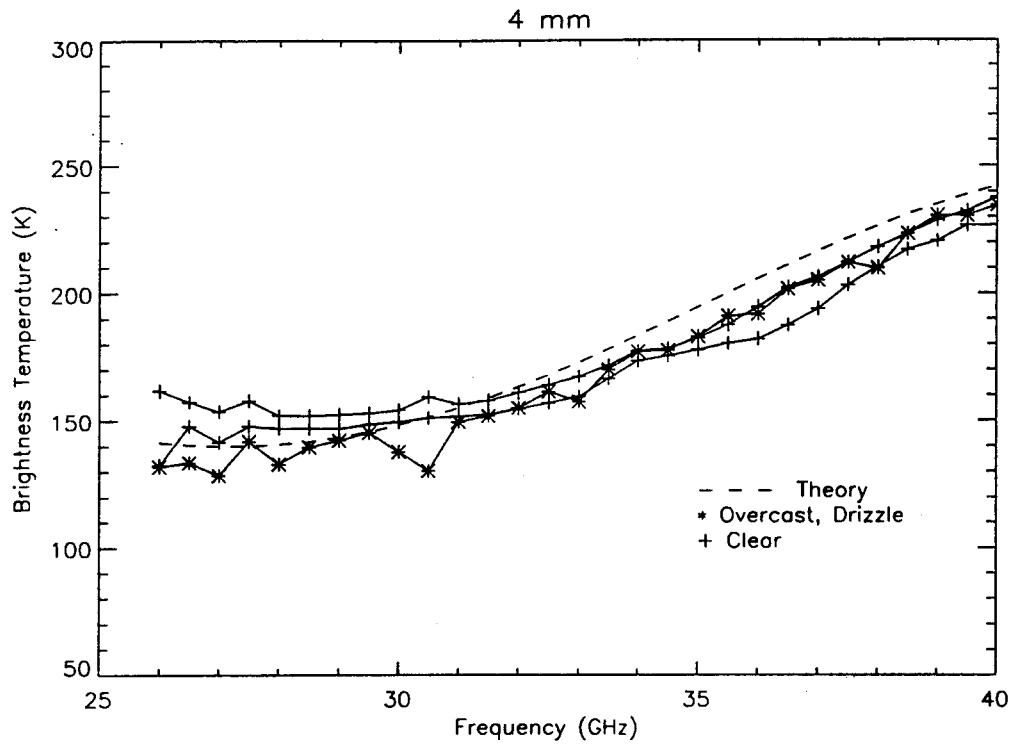
Figure A-24. Weather Comparison, 4 mm Uniform Thickness

5 mm
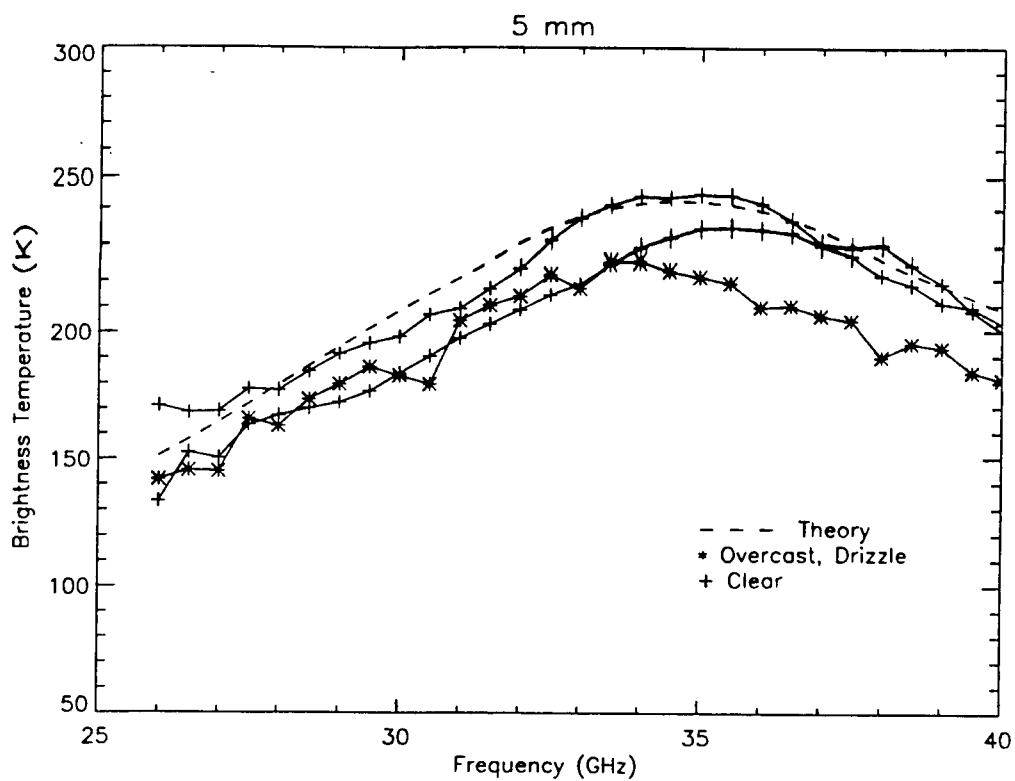
Figure A-25. Weather Comparison, 5 mm Uniform Thickness

6 mm
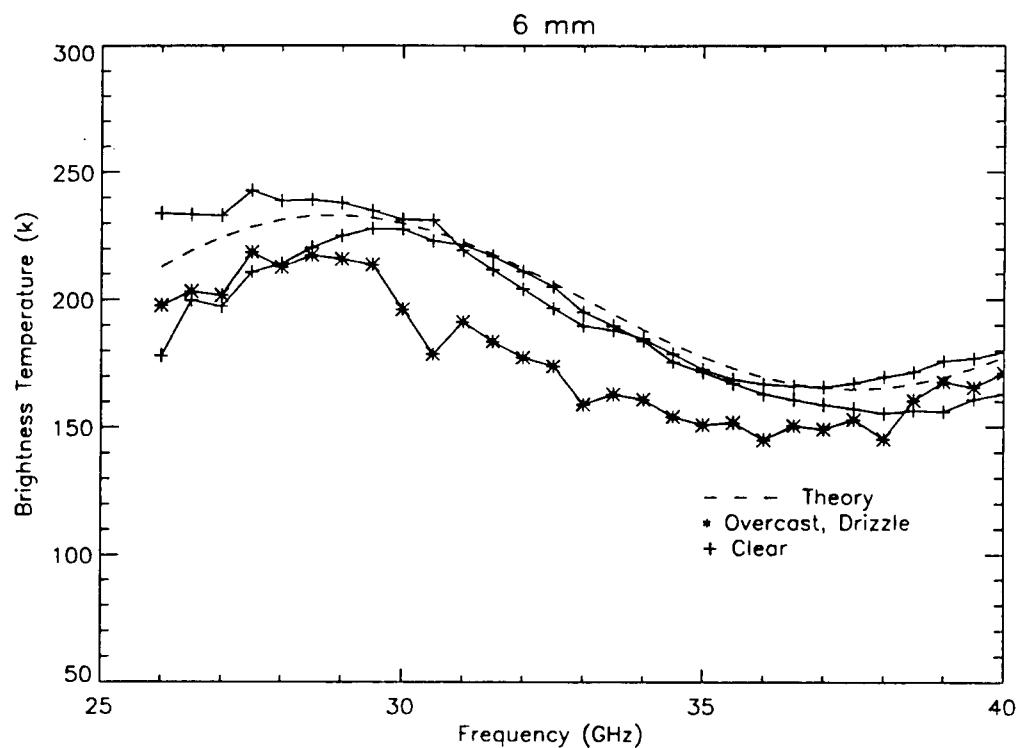
Figure A-26. Weather Comparison, 6 mm Uniform Thickness
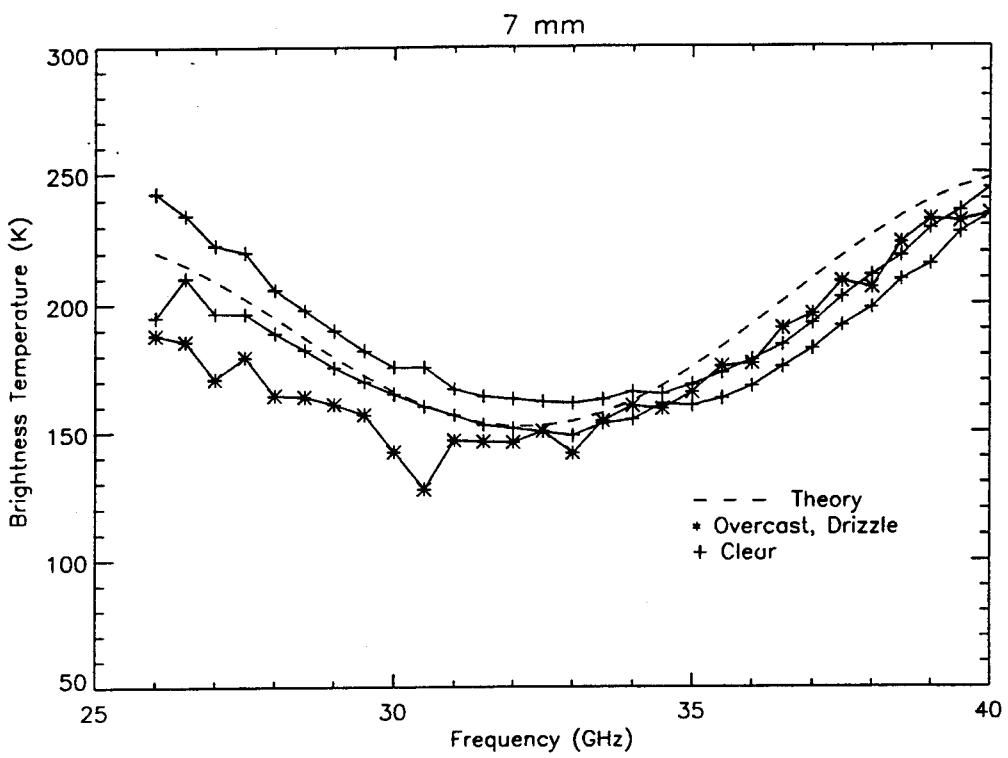
Figure A-27. Weather Comparison, 7 mm Uniform Thickness
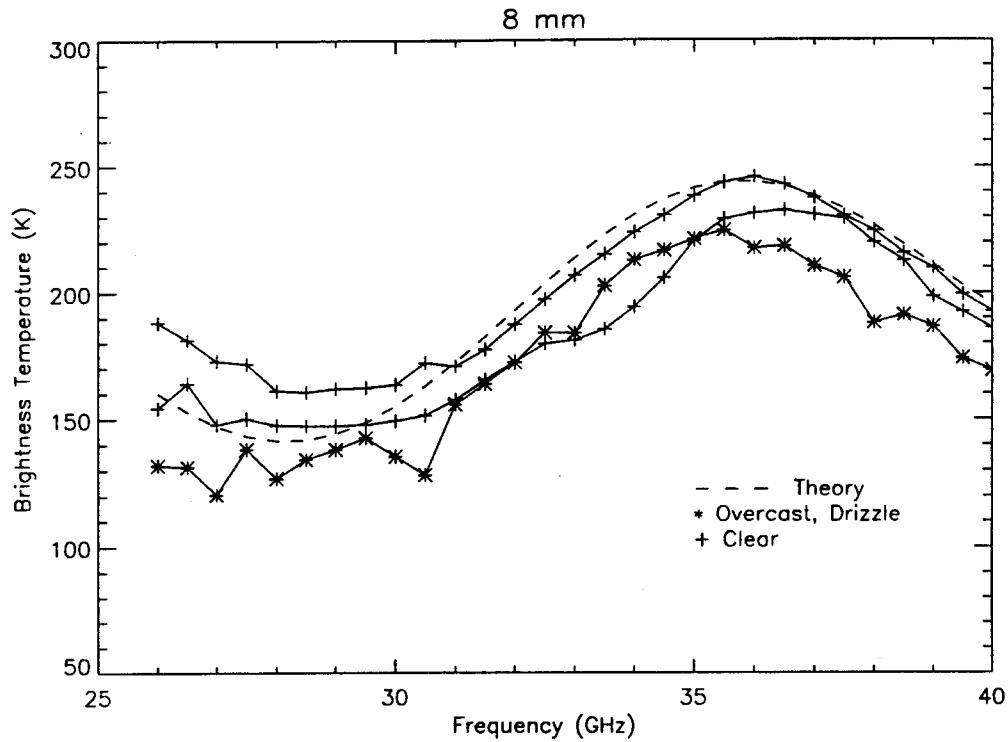
Figure A-28. Weather Comparison, 8 mm Uniform Thickness
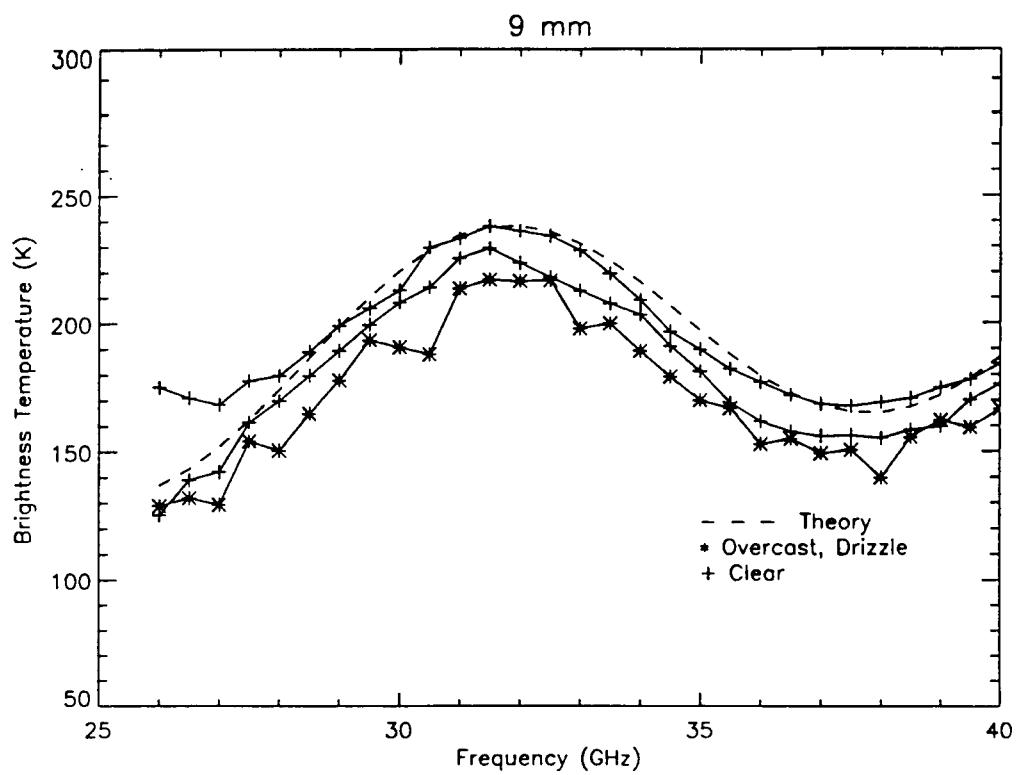
Figure A-29. Weather Comparison, 9 mm Uniform Thickness

APPENDIX B
EMULSION MEASUREMENTS

The complete set of measured data taken during the emulsion tests is included in this appendix. For each plot, the legend describes the water/oil emulsion mix and a theoretical prediction of a nominal brightness temperature for water and for a pure, uniform oil layer at the same thickness .

Figures B-1 to B-7 illustrate results from the emulsified oil measurements. Emulsions variants were 20%, 40% and 55% water by volume. Measurements of emulsions that are available for comparision purposes are 0 mm, 1 mm, 3 mm, 5 mm, 7 mm, 9 mm, and 10 mm thicknesses.
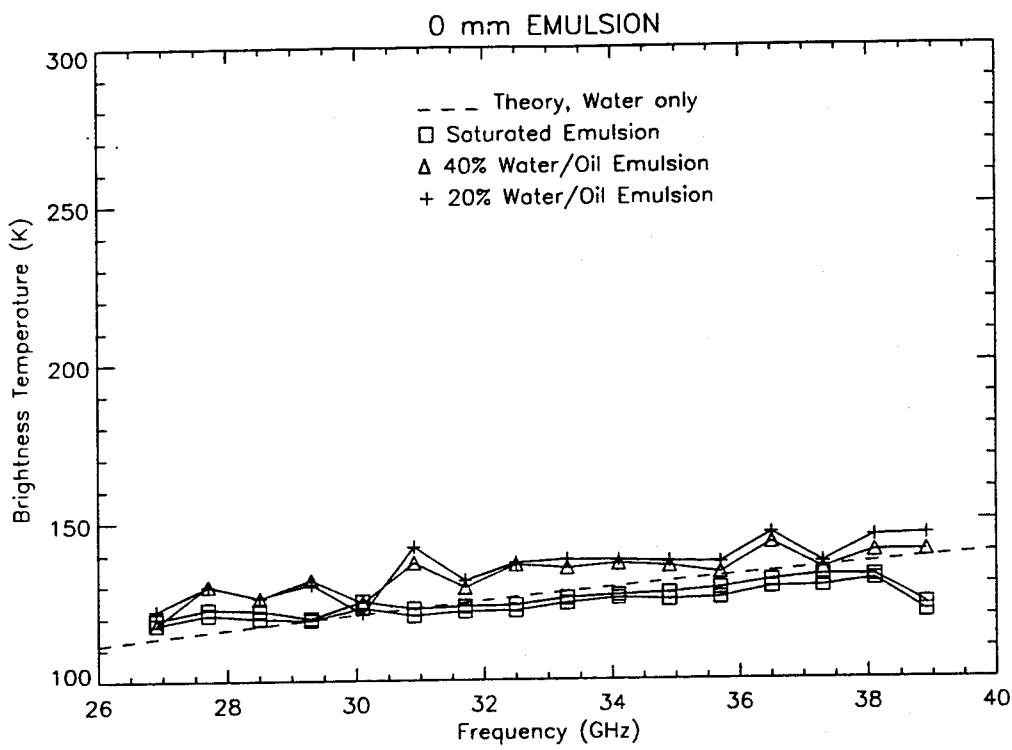
Figure B-1. Emulsified Oil, Water
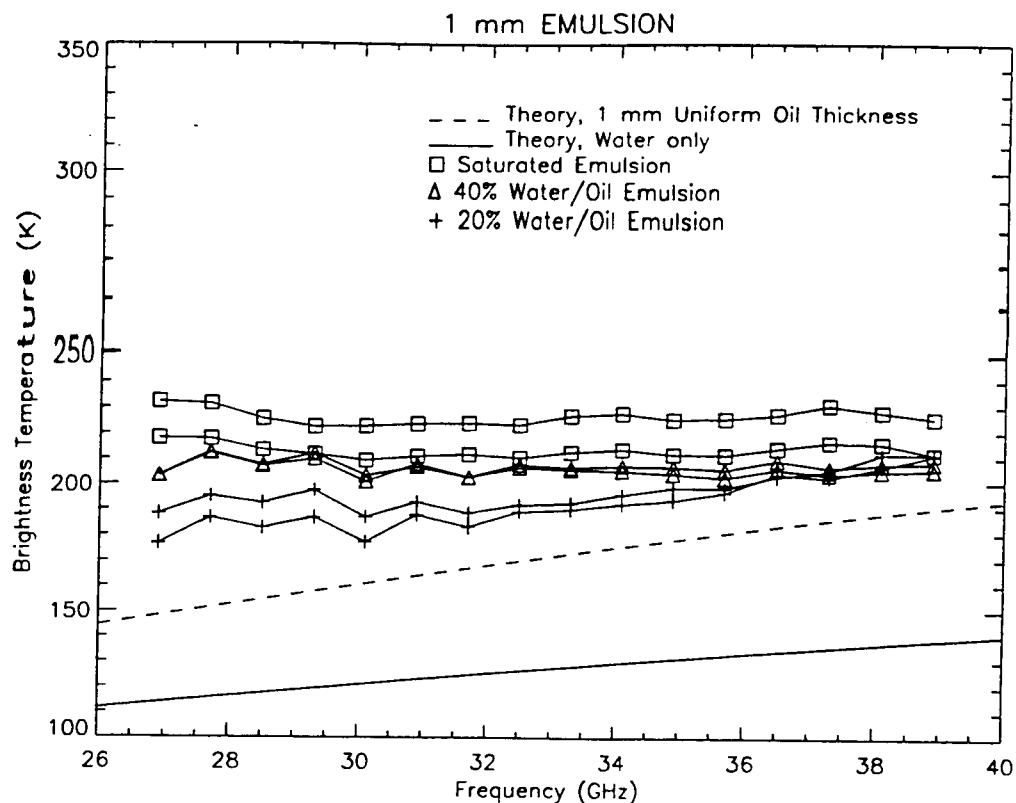
Figure B-2. Emulsified Oil, 1 mm Thickness
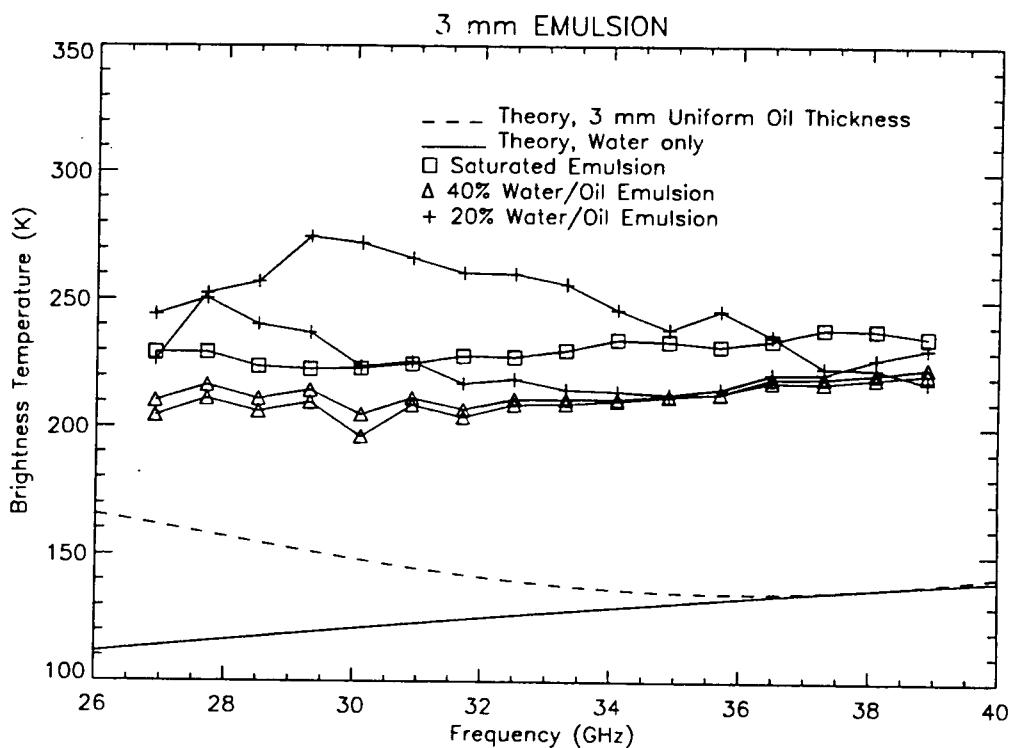
Figure B-3. Emulsified Oil, 3 mm Thickness
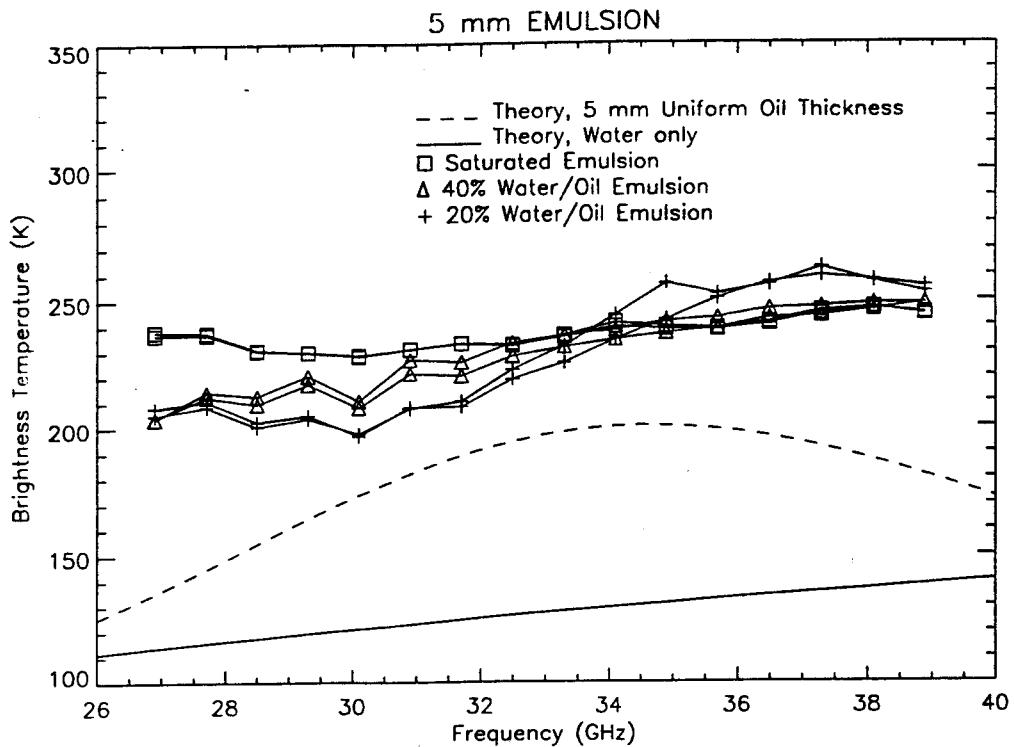
Figure B-4. Emulsified Oil, 5 mm Thickness
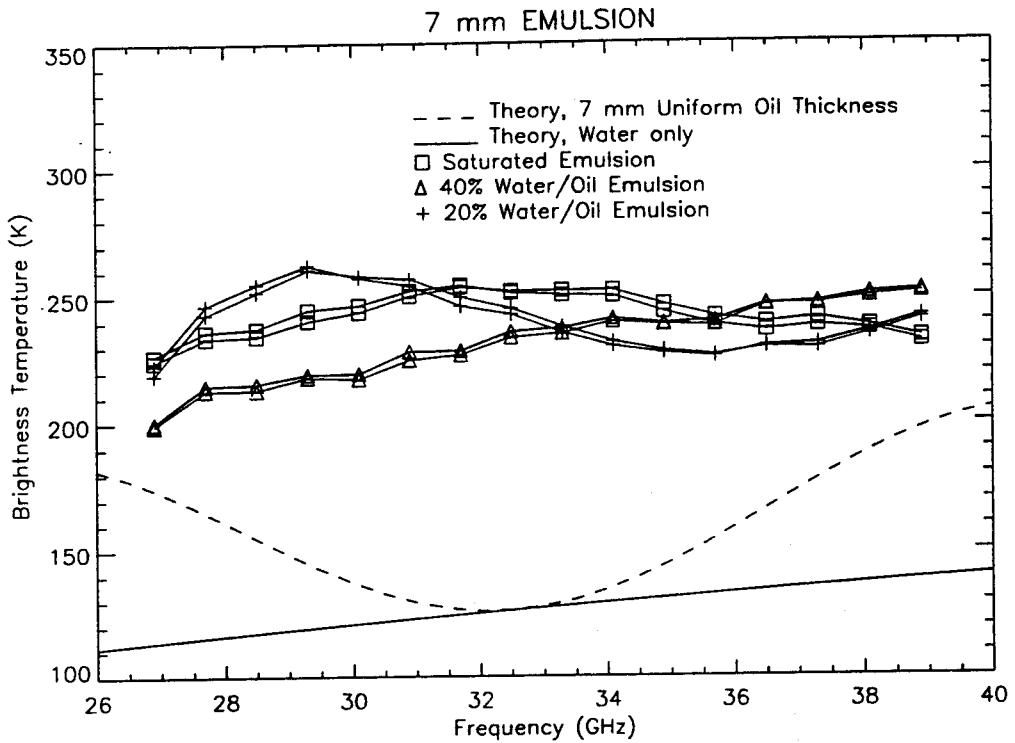
Figure B-5. Emulsified Oil, 7 mm Thickness
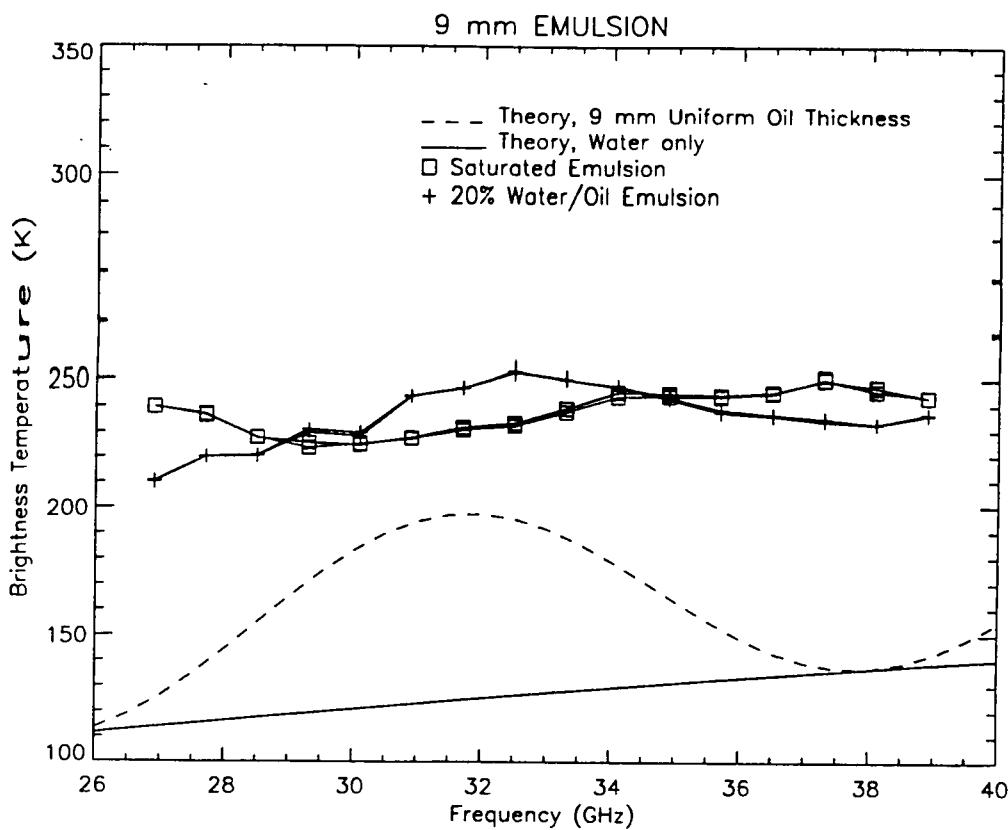
Figure B-6. Emulsified Oil, 9 mm Thickness
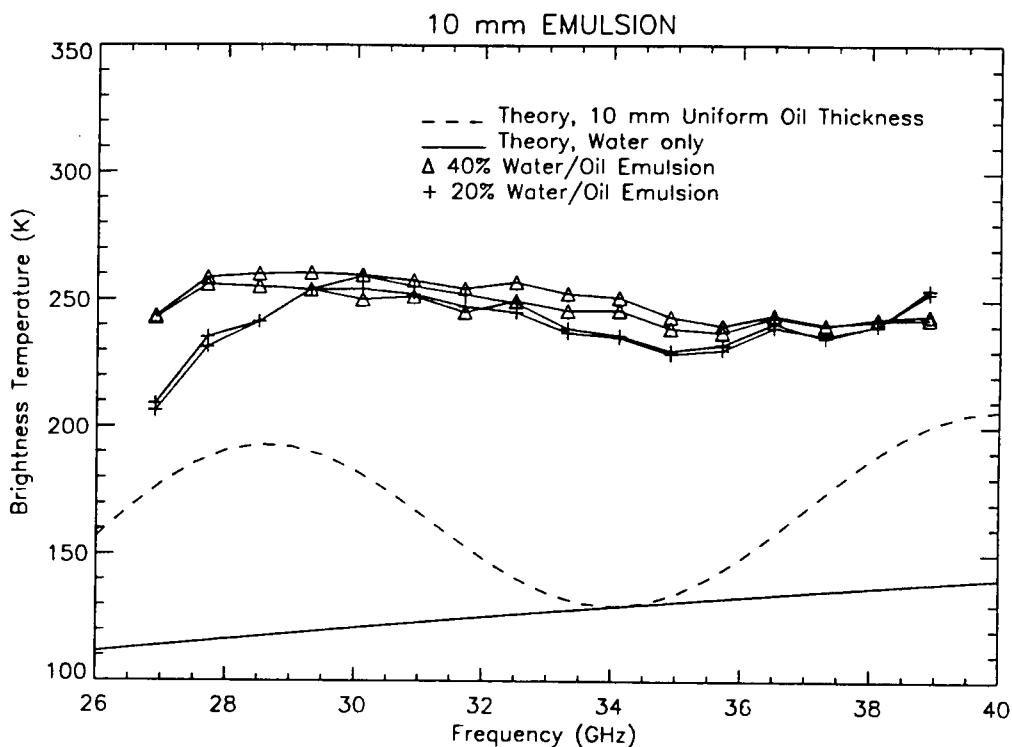
Figure B-7. Emulsified Oil, 10 mm Thickness

APPENDIX C
NON-UNIFORM THICKNESS MEASUREMENTS

The complete set of measured data for non-uniform oil thickness tests is included as this appendix. For each plot, the legend describes the attributes of the measured oil layer and a theoretical prediction of a nominal brightness temperature is included.

Figures C-1 to C-11 illustrate the results from the split tank measurements. The antenna was placed such that each of the two different uniform thicknesses covered 50% of the antenna field-of-view.

Figures C-12 to C-21 illustrate the results from the step thickness function measurements. Oil of the given depth was constrained in vertical mylar cylinders. The liquid surrounding the cylinders contained a sheen oil layer of approximately 0.5 mm thickness. The step function of oil thickness covered an area of approximately 60% in the antenna field-of-view.

Figures C-22 to C-25 illustrate the results from the step thickness gradient measurements. The thickness gradient consisted of six vertically-oriented mylar cylinders. Oil was poured into each of the cylinders to form a "wedding cake", or staircase gradient from a background of 0 mm, increasing in 0.5 mm steps to 2.5 mm. The center cylinder thickness is the reported depth (3 mm, 6 mm, and 9 mm).

Figures C-26 to C-34 illustrate the results from the patchy thickness measurements. Three vertically oriented mylar cylinders constrained the oil to the given depths. The patchy oil thickness covered an area of approximately 50% in the antenna field-of-view.
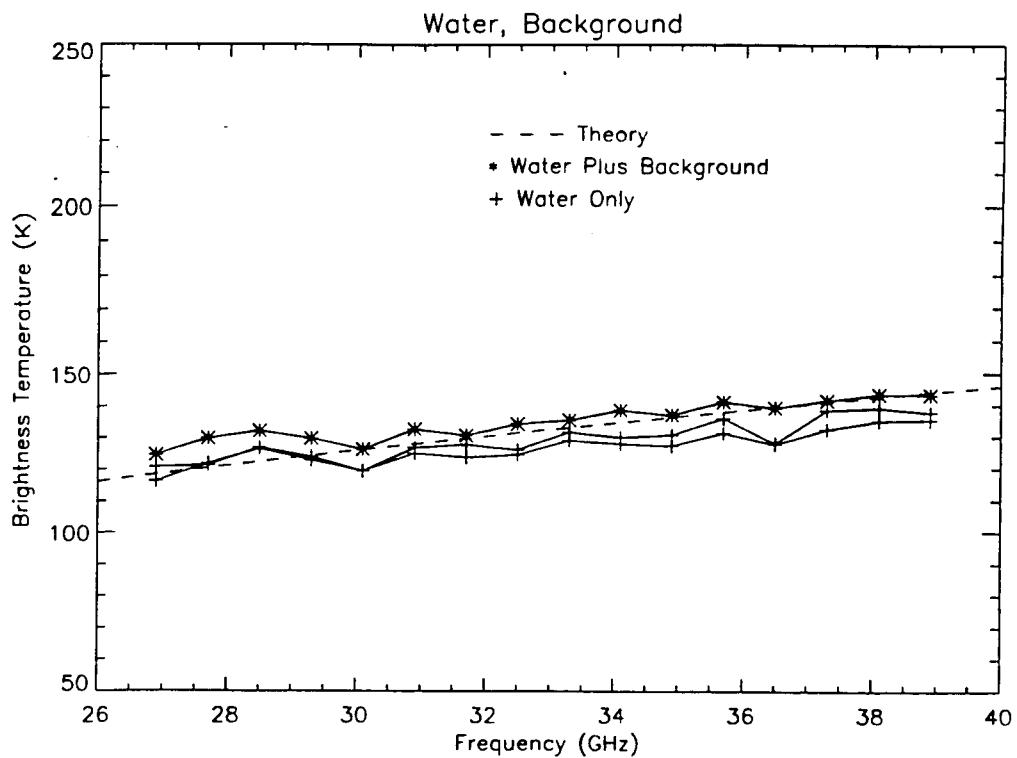
Water, Background

Figure C-1. Split Tank Measurement, Water and Background

0,1 mm
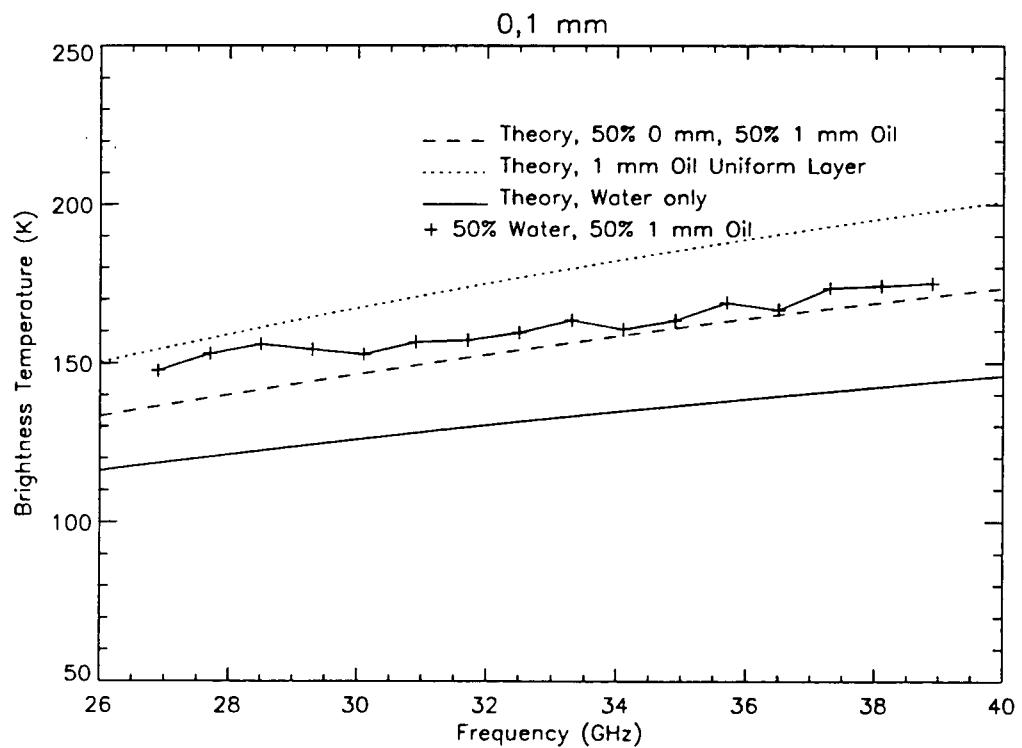
Figure C-2. Split Tank Measurement, 0 mm and 1 mm Oil

C-2
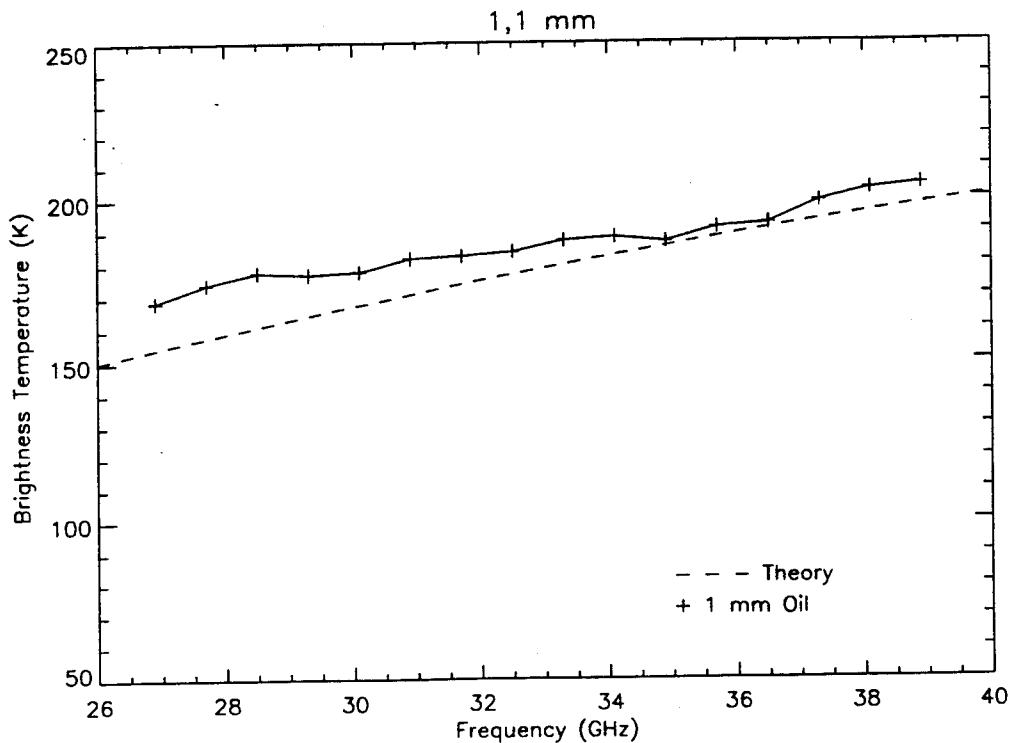
Figure C-3. Split Tank Measurement, 1 mm and 1 mm Oil
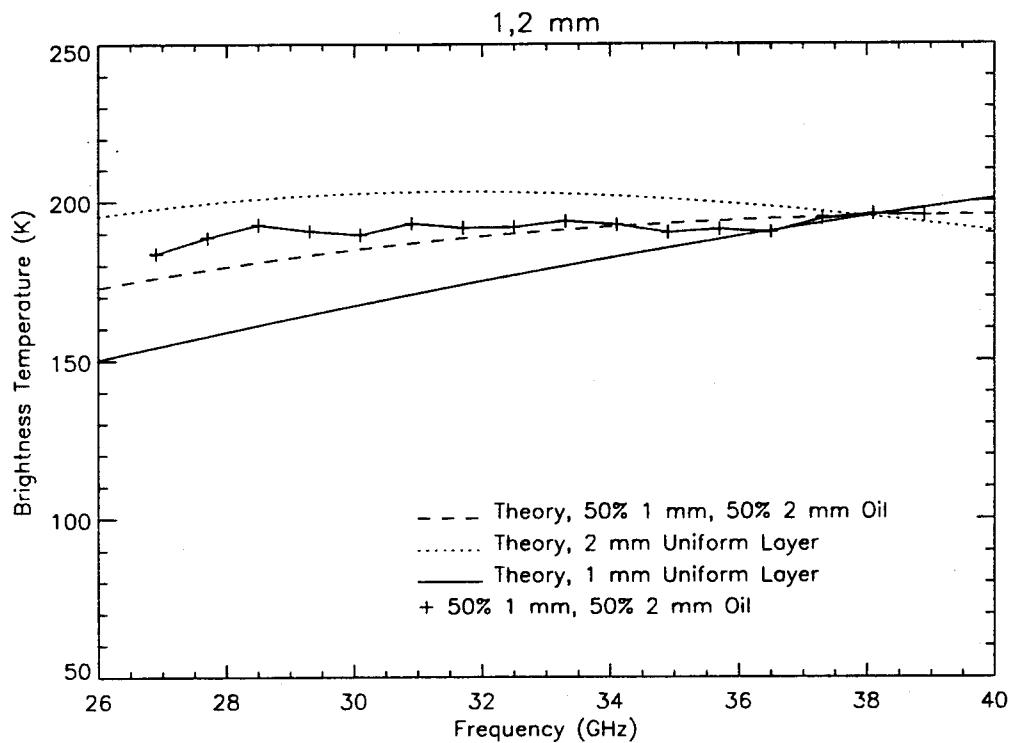
Figure C-4. Split Tank Measurement, 1 mm and 2 mm Oil
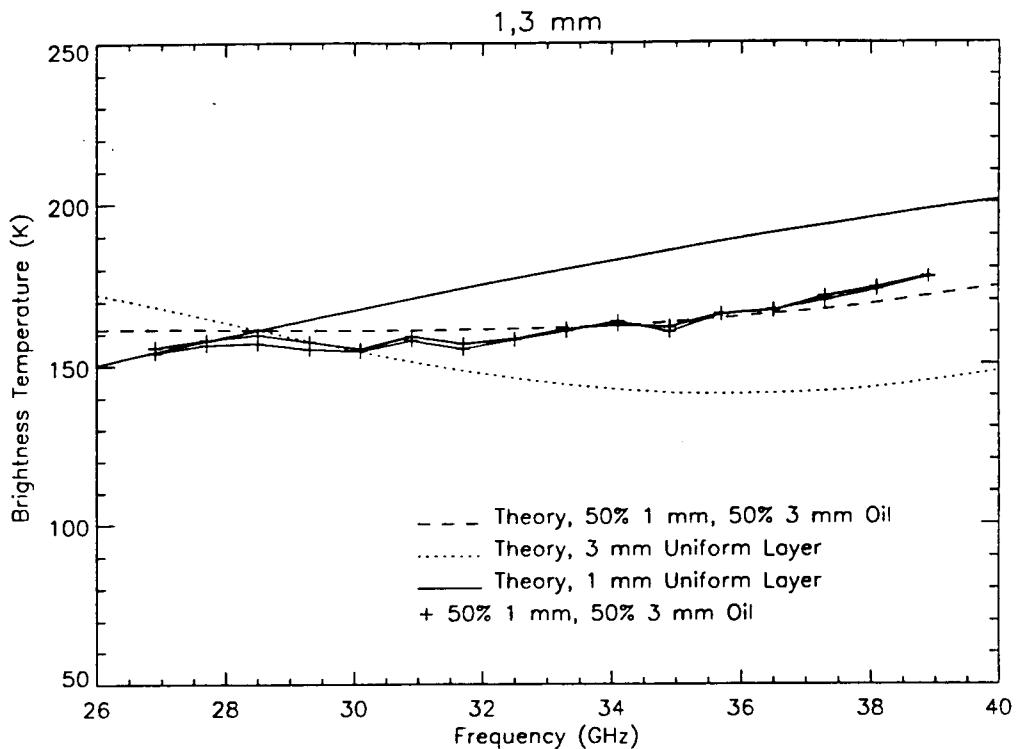
Figure C-5. Split Tank Measurement, 1 mm and 3 mm Oil
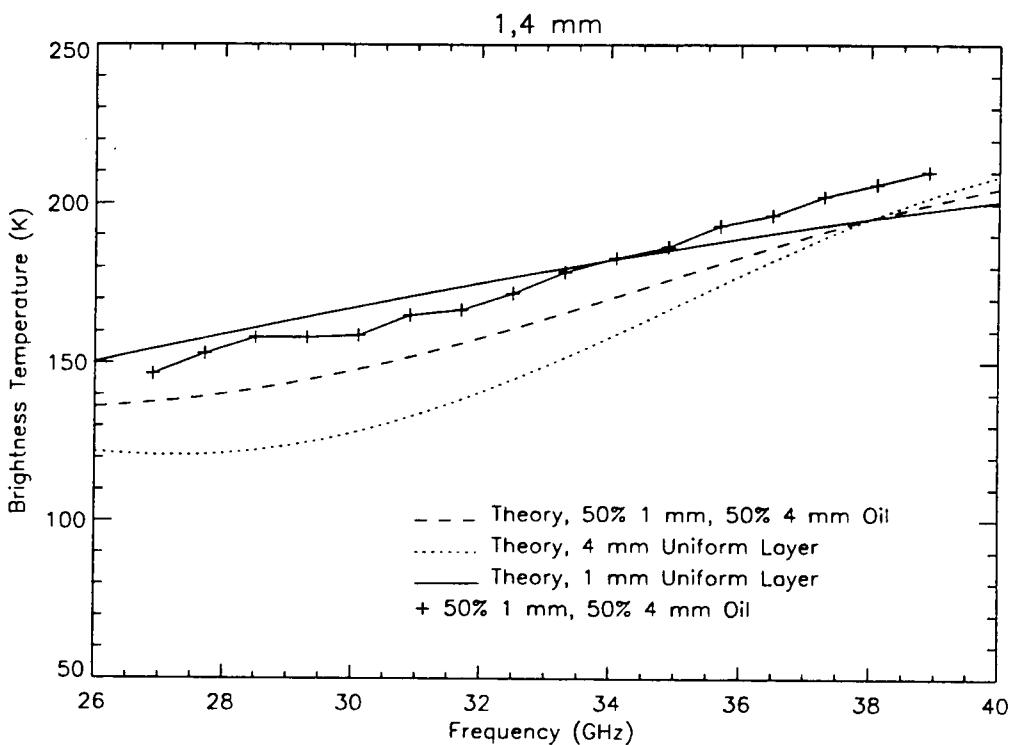
Figure C-6. Split Tank Measurement, 1 mm and 4 mm Oil
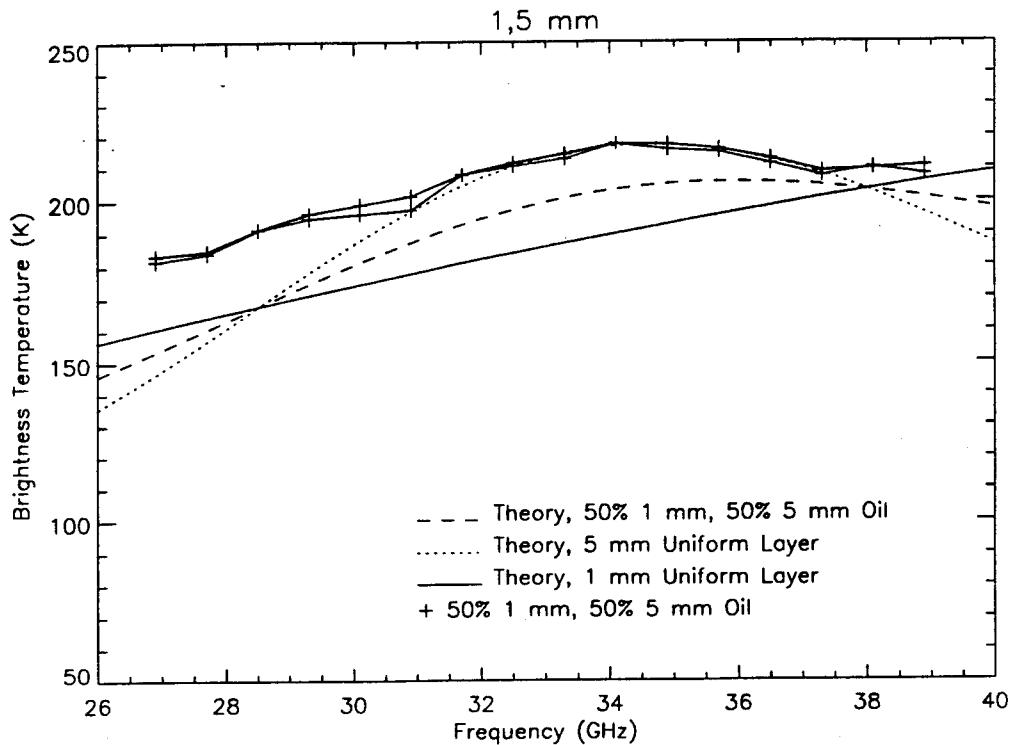
Figure C-7. Split Tank Measurement, 1 mm and 5 mm Oil
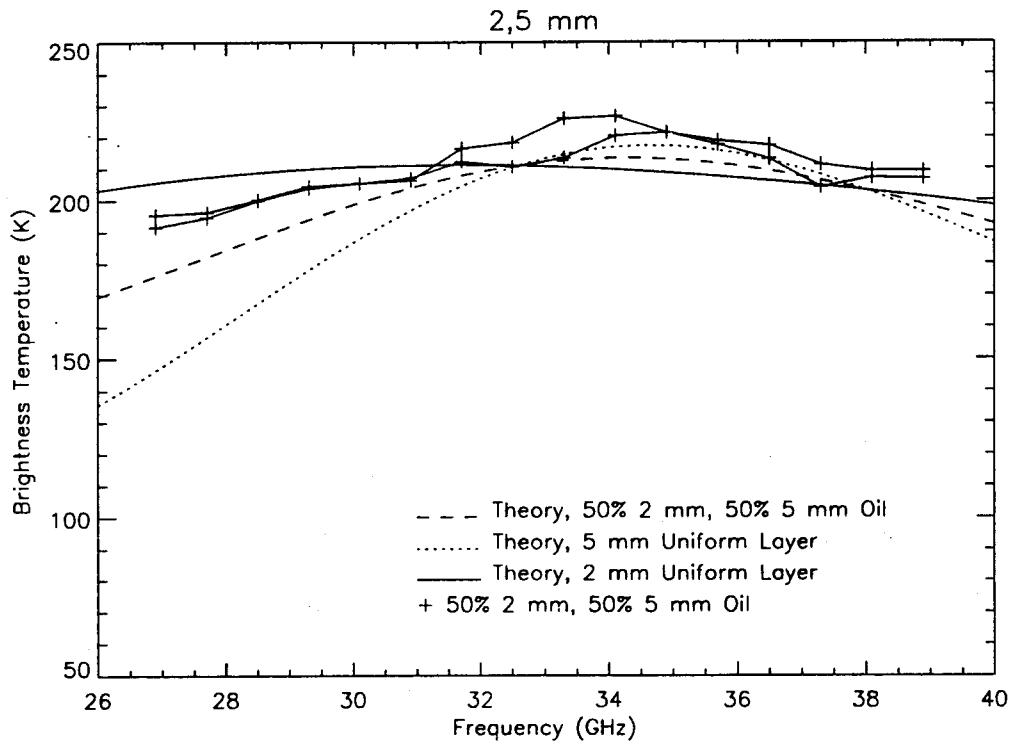
Figure C-8. Split Tank Measurement, 2 mm and 5 mm Oil
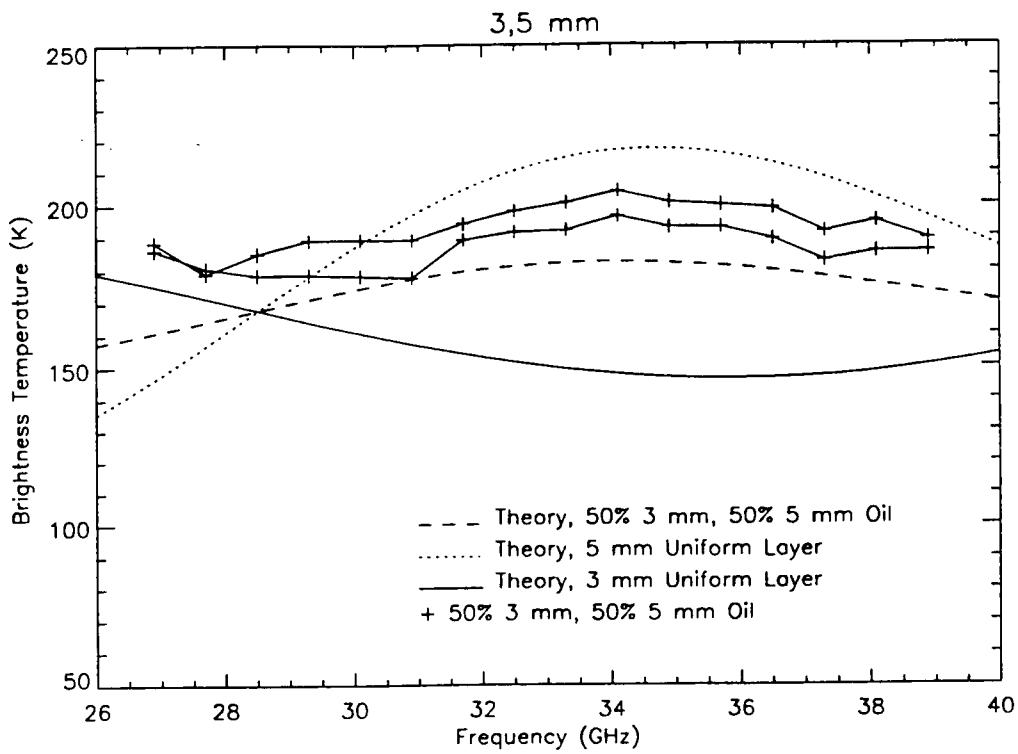
Figure C-9. Split Tank Measurement, 3 mm and 5 mm Oil
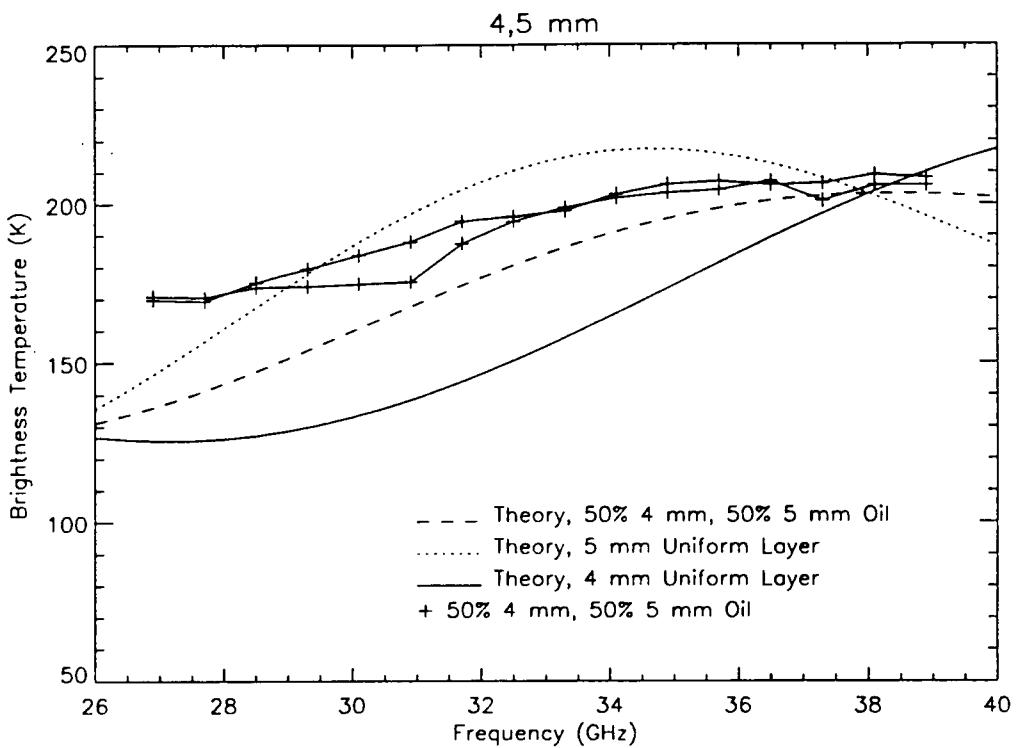
Figure C-10. Split Tank Measurement, 4 mm and 5 mm Oil

5,5 mm
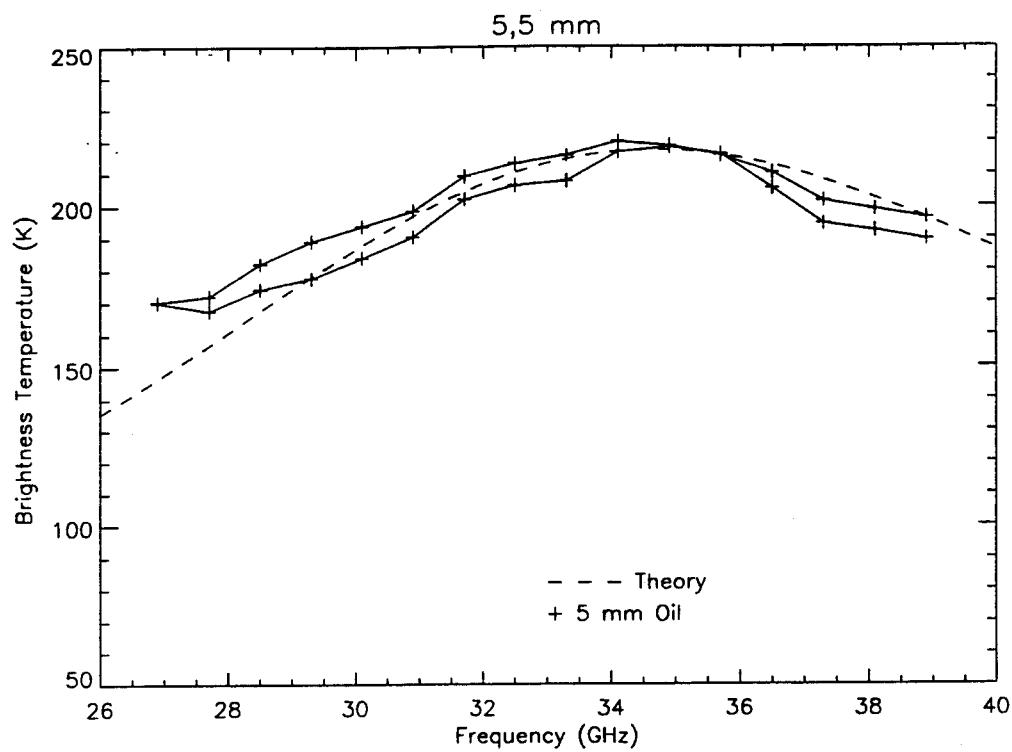
Figure C-11. Split Tank Measurement, 5 mm and 5 mm Oil

Water Plus Background
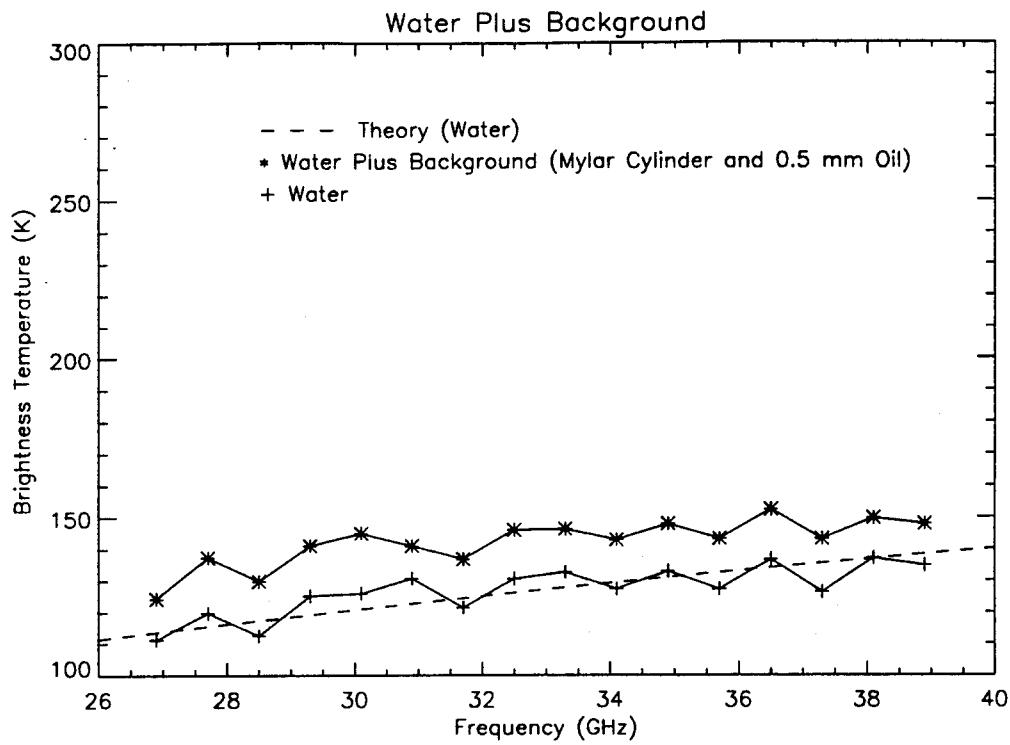
Figure C-12. Step Function, Water and Background

C-7
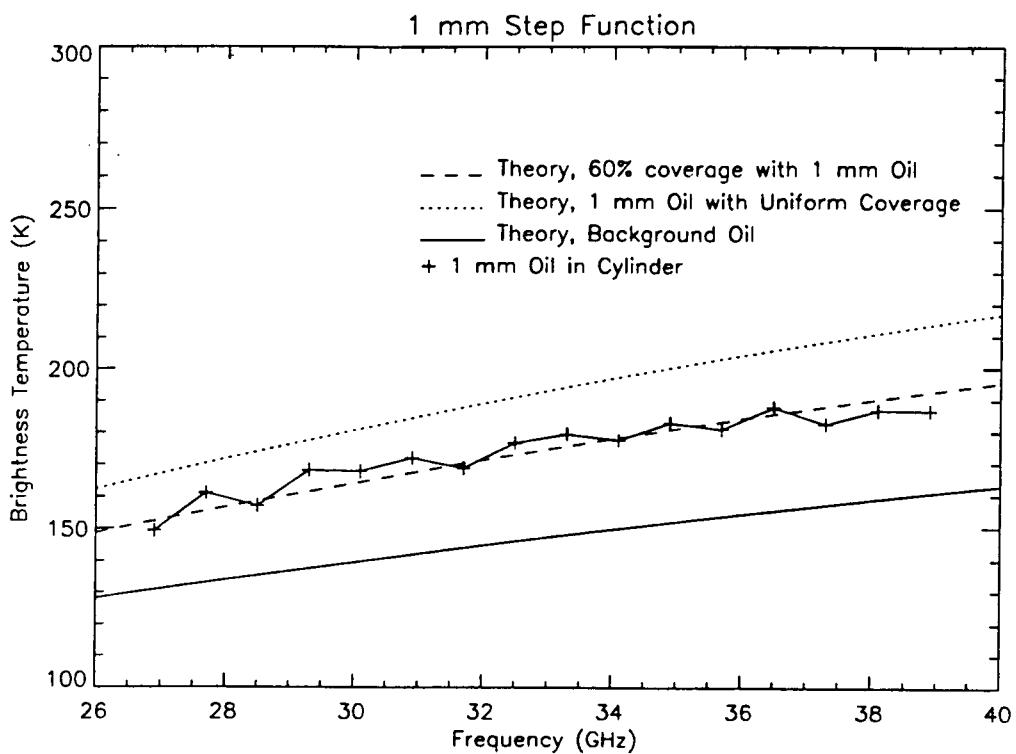
Figure C-13. Step Function, 1 mm Oil
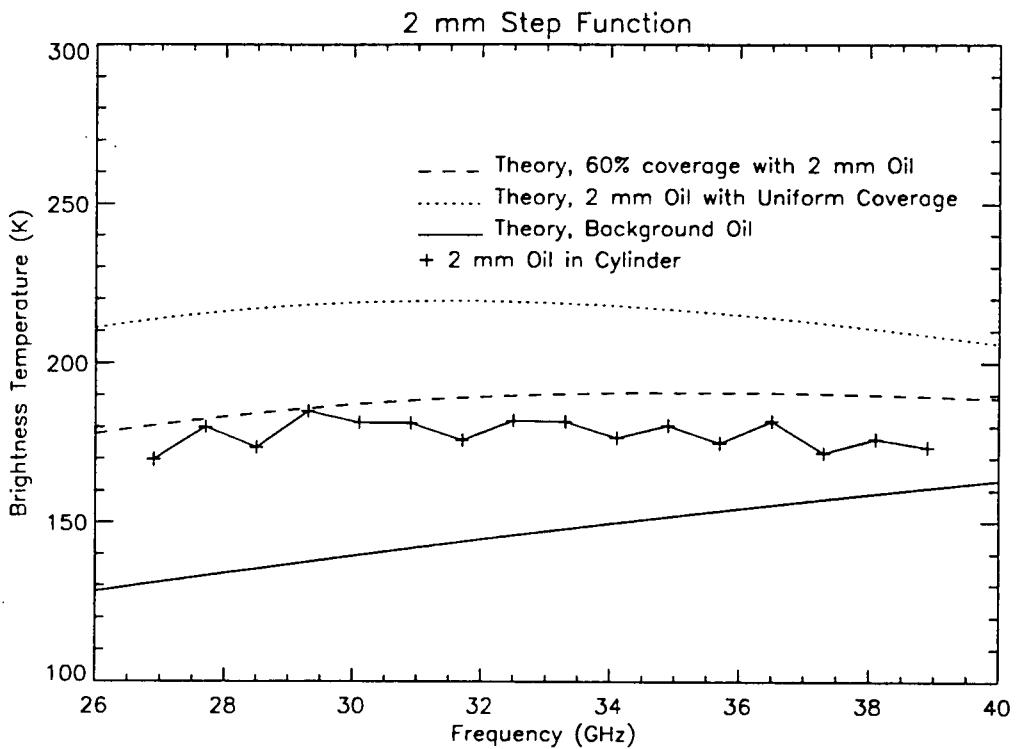
Figure C-14. Step Function, 2 mm Oil
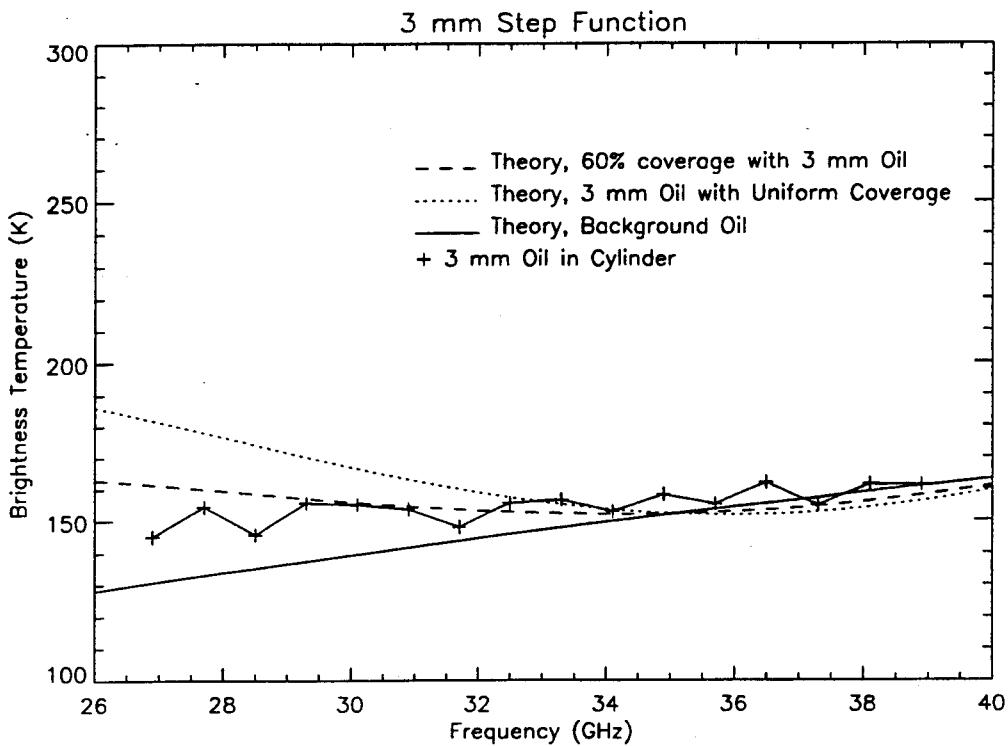
3 mm Step Function

Figure C-15. Step Function, 3 mm Oil
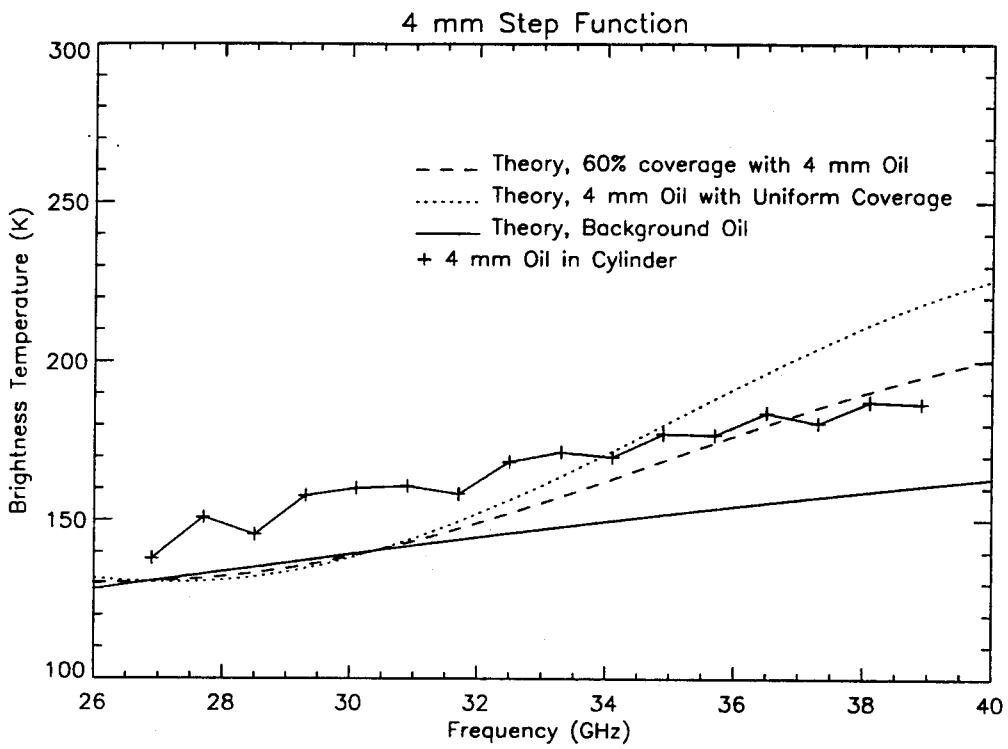
4 mm Step Function

Figure C-16. Step Function, 4 mm Oil
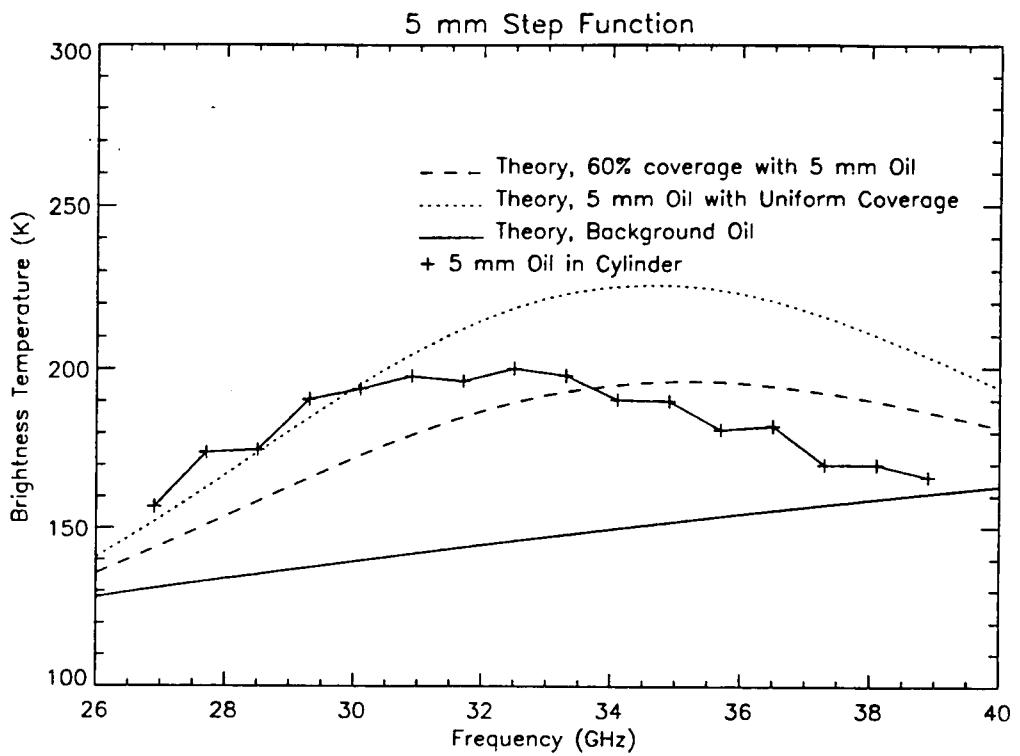
Figure C-17. Step Function, 5 mm Oil
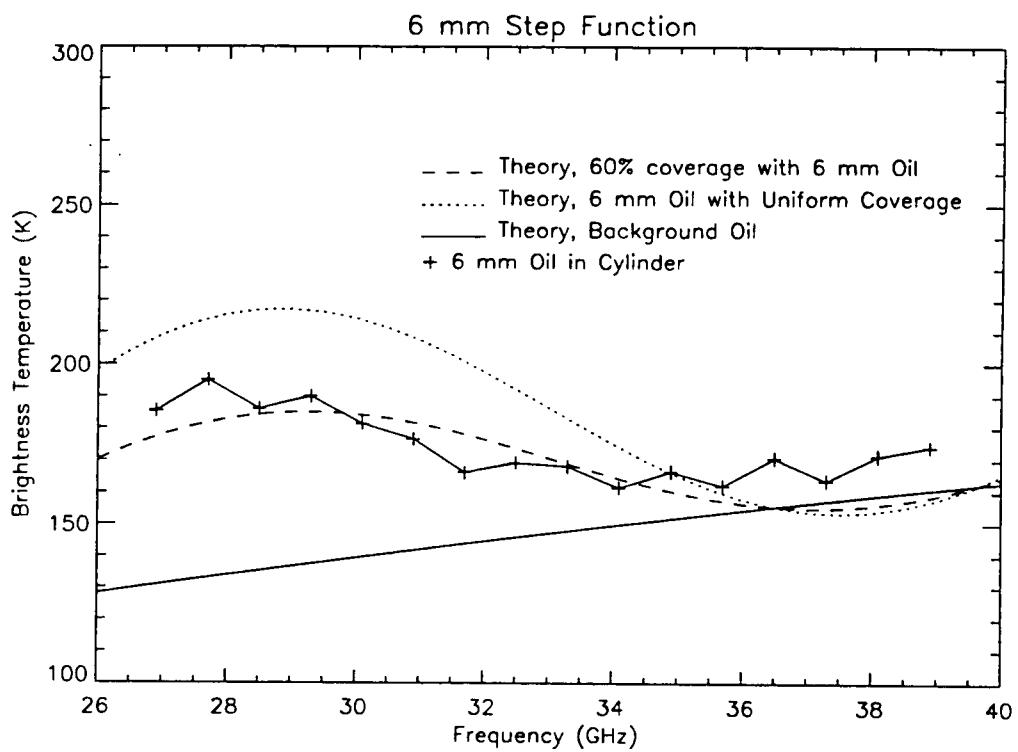
Figure C-18. Step Function, 6 mm Oil
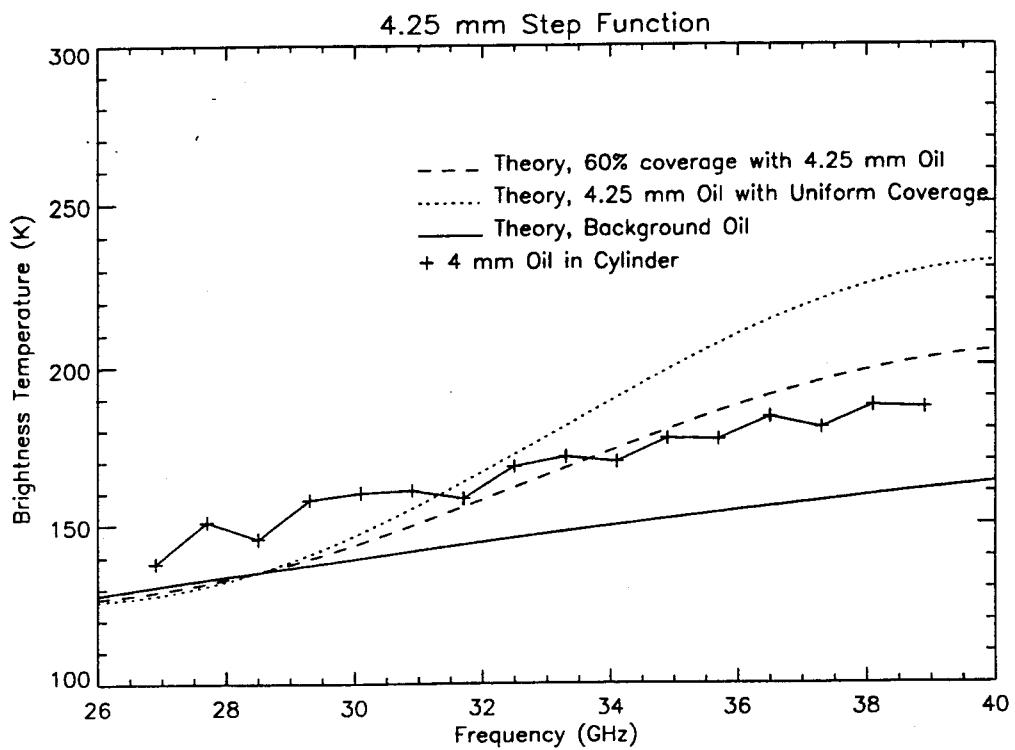
Figure C-19. Step Function, 4.25 mm Estimated Oil Thickness
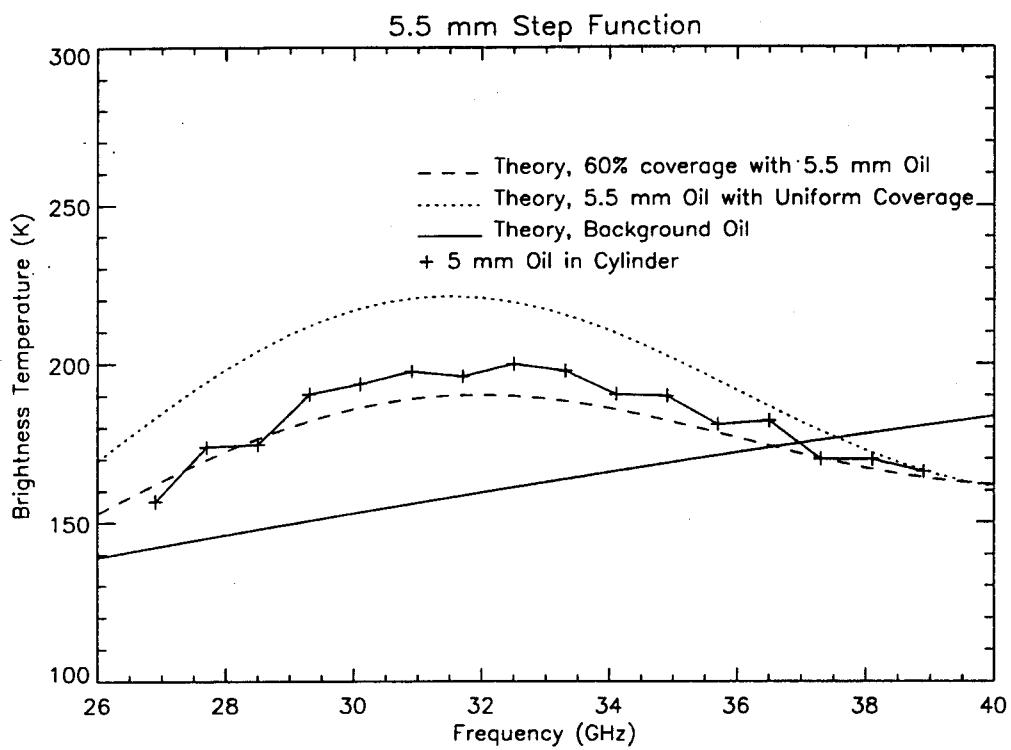
Figure C-20. Step Function, 5.5 mm Estimated Oil Thickness

C-11
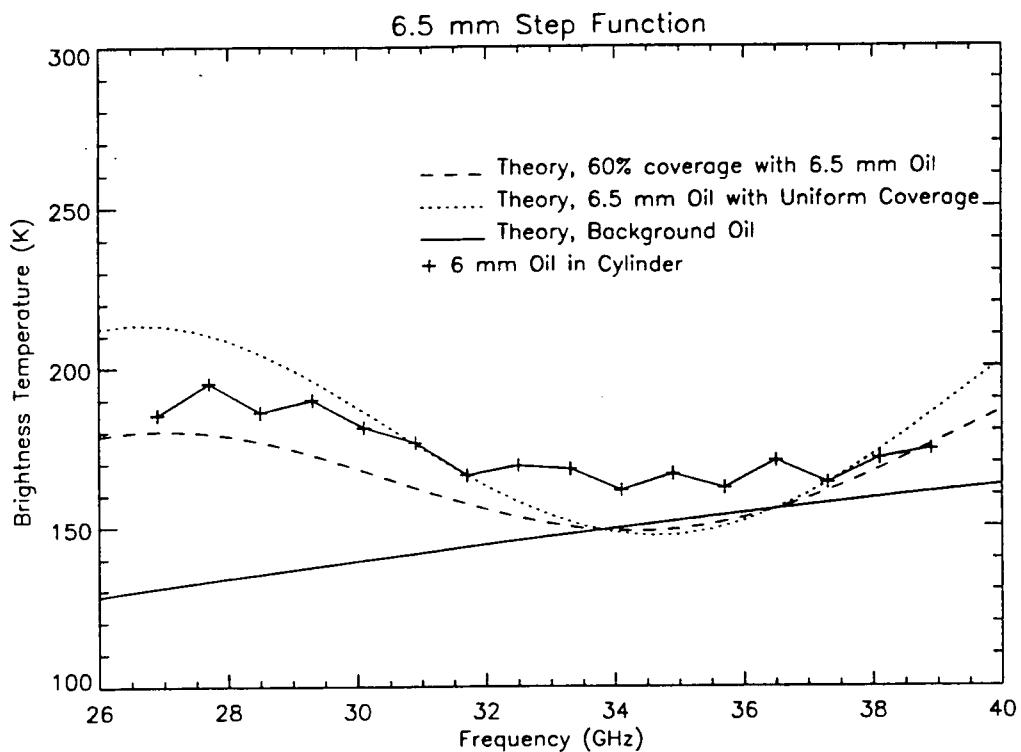
Figure C-21. Step Function, 6.5 mm Estimated Oil Thickness
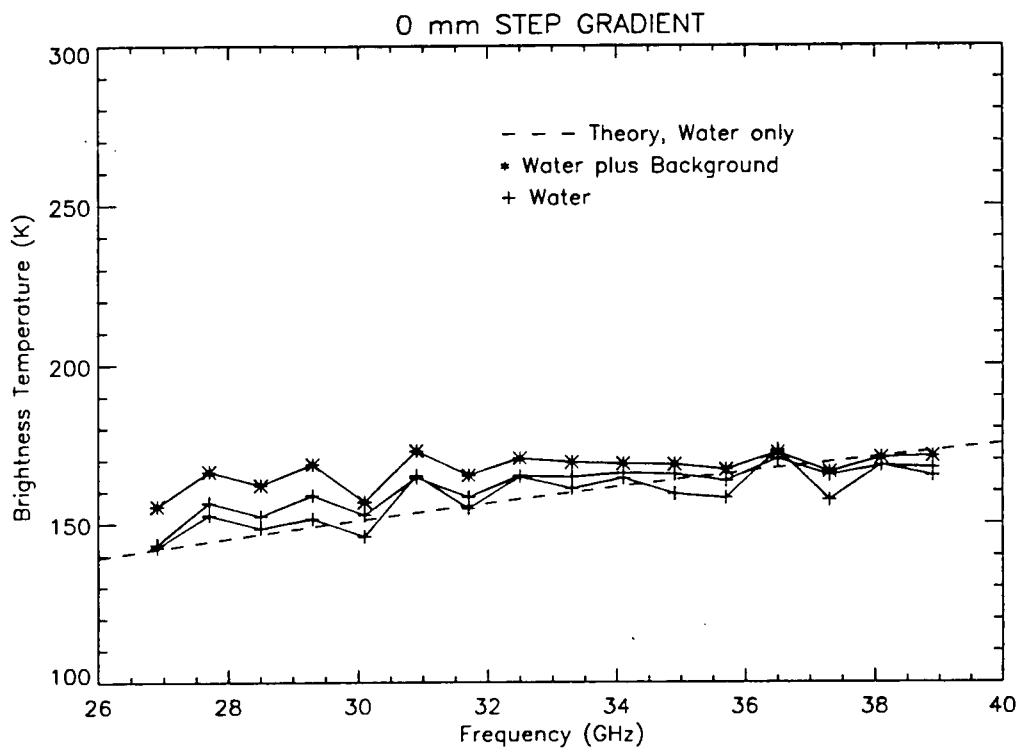
Figure C-22. Step Gradient, Water and Background
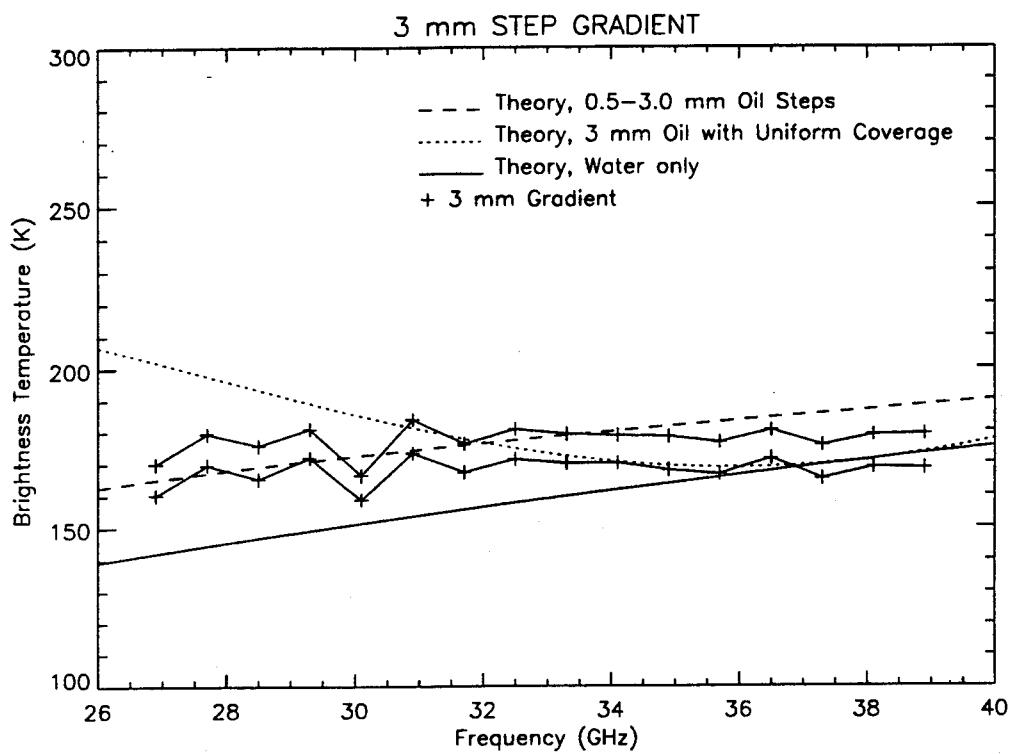
3 mm STEP GRADIENT

Figure C-23. Step Gradient, 3 mm Oil in Center Ring
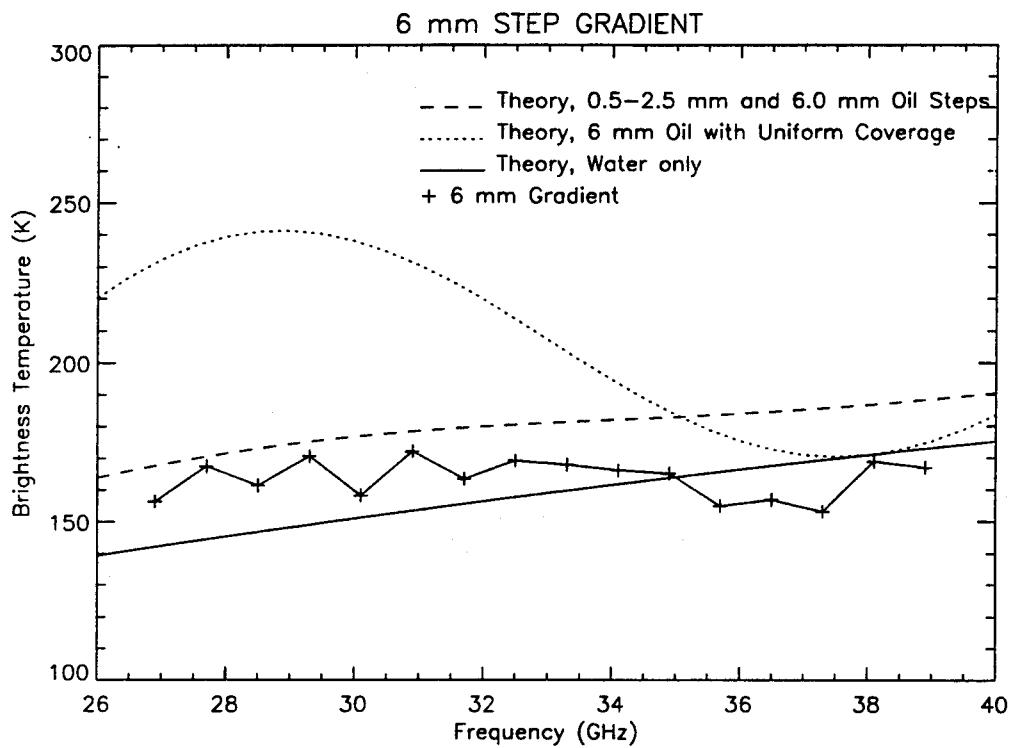
6 mm STEP GRADIENT

Figure C-24. Step Gradient, 6 mm Oil in Center Ring

C-13
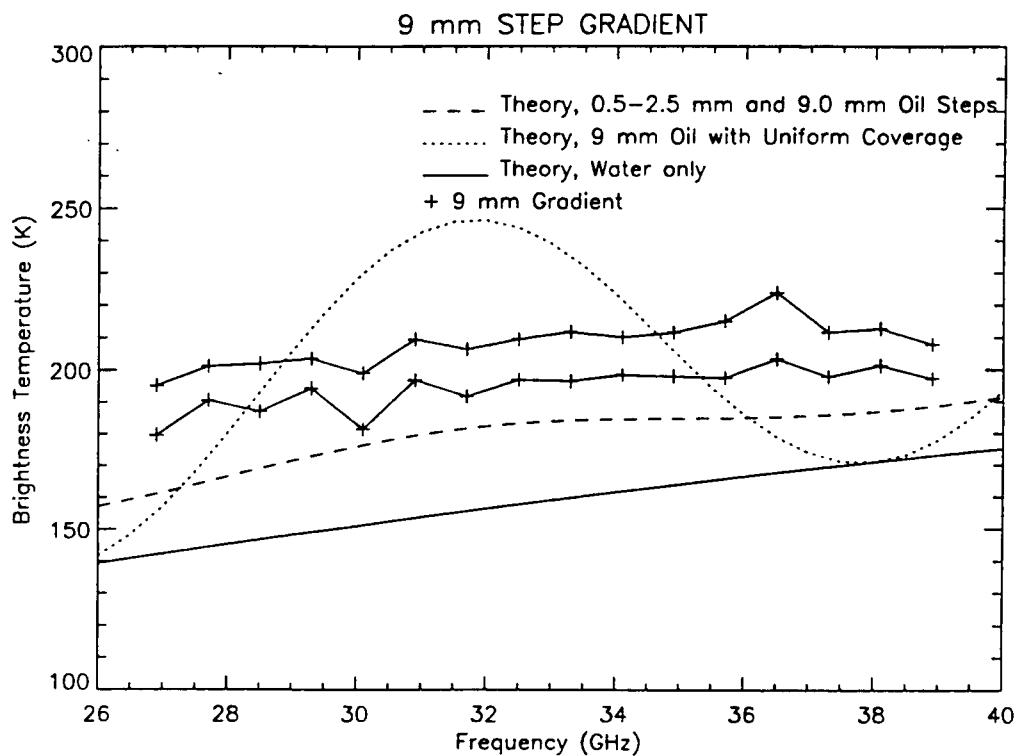
9 mm STEP GRADIENT

Figure C-25. Step Gradient, 9 mm Oil in Center Ring
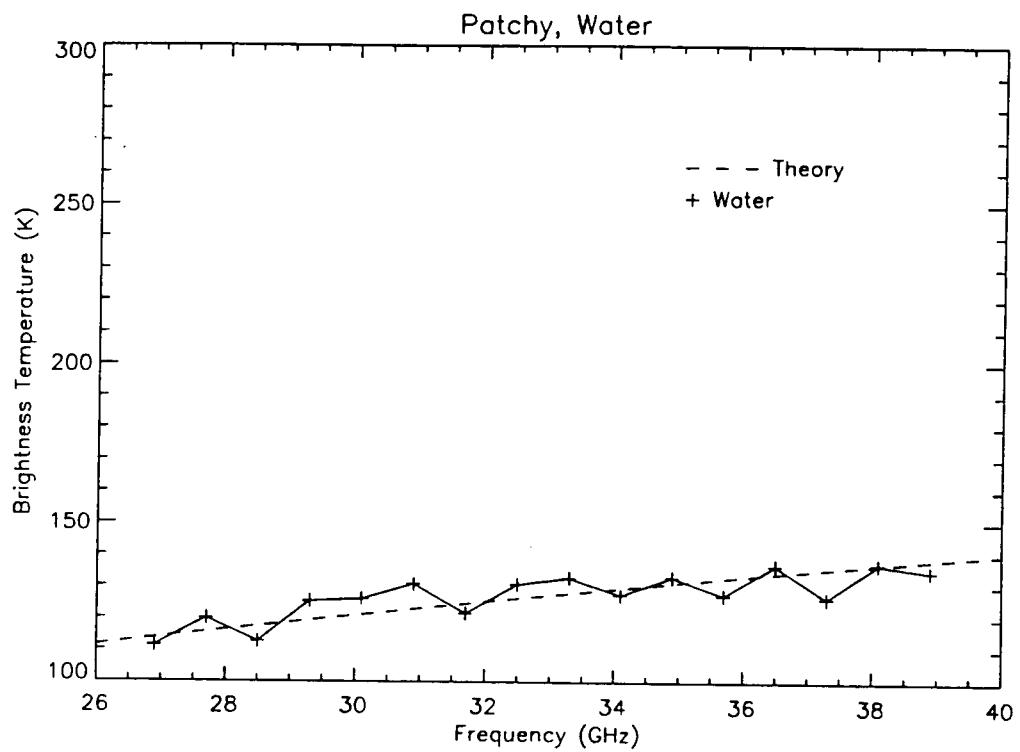
Patchy, Water

Figure C-26. Patchy Oil, Water
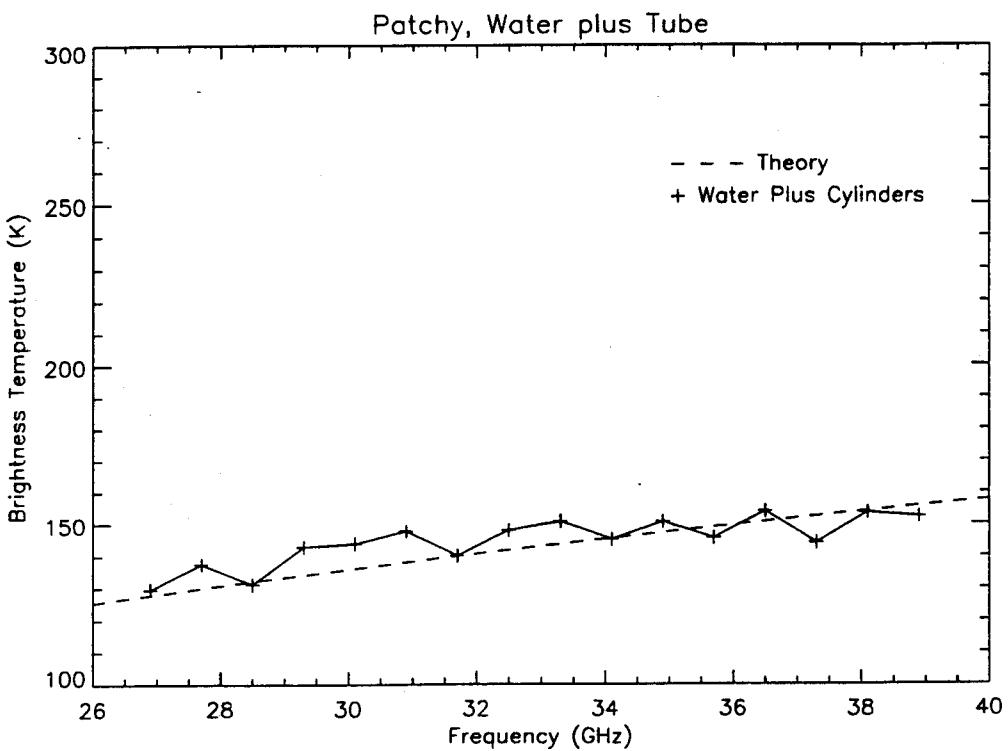
Figure C-27. Patchy Oil, Water and Background
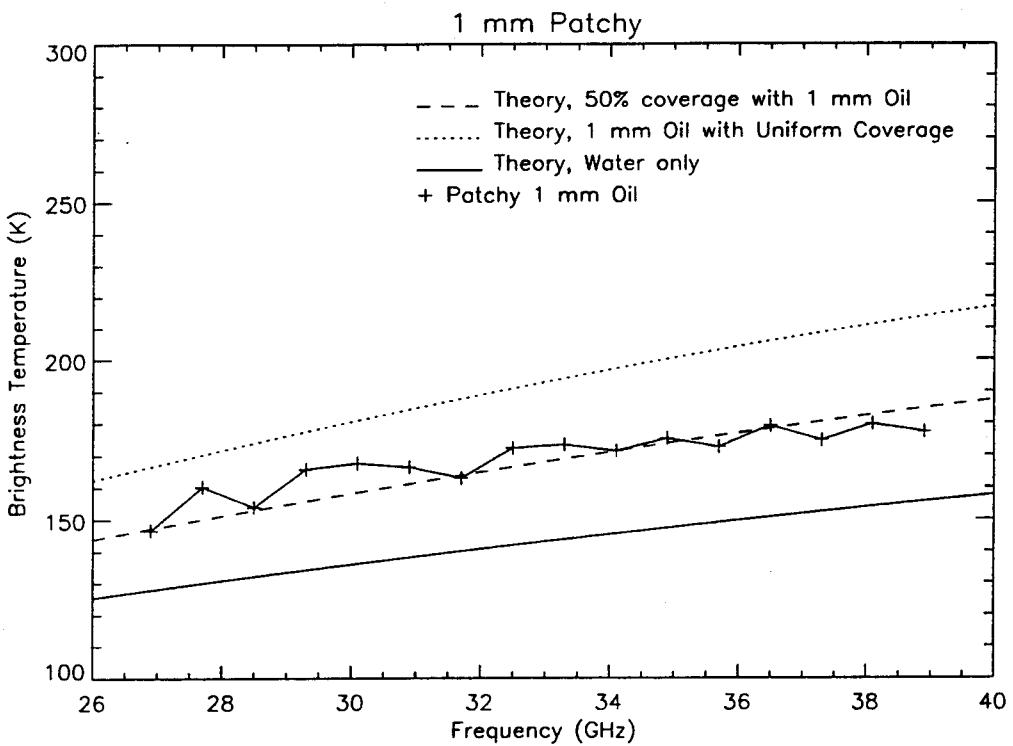
Figure C-28. Patchy Oil, 1 mm Thickness

2 mm Patchy
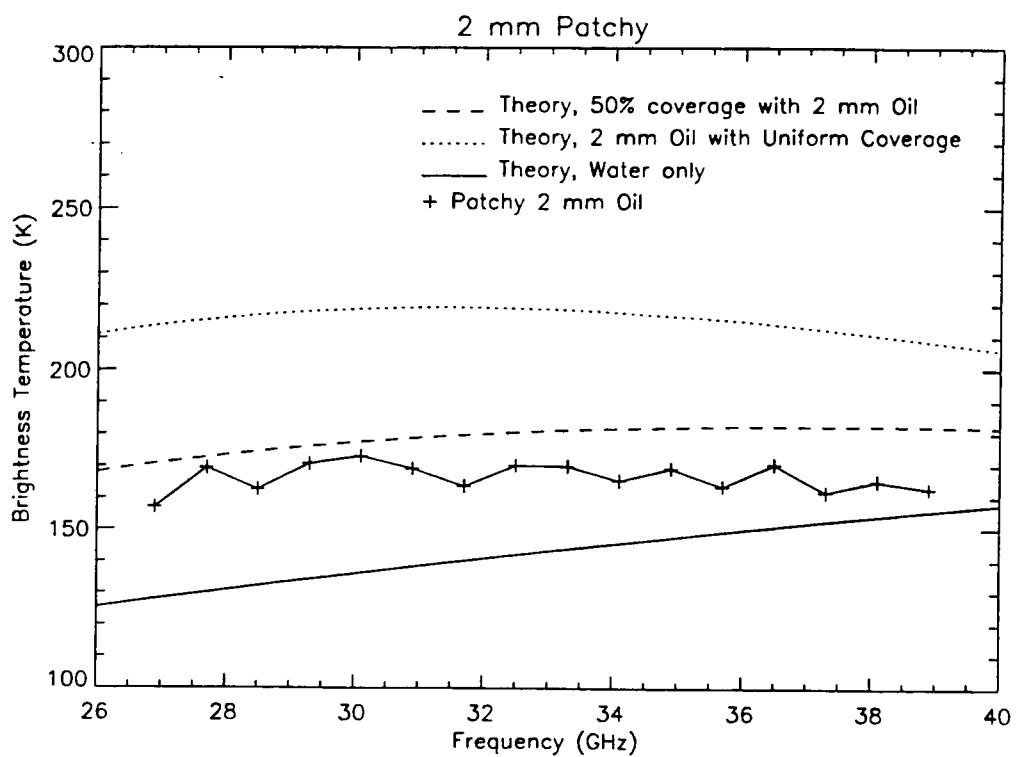
Figure C-29. Patchy Oil, 2 mm Thickness

3 mm Patchy
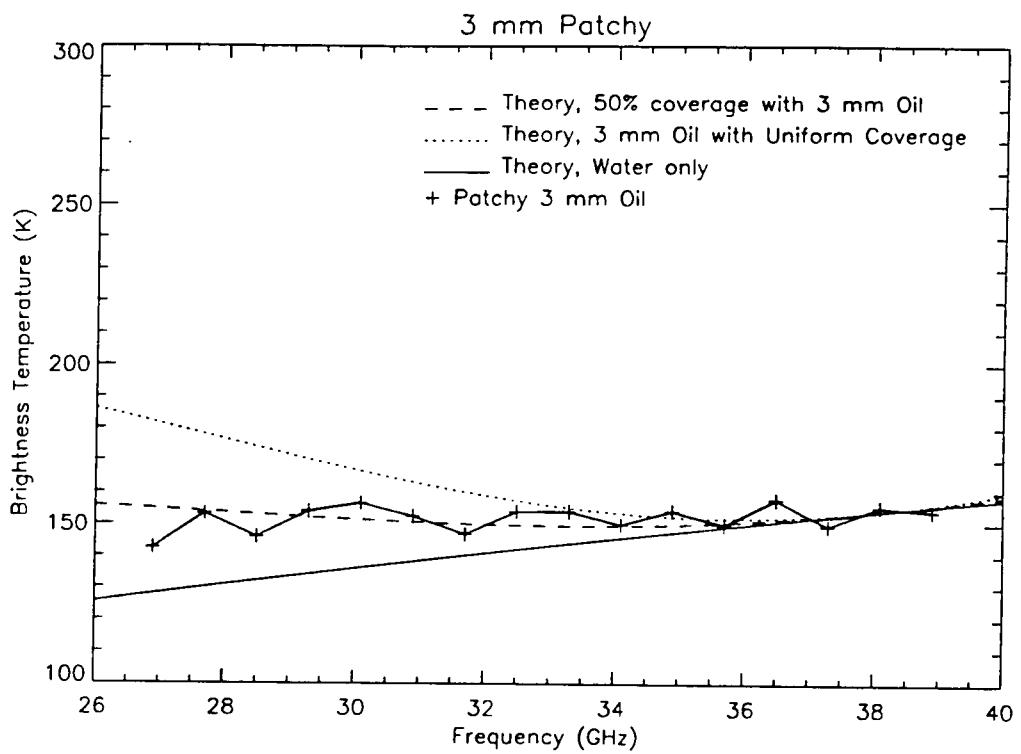
Figure C-30. Patchy Oil, 3 mm Thickness

4 mm Patchy
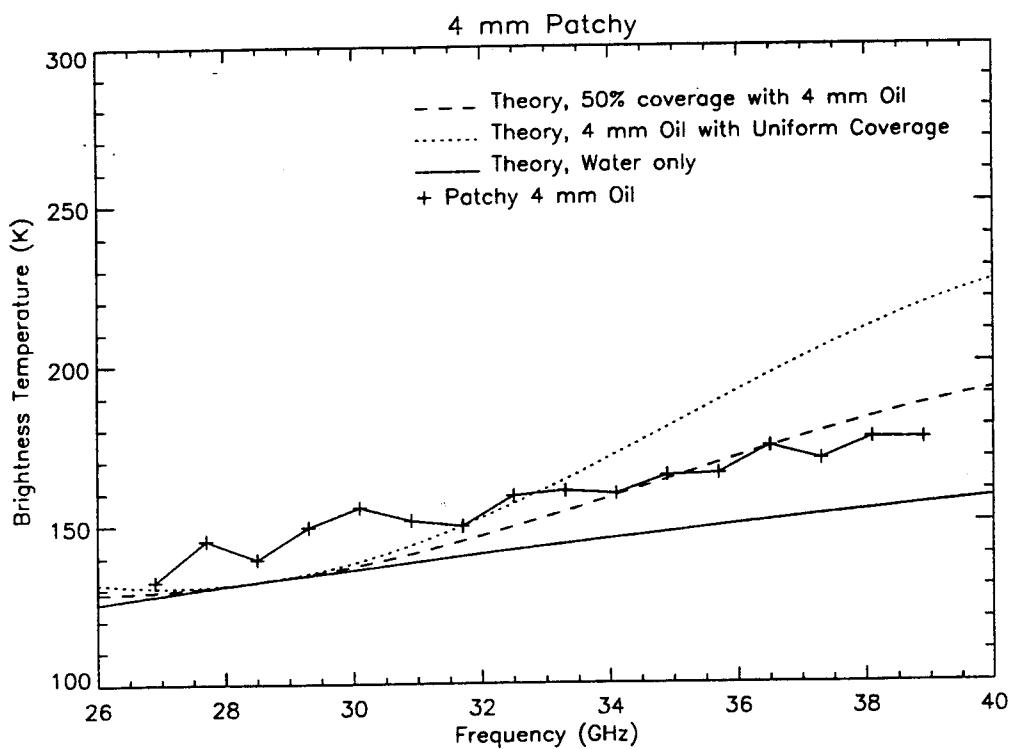
Figure C-31. Patchy Oil, 4 mm Thickness

5 mm Patchy
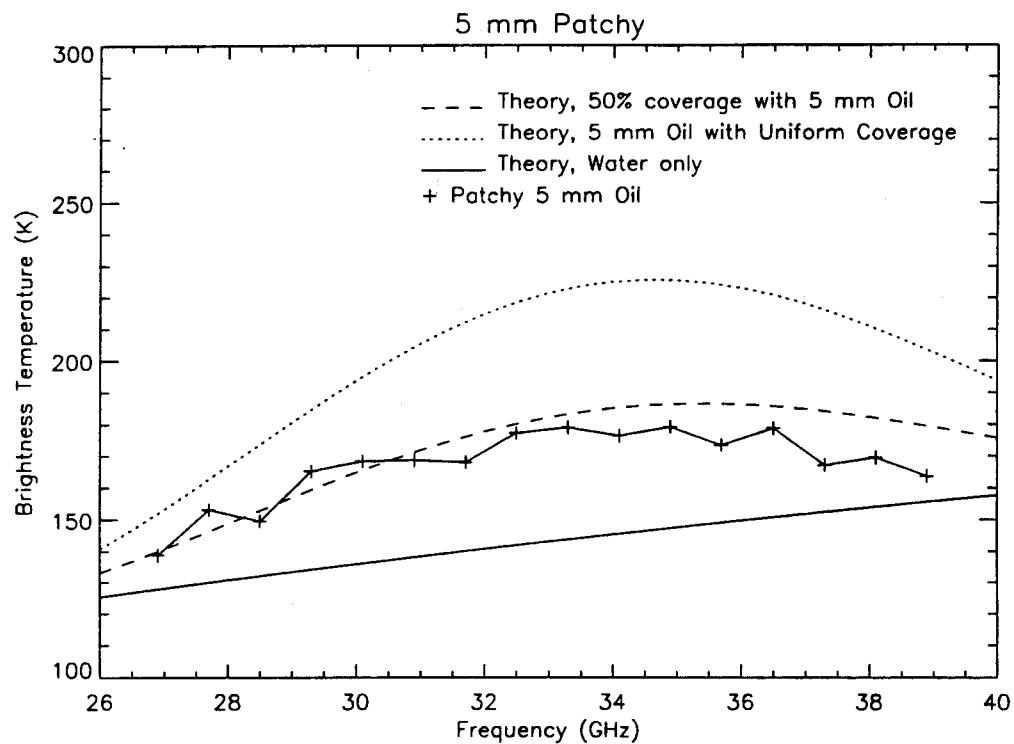
Figure C-32. Patchy Oil, 5 mm Thickness

6 mm Patchy
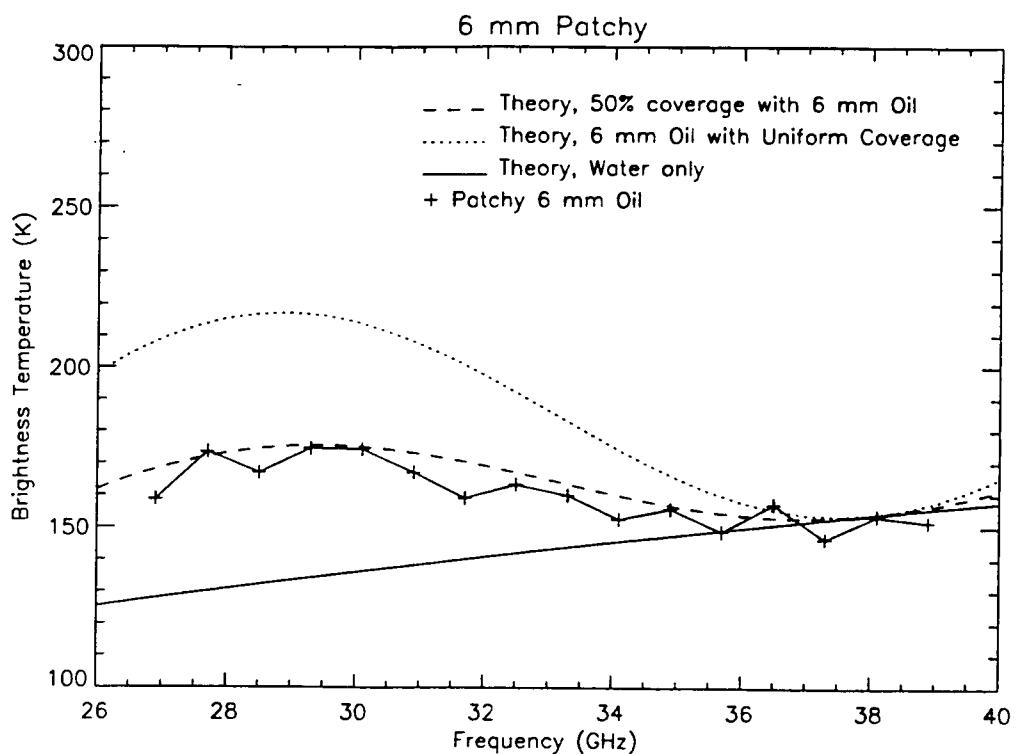
Figure C-33. Patchy Oil, 6 mm Thickness

7 mm Patchy
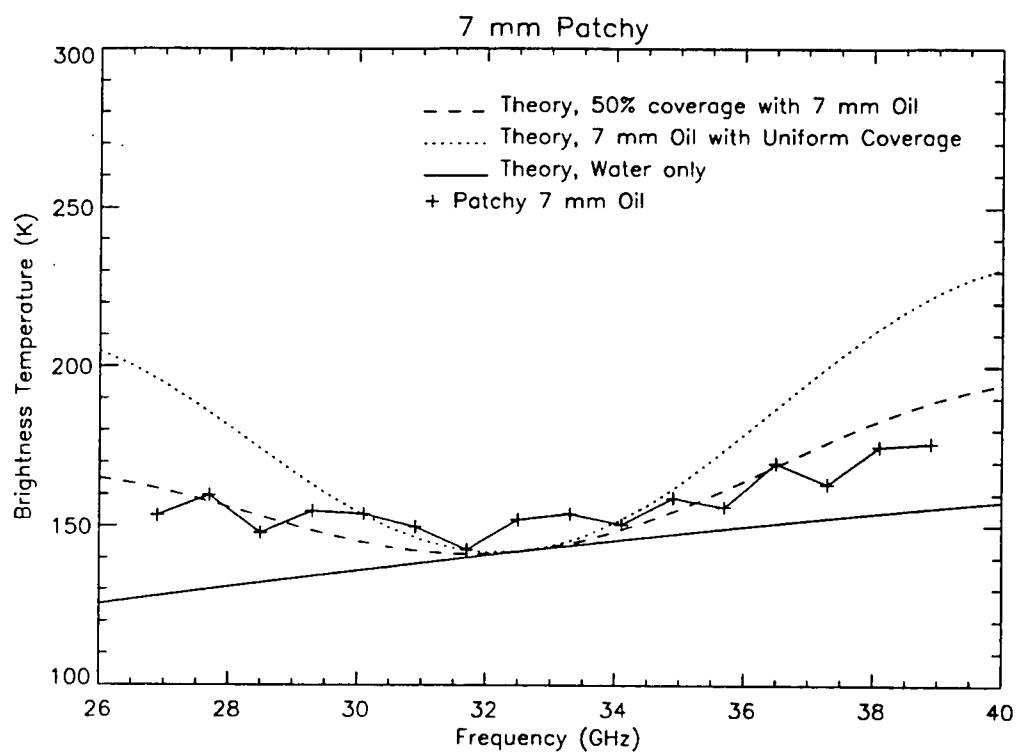
Figure C-34. Patchy Oil, 7 mm Thickness